Optical tweezers combined with fluorescence microscopy and a heating laser for the study of model lipid bilayer systems and membrane proteins

Dissertation
der Mathematisch-Naturwissenschaftlichen Fakultät
der Eberhard Karls Universität Tübingen
zur Erlangung des Grades eines
Doktors der Naturwissenschaften (Dr. rer. nat.)

vorgelegt von Gero Hermsdorf
geb. in Burgstädt

Tübingen 2019

Gedruckt mit Genehmigung der Mathematisch-Naturwissenschaftlichen Fakultät der Eberhard Karls Universität Tübingen.

Tag der mündlichen Prüfung	18.12.2019
Dekan	Prof. Dr. Wolfgang Rosenstiel
1. Berichterstatter:	Prof. Dr. Erik Schäffer
2. Berichterstatter:	Prof. Dr. Ana García-Sáez

Für Lena und Julius.

Abstract

In the past decades, optical tweezers have been an exquisite tool to study a variety of molecular machines. By studying mechanical properties of these biomolecules, it has been possible gain new insights into a range of biophysical questions regarding, for example, microtubule dynamics, the stepping behaviour of motor proteins, DNA mechanics, as well as, membrane remodelling. Membrane remodelling is important for many essential cellular processes such as cell division, vesicular transport of cargo, formation of filopodia and fission and fusion of the mitochondrial network. A cell's plasma membrane encloses the cytosol and defines its boundary to the extracellular environment. Any interaction between the cell and the environment is mediated either by membrane transport proteins or a change of membrane shape resulting, for instance, in an exchange of cargo via endo- or exocytosis. Deformations in the shape of the whole cell are predominately mediated by the cytoskeleton, whereas deformations during endo- and exocytosis are mediated by a shape change of the plasma membrane and its associated proteins. To regulate these mechanisms of membrane transport and deformation, cells developed several fundamental processes. One such essential process is the intracellular transport of membrane proteins or soluble components via vesicles. These vesicles form out of a flat membrane and initially remain in contact with the original membrane through a tether. This reshaping of a membrane has been studied with a variety of *in vitro* membrane systems such as giant unilamellar vesicles utilizing optical tweezers. How an individual protein or oligomer induces this membrane deformation remains poorly understood.

To study the mechanics of membrane remodeling, I established an *in vitro* assay of a reconstituted hemispherical giant unilamellar vesicle. In the experiment, a membrane tether is pulled out of a vesicle and interactions with membrane associated proteins can be observed. Here, dynamin related protein 1 (DRP1) was shown to sever membrane tethers after diffusion on the model membrane system. To perform these experiments, I developed an optical tweezers system that is capable of simultaneous force and fluorescence measurements. The system is further equipped with simultaneous interference reflection microscopy and a heating laser that can locally increase the temperature, for example, to adjust the membrane tension of vesicles. Furthermore, a novel vibration isolation system and advanced temperature control minimized mechanical noise and thermal drift, respectively. The novel, custom-built microscope with single-molecule sensitivity allows to correlate membrane deformation with the presence of individual proteins or oligomers. In the

long-term, such experiments will provide a better understanding of how proteins deform membranes to fulfil their cellular functions.

Zusammenfassung

In den letzten Jahrzehnten haben sich optische Pinzetten als ein hervorragendes Werkzeug zur Untersuchung einer Vielzahl molekularer Maschinen etabliert. Durch die Untersuchung der mechanischen Eigenschaften dieser Biomoleküle konnten neue Einblicke in eine Reihe von biophysikalischen Fragen ermöglicht werden, z. B. in Bezug auf die Mikrotubulusdynamik, das Schrittverhalten von Motorproteinen, die DNA-Mechanik sowie die Membranremodellierung. Die Remodellierung der Membran ist wichtig für viele wesentliche zelluläre Prozesse wie die Zellteilung, den Transport von Vesikeln, die Bildung von Filopodien oder das Abspalten und Fusionieren des mitochondrialen Netzwerks. Die Plasmamembran einer Zelle umschließt das Cytosol und definiert dessen Grenze zur extrazellulären Umgebung. Wechselwirkungen zwischen Zelle und Umwelt wird entweder durch Membrantransportproteine oder eine Veränderung der Membranform vermittelt z.B. durch Materialaustausch der Endo- oder Exozytose. Deformationen der Form der gesamten Zelle werden überwiegend durch das Zytoskelett vermittelt, wohingegen Deformationen während der Endo- und Exozytose durch eine Formänderungen der Plasmamembran und der damit verbundenen Proteine vermittelt werden. Um diese Mechanismen des Membrantransports und der Deformation zu kontrollieren, entwickelten die Zellen mehrere grundlegende Prozesse. Einer dieser essentiellen Prozesse ist der intrazelluläre Transport von Membranproteinen oder löslichen Komponenten über Vesikel. Diese Vesikel bilden sich aus einer flachen Membran und bleiben anfangs durch einen Membrantubus mit der ursprünglichen Membran in Kontakt. Diese Umformung einer Membran wurde mit einer Vielzahl von *in vitro* Membransystemen wie z.B. riesigen unilamellaren Vesikeln unter Verwendung einer optischen Pinzette untersucht. Wie ein einzelnes Protein oder Oligomer diese Membranverformung hervorruft, ist bisher nur unzureichend bekannt.
Um die Mechanismen der Membranremodelierung zu untersuchen, habe ich ein *in vitro* Experiment für ein rekonstituiertes unilamellares Riesenvesikel in Form einer Halbkugel durchgeführt. In diesem Experiment wird ein Membrantubus aus dem Vesikel herausgezogen und Wechselwirkungen von dem Tubus mit membranassoziierten Proteinen können beobachtet werden. Ich konnte zeigen, dass Dynamin-Related Protein 1 (DRP1) nach Diffusion auf dem Modellmembransystem den Membrantubus trennen kann. Dieser Prozess ist für die Teilung von Mitochondrien und deren Instandthaltung wichtig. Um solche Experimente durchführen zu können, habe ich einen neuen experimentellen Aufbau entwickelt basierend auf einer optischen Pinzette, bei welchem gleichzeitige Kraft- und Fluoreszenzmessungen

durchführbar sind. Das System ist weiterhin mit einem Interferenzreflexionsmikroskop und einem Heizlaser ausgestattet. Alle Methoden können simultan benutzt werden. Der Heizlaser kann die Temperatur lokal erhöhen, um beispielsweise die Membranspannung von Vesikeln einzustellen. Darüber hinaus haben ein neuartiges Vibrationsisolationssystem und eine sehr stabile Temperaturregelung mechanische Schwingungen bzw. thermische Drift des Systems minimiert. Dieses neuartige maßgeschneiderte Mikroskop, welches Einzelmolekülempfindlichkeit hat, ermöglicht gleichzeitig die mechanische Membranverformung und die Lokalisisation einzelner Proteine oder Oligomere zu messen. Langfristig werden solche Experimente ein besseres Verständnis dafür liefern wie Proteine Membranen, deformieren um ihrer Zellfunktionen zu genügen.

Contents

Part I.

Introduction

Some membrane proteins are molecular machines that can convert chemical energy resulting from ATP or GTP hydrolysis into mechanical work. These machines can e.g. deform membranes in a variety of essential cellular processes e.g. cell division, vesicular transport of cargo, formation of filopodia, and fission and fusion of the mitochondrial network. The study of membrane proteins in reconstituted *in vitro* system remains challenging due to the complexity of the membrane with which the proteins interact and the wide range of curvatures they may prefer. Especially high curvatures, for example, of membrane tethers are difficult to generate in a controlled fashion. Using *in vitro* systems allows to manipulate the conditions, compositions, or other biochemical parameters to characterize the properties of membrane proteins. The availability of *in vitro* assays to study mechanical interactions of membranes tethers with membrane proteins on the single-molecule level, as well as the availability of suitable instruments to perform these assays are very limited. A milestone in this direction was developed by Heinrich and Waugh [1] that allowed to generate a single membrane tether that was later combined with fluorescence. To date, optically trapped microspheres have been used to generate to single tethers that were investigated with epi-fluorescence [2–4]. Most of these experiments used a high concentration of proteins and showed the average behavior of an unknown quantity of proteins. The force signal was detected via video tracking that resulted in a low spatiotemporal resolution. The motivation for this project was to push the limits in sensitivity of an optical-tweezers-based assay towards single-molecule fluorescence detection on a single membrane tether. I develop a surface-based assay in which one can generate single membrane tethers in a controlled manner close to a surface. The proximity of the tether to the surface allows in principle to use the evanescent field of a total internal reflection fluorescence microscope for the observation of single membrane proteins. The need for a new instrument that is optimized for membrane-based assays resulted from previous studies [5], in which giant unilamellar vesicles were used as membrane reservoirs.

This thesis consists of six major parts. In Part I, I motivate the need for a new optical tweezers system based on existing methods that allow force measurements on membranes and membrane proteins. Part II focusses on the overall development of my optical tweezers system. Chapter 1 describes how the instrument is isolated from vibrations. I will show a custom-built, passive vibration system and compare it to commercially available systems. Chapter 2 describes the optical design and features of the system. Part III focusses on the novel *in vitro* lipid bilayer assay that was performed with the custom-built system to generate membrane tethers. In Chapter 3, I will show experiments with a standard lipid DOPC that allow to determine membrane and giant unilamellar vesicle properties. Chapter 4 provides new insight into the behavior of the membrane protein DRP1 and its interactions with membrane tubes. Part IV of this thesis is a summarized outlook for future experiments.

Part II.

Development of optical tweezers optimized for membrane studies

1. Stabilized environment for optical tweezers

Using optical tweezers offers the possibility to measure displacements in range of nanometers and below. A stable environment is a key requirement for a precise measurements. Mechanical vibrations from the building and the environment are going to be reduced by the choice of a suitable vibration isolation system. We chose a commercial system to be implemented into our optical tweezers system, that i built. The tedious optimizations on custom built vibration isolation systems would have protracted the development of the optical tweezers. Nevertheless, in the long term high performance vibration isolation system are desired for high precision measurements. Therefore, we choose a parallel development of a custom built optical tweezers and a vibration isolation system that can be used for other high-end microscopes.
In the following chapter, the performance of a commercial vibration isolation system and the design and performance of a custom built vibration isolation system is shown. These results have been published in Review of Scientific Instruments [6] and are quoted in this chapter. To broaden the understanding, additional data is provided compared to the published manuscript.

1.1. Introduction

Advances in modern technology have enabled the investigation and development of nanoscale objects ranging from semiconductor devices to single molecular machines in biology. One requirement to manipulate and observe such objects, is to isolate instruments that are used to characterize these objects from mechanical vibrations that are particularly present in fabrication plants and research laboratories. The amplitude of such vibrations often exceeds the dimension of nanoscale objects in particular for frequencies below 10 Hz. The frequency band of building noise typically ranges from sub-1 Hz to several tens of hertz depending on the source. Typical noise sources that couple to building resonances in the range of about 1–40 Hz are elevators ($\lesssim$40 Hz), people walking in the building ($\approx$1–5 Hz), heating/ventilation/air conditioning ($\approx$7–350 Hz), machines, motors, and transformers ($\gtrsim$4 Hz, often with peaks close to the power line frequency of 50 Hz or 60 Hz and overtones), wind ($\approx$1–13 Hz), ocean waves $\approx$ 0.1 Hz and many more such as nearby traffic [7,

8]. Vibrations with frequencies below $\lesssim$100 Hz have a long wavelength compared to typical room dimensions. Therefore, they are well transmitted through structures. Because of their long wavelength they are also poorly damped by most materials. Mechanical vibrations with frequencies above 100 Hz often have sufficiently low amplitudes that they do not interfere with measurements. In this frequency range, sound isolation is more important, which will not be considered further here.
For isolation of instruments from mechanical vibrations, most passive systems are approximated and oversimplified by a one-dimensional damped-harmonic-oscillator model [7–12]. Below the resonance frequency f_0, vibrations directly couple to the instrument without attenuation. Above resonance, vibrations are attenuated. The relative amplitude of transmitted vibrations rolls off in analogy to a low pass filter. The strength of the filter depends on the damping ratio $\zeta = \gamma/(2\sqrt{m\kappa})$, where γ is the damping coefficient, m the instrument mass, and κ the spring constant. For high frequencies $f \gg f_0$ the amplitude of a damped harmonic oscillator falls off with $1/f^2$ independent of the damping ratio. However, the motion transmissibility of a vibration isolation system, taking into account the displacement of the oscillator position relative to the (moving) support, falls off with $1/f$ [7, 8]. And, counterintuitively, the amount of vibration isolation for $f > \sqrt{2}f_0$ is less with an increased damping ratio. Therefore, systems are typically not overdamped with the consequence that at resonance vibrations are slightly amplified [7, 8]. Real systems have many degrees of freedom, typically coupled through viscoelastic damping elements [8]. The response of such a system to a disturbance often cannot be solved analytically. Thus, the vibration isolation performance needs to be tested under conditions that the system is designed for. The optimal amount of damping will depend on the noise spectrum of the building and other criteria such as an optimized transient response. Overall, for efficient vibration isolation between 1–10 Hz, a passive vibration isolation system ideally should have a fundamental resonance frequency below 1 Hz, be somewhat underdamped ($\zeta < 1$), and provide damping in all degrees of freedom without coupling them.
Typical vibration isolation systems for optical tables include bungee cords [13], air damped tables [14], passive systems with a negative-stiffness mechanism [12], active systems that include an accelerometer, an actuator and feedback controller [11, 15, 16], and less common pendulum systems [17]. While suspension from bungee cords is by far the cheapest solution, damping may not be optimal, cannot be tuned, and is determined by the choice of rubber. Also, because rubber is viscoelastic there is creep in the extension, the stress-strain relation may be highly non-linear, and large static strains exceeding 50 % are not recommended over long periods of time [8]. One reason for the latter recommendation is that rubbers may crystallize under high, continuous strain causing failure of the material [8]. In general, for a ceiling-suspension system, the ceiling height limits the maximum length of the extended suspension spring given by its resting length plus its extension. Low resonance frequencies require high ceilings. Interestingly, the resonance frequency

f_0 of a mass suspended from a ceiling via a Hookean spring only depends on the extension Δz of the spring

$$f_0 = \frac{1}{2\pi}\sqrt{\frac{\kappa}{m}} = \frac{1}{2\pi}\sqrt{\frac{g}{\Delta z}} \approx \frac{0.5\,\mathrm{Hz}}{\sqrt{\Delta \tilde{z}}}, \tag{1.1.1}$$

with the gravitational acceleration g and the value of the extension in meters is denoted by $\Delta\tilde{z}$. For example, for a resonance frequency of 0.5 Hz, 1 m of spring extension is necessary. The relation is a consequence of Newton's first law, that, in steady state, the table is at rest with no net force acting on it: the sum of the gravitational force F_g and spring force F_s is zero, i.e. $F_g + F_s = mg - \kappa\Delta z = 0$, resulting in Eq. 1.1.1 due to the linear relation between the spring constant and the mass ($\kappa = mg/\Delta z$). Thus, for a given geometry, i.e. ceiling height, the resonance frequency is only limited by how far the suspension spring can be extended. To achieve the maximum extension for a given mass, the spring constant needs to be chosen appropriately. While rubber generally allows for very high strains up to several times the resting length, for continuous strain applications—as stated above—maximum strains of ≈50 % are recommended. This strain also roughly corresponds to the maximum strain before failure of common bungee cords [18]. Thus, with such a strain and an extension of one meter, the resting length of the bungee cord would be about two meters. Together with an optical table height of about one meter, results in a ceiling height of about four meters. Steel springs allow for a shorter resting length, are ideal for large static, continuous deflections, and practically have no creep when operated at room temperature [8]. However, steel springs require an additional damping system. Here implemented a vibration isolation system that is viscously damped in all degrees of freedom minimizing the coupling between them. The system is based on steel springs and suitable for common ceiling heights below 3 m. Higher ceilings should allow for a lower resonance and even better performance.

1.2. Materials & methods

1.2.1. Custom room specifications

In the long term the experimental setup to be isolated is a custom-built optical tweezers combined with a TIRFM, IRM, heating laser in detail described in the following Chapter 2. Typical stability requirements for optical tweezers are higher compared to those for optical microscopy, for example in terms of temperature stability and mechanical stability. Therefore, the optical tweezers system has been placed in the basement laboratory of the building in a separate walk-in chamber. This location already reduces the input of vibrations significantly compared to an upper floor. The walk-in chamber itself is isolated from the remaining building via

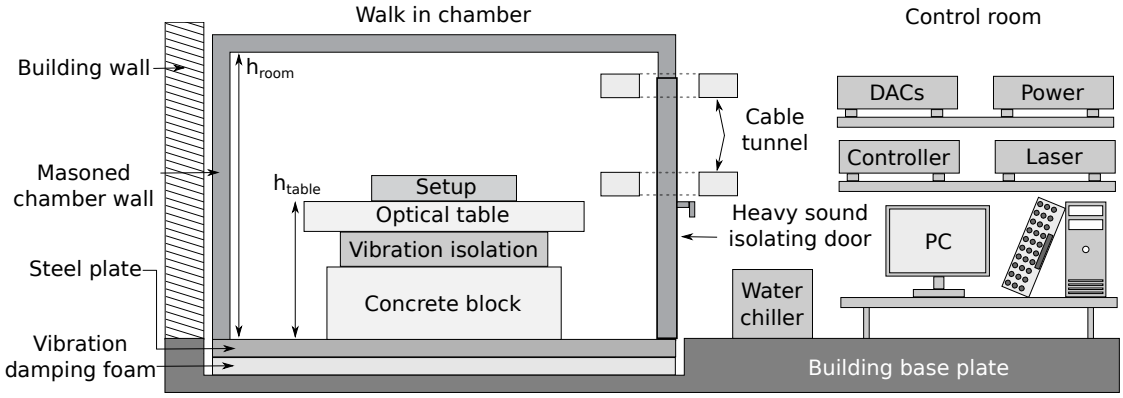

Fig. 1.1 | Walk in chambers and control room for experimental setup. The optical tweezers setup has been constructed in the basement of the building. To decouple the users from the instrument, the setup is located in a separate walk-in chamber that isolates from mechanical and acoustic frequencies and temperature variations. For the isolation of mechanical vibrations an additional system (Minus K 500BM-1) has been used.

a vibration damping foam underneath a steel plate floor. On the steel plate, the chamber is made of brick walls with a concrete ceiling ($h_{room} = 2.5\,\mathrm{m}$) and soundproof door (Fig. 1.1). The chamber isolates well from acoustic noise. Experiments are controlled from outside the chamber minimizing user-induced disturbances. The used vibration system is placed on a custom concrete block. On top is a high precision optical table ($1000\times1200\times200\,\mathrm{mm}$, 1HT10-12-20, Standa, Lithunia) for the optical tweezers setup to be mounted on ($h_{table} = 1\,\mathrm{m}$). The setup is surrounded with an optical enclosure (TB4&XE25 25 mm Rails, Thorlabs, US). This enclosure partially protects the setup from stray-light, dust, acoustic noise, air convection, and temperature changes. The control room is equipped with an overpressure air conditioning system. This keeps the temperatures fairly stable all over the year. With the overpressure in the room, we try to keep dust out of the room. The necessary water cooling for one of the cameras is positioned furthest away from the walk-in chamber within the limits of the control room. As a general principle, I tried to avoid any fans and power supplys to be present in the walk-in chamber.

1.2.2. Vibration measurements

In this chapter I will briefly introduce the vibration measurements. To measure acceleration and velocity, we used a 3-axis vibration analyzer system with a specified sensitivity in acceleration of $1\,\mu g$ over a frequency range of 2–1000 Hz (VA-2; The TableStable Ltd., Mettmenstetten, Switzerland). Note that our resonance frequency of 0.5 Hz for the Minus K BM500-1 and for the custom built vibration

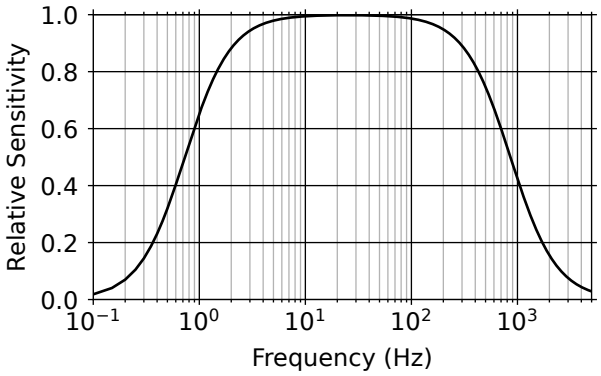

Fig. 1.2 | Transfer function of the vibration analyser VA-2. The transfer function shows a sensitivity drop between 0.1 Hz and 10 Hz and between 100 Hz and 5000 Hz. This drop in amplitude sensitivity does not effect the sensitivity of frequency measurement.

isolation was outside the range of the vibration analyzer's transfer function. We approximated the transfer function T by

$$T = 1/(1 + (0.73/f)^2)/(1 + (f/858)^2) \tag{1.2.1}$$

in the frequency range of 0.1–5000 Hz from the provided manual's printed graphical plot, converted by a plot digitizer [19]. At a value of $T \approx 0.3$ at 0.5 Hz vibrations on the table were largely below 1 μg (Fig. 1.3). Also note that while vibration amplitudes may be underestimated outside the specified frequency range, the frequency itself of a certain vibration, e.g. a resonance, is still reliably measured. The sensor readout for the respective axis has been recorded with a USB data acquisition card (NI 6221 USB, National Instruments). The time signal can be directly saved for displacement measurements or further processed by a fast Fourier transformation (FFT) in a custom LabView VI to a power spectral density (PSD). From the spectral densities of the acceleration amplitude A, the velocity V and displacement X can be calculated by

$$|V| = \frac{1}{\omega}|A| \tag{1.2.2}$$

and

$$|X| = \frac{1}{\omega^2}|A|, \tag{1.2.3}$$

where $\omega = 2\pi f$ is the angular frequency. The common approach to compare vibration isolation systems is to record a so called transmissiblity of a system. A typical procedure would be to use an electrodynamic shaker mounted on a heavily reinforced frame that supports also the to-be-tested vibration isolation system. A

first vibration sensor is mounted on the frame where the electrodynamic shaker is placed and a second sensor is placed on top of the isolator. A dynamic input of a certain frequency is applied and a PSD for both sensors has to be measured. The ratio of the passed vibrations divided by the input vibrations is what I will refer to as dynamic measured transmissibility. This methodology most likely arises from the developments made in building enforcements due to earth quakes [20, 21], which resembles the measurement situation. Due to the lack of suitable equipment I could not perform experiments in this manner. Excited amplitudes are much larger compared to amplitudes for a static measured transmissiblity, which will be used in the following chapters to compare different systems. By static measured transmissiblity, I mean an equilibrated measurement. We define the floor vibrations as the input signal and a second measurement at a different time point on top of the vibration isolation system as the isolated signal. A static measured transmissiblity reflects the actual situation in a research lab with quiet and sparse input vibrations more adequately. Since these mechanical input vibrations are low in amplitude and originate from the building and its interior itself, they represent a typical mechanical noise input.

1.3. Results

1.3.1. Performance of a commercial passive vibration isolation systems

We choose a passive vibration isolation system Minus K 500BM-1 (Minus K Technology, Inglewood, USA) to be paired with the custom optical tweezers system. The system operates via a negative stiffness mechanism that is describes elsewhere [12]. To achieve the desired 0.5 Hz natural frequency a certain mass is needed. I had to add a mass within the range of 164–239 kg. The used optical table contributes with ≈139 kg already a significant portion. Since the weight distribution of optics, cameras and lasers will be inhomogeneous, I later added lead bricks to level the system. Due to the compact measures (610 mm width x 572 mm depth x 216 mm height) the MinusK system needed to be elevated. In previously developed optical tweezers setups a heavy custom-made steel-profile frame was used [22–24]. From these experiences, we decided to design a table stand made out of concrete by ourselves. The wooden box to give the concrete block the desired shape was made by the university wood workshop. The concrete was kindly provided by the construction site of the greenhouse next to the institute. After drying, the concrete block was painted to avoid any concrete dust emerging from the block once its inside the walk-in chambers, where sensitive optics would be exposed to it. In Fig. 1.3 the concrete block is shown in the inset. The two cut outs on the bottom are made for moving the block with a forklift. We choose concrete with the inten-

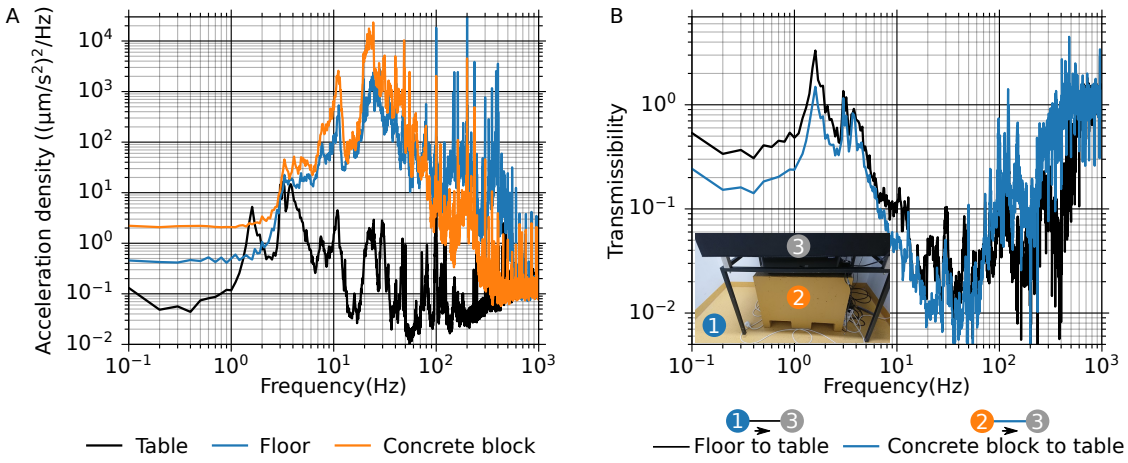

Fig. 1.3 | Passive vibration damping. A, Power spectral density in the z-axis of the floor, on top of the concrete block, and with the damping system active. B, Statically measured transmissiblity for position 2 and 3 marked in the inset picture. Inset: Side view of the setup. Marked are the measurement positions 1 - floor, 2 - concrete block and 3 - on top of the table. The additional table stand is visible, which limits extreme displacements of the system with manual stoppers attached.

tion to shift any internal resonance to high frequencies. These will essentially not contribute to the overall displacement of the system. For safety reasons, I put an additional table frame under the optical table. This frame prevents any extreme displacements downwards while working on the setup. For the measurement of the acceleration density in Fig. 1.3A, the system has been beforehand adjusted for the payload using the tunable adjustment screw in front of the device. In general, measurements were taken outside of the core working times of the building. The reason was to avoid single large displacement events that could distort the transmissibility due to the mentioned measurement procedure. The PSDs were averaged 40 times with a resolution of 0.1 Hz resulting in a measurement time per single PSD of 10 s. We attribute broad peaks around 10 Hz and 20 Hz to the resonance frequency of the walk-in chambers, since we can observe them in different floor measurements. Both peaks were transmitted and slightly amplified towards the concrete block below $\approx$ 100 Hz. Between 100 Hz and 400 Hz, we already see a reduction of transmitted amplitude. Above 500 Hz all curves lay on top of each other, meaning that amplitudes in this frequency band were below the detectors sensitivity. On the lower frequency band where sensitivity drops as well we can observe three different levels for the measurements. Since they do not overlap as in the higher frequencies, this can correspond to a broad band low frequency that we can not resolve with this device. The measurements were performed at different time points, while a constructions site of the neighbouring building was ongoing.

Depending on the equipment used on the site, different low frequency levels might have been generated. An overall reduction of vibrations reaching the optical table in the frequency band between 5-200 Hz is visible. At ≈1.6 Hz, an additional internal frequency of the vibration table occurs. This peak is also clearly visible in the transmissiblity in Fig. 1.3B. A sharp peak at 100 Hz has been coupled into the system by the air-conditioning outside the walk-in chamber. It could be significantly reduced when the air-conditioning was turned off. We could not observe the typical amplification at the resonance frequency, which is visible in the dynamically measured transmissiblity provided by the company.

1.3.2. Custom-built vibration isolation

The optimization of the custom-built system took longer then expected. Therefore we decided to use a commercial system for the optical tweezers setup as previously described. The custom vibration isolation system is now used with a similar optical table in an almost identical walk-in chamber for a reflected light sheet microscope [5A].
In this chapter, we show how to implement a vibration isolation system that is viscously-damped in all degrees of freedom minimizing the coupling between them. The system is based on steel springs and suitable for common ceiling heights below three meters. Higher ceilings should allow for a lower resonance and even better performance.

1.3.2.1. Design of a steel spring based vibration isolation system

We used steel springs (Z209JX made of EN10270-1 steel; Gutekunst Federn, Metzingen, Germany) with a spring constant of $k = 0.39\,\mathrm{N/mm}$ (initial tension of 21 N and maximum spring force of $438 \pm 22\,\mathrm{N}$) having an unloaded resting length of $z_0 = 0.365 \pm 0.004\,\mathrm{m}$ (including the mounting hooks), a maximum extension of 1.054 m, and weight of ≈1.4 kg. The silicone oil had a very high viscosity of $\eta = 100\,\mathrm{Pas}$ (Wacker AK 100000, Wacker Chemie AG, Munich, Germany). Note that the silicone oil was the most expensive component of the vibration isolation system. The optical table had dimensions of $900\times1400\times200\,\mathrm{mm}$ and a mass of around 146 kg (1HT09-14-20; Standa, Vilnius, Lithuania). As additional test payload, we used about 40 lead bricks weighing 1 kg each. The steel spheres (51604M6; balltech Kugeltechnik GmbH, Bodenheim, Germany) used as damping elements had a radius of $r = 2\,\mathrm{cm}$, a mass of 245 g, and have a M6 thread used to mount them below the optical table. Transparent silicone oil beakers mounted on a table frame were made of acrylic glass in the local workshop with an inner diameter and height of 10 cm. To compare the acceleration on the optical table to the gravitational acceleration, we plot reference lines with a constant spectral density of acceleration in units of g. For example, the root-mean-square (rms) velocity density corresponding

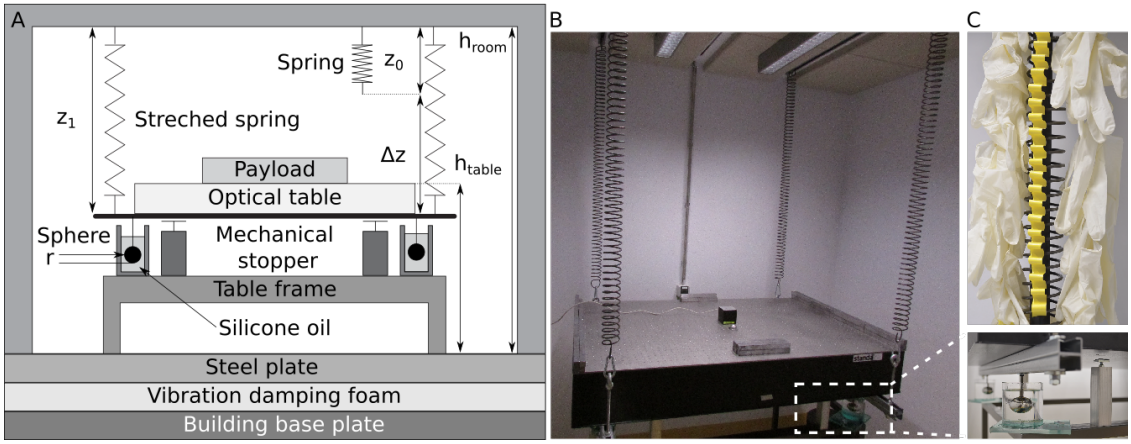

Fig. 1.4 | Steel spring based vibration isolation system.(A) Schematic of the system suspended from the ceiling of a walk-in chamber. (B) Picture of the system showing the vibration analyzer in the middle of the optical table and lead bricks as additional payload. All vibration measurements were performed in this manner. Magnified inset: View of the damping elements, mounting rail, and mechanical stopper. (C) Damping implementation for the internal steel spring resonance based on rubber gloves and tape (yellow) [not shown in (B)]. Dimensions: $z_0 = 0.4\,\mathrm{m}$, $z_1 = 1.4\,\mathrm{m}$, $\Delta z = 1.0\,\mathrm{m}$, $h_{room} = 2.5\,\mathrm{m}$, $h_{table} = 1.1\,\mathrm{m}$, $r = 2\,\mathrm{cm}$. Modified from [6].

to 10 ng is calculated according to

$$V_{10g} = 1/(2\pi f) \cdot 9.81 \cdot 10^{-8}/\sqrt{2}\, m/s^2/\sqrt{\text{Hz}}. \tag{1.3.1}$$

To record the power spectral densities of the vibrations, we used a data acquisition system from National Instruments operated via LabView with custom written software. For noise reduction, we always averaged 40 power spectra. To measure a macroscopic transient response (1–2 cm displacement from the equilibrium position) of the vibration isolation system, we mounted a laser (LuxX 488-100, Omicron-Laserage Laserprodukte GmbH, Rodgau-Dudenhofen, Germany) on the optical table pointing at a camera (PowerShot SX500IS) fixed to the inside wall of the walk-in chamber. The recorded video was analyzed in Fiji [25] by tracking the position of the laser spot as a function of time.

We designed the vibration isolation system for an optical table with a resonance frequency of ≈0.5 Hz in a walk-in chamber with a ceiling height of $h_{\text{room}} \approx 2.5$ m (Fig. 1.4A). The chamber is, as previously mentioned, also located in a basement laboratory room of the building. The walk-in chamber is equipped with mounting rails, in the ceiling. From these ceiling rails, we suspended an optical table using steel springs. The springs were attached to the table via steel mounting rails on which the optical table was fixed (Fig. 1.4B). Note that we used small rubber pads between the end of the springs and the rails to reduce the transmission of high-frequency vibrations. To the same rails, we attached the damping elements—steel spheres immersed in silicone oil. An additional table frame under the optical table was used to fix the silicone oil containers. To prevent extreme downward displacements, we mounted mechanical stoppers to this table frame (see magnified inset in Fig. 1.4B). Based on the estimated weight, the spring constant was chosen to achieve $f_0 \approx 0.5$ Hz. With the total suspended mass of the optical table and test payload, springs were extended to their maximum with a total length of $z_1 = 1.420$ m resulting in $\Delta z = z_1 - z_0 = 1.055$ m. This extension corresponds to a mass of $m \approx 190$ kg and resulted in a table height of $h_{\text{table}} \approx 1.10$ m. An internal resonance of the steel springs, their surge frequency, was effectively damped with soft rubber contacts of standard latex laboratory gloves hanging from the springs and tape connecting the spring coils (Fig. 1.4C). As an equally-well-performing alternative, we used long stripes cut from an inner tube of a bicycle tire mounted on the inside of the springs. With this additional damping, the vibration isolation system is complete for characterization and performance measurements.

1.3.2.2. Optimization and system qualification

To characterize the performance of the vibration isolation system, we measured the power spectral density (PSD) of the vibrations (Fig. 1.5A). We placed the sensor of the vibration analyzer system either in the center of the optical table (Fig. 1.4B) or

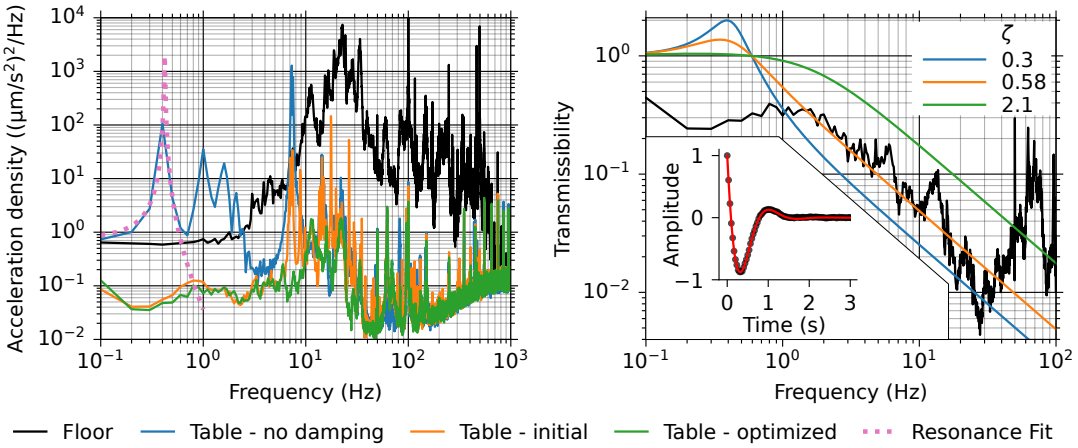

Fig. 1.5 | Vibration spectrum, transmissibility and transient response of the vibration isolation system. (A) Power spectral density of the acceleration measured on the floor and optical table. (B) Transmissibility of the optimized table as a function of frequency. The transmissibility $T = ([1+(2\zeta f/f_0)^2]/[(1-[f/f_0]^2)^2+(2\zeta f/f_0)^2])^{\frac{1}{2}}$ was fitted to the data (red line) in the range of 1–40 Hz using a fixed value of $f_0 = 0.42$ Hz. With the same f_0, T for $\zeta = 0.3$ and 2.1 are shown for comparison. Inset: Normalized amplitude (data: circles, fit: red line) after a ≈1 cm displacement from the equilibrium position as a function of time. As a guide to the eye, the edge of the inset has a $1/f$ slope. Modified from [6].

on the floor directly beneath the optical table and recorded the vibrations from the control room outside the walk-in chamber. The PSD of the floor acceleration inside the walk-in chamber [black line in Fig. 1.5A had a maximum at ≈20 Hz with a first peak at ≈11 Hz presumably corresponding to its lowest fundamental resonance. A narrow peak at 100 Hz was caused by the air-conditioning outside the walk-in chamber, which was significantly reduced when the air-conditioning was turned off. On the optical table, vibrations were significantly reduced at all frequencies (orange line in Fig. 1.5A). With the initial implementation of the system, we observed high peaks at around 7 Hz, 9 Hz, and corresponding overtones. These peaks originated from an internal resonance or surge frequencies between the individual coils of the steel springs due to their finite mass. We successfully damped these resonances by weak rubber contacts between the coils on both the in- and outside of the springs (Fig. 1.4C). These loose contacts optimized the damping in the frequency band around 1–10 Hz (green line in Fig. 1.5A). Note that above 40 Hz, the measurement was largely limited by the sensitivity of the vibration analyzer. Also, some of the peaks may correspond to electronic noise (overtones of the power line frequency). When we removed the damping elements below the optical table, the PSD showed a resonance peak (blue line in Fig. 1.5A) fitted to be at $f_0 = 0.42 \pm 0.01$ Hz (pink dotted line) roughly consistent with the expected value. Thus, the table was well isolated from typical laboratory vibrations with frequencies $f \gtrsim 1$ Hz.

To quantitatively assess the table performance, we estimated its transmissibility and measured its transient step-response behavior. Since we could not measure vibrations on the ceiling or on top of the walk-in chamber, we approximated the motion transmissibility by the ratio of the vibration amplitude on the table relative to the floor (Fig. 1.5B), as previously stated the statically measured transmissiblity. The measurement was limited to a frequency range of ≈2–40 Hz because the vibration analyzer could not reliably measure vibration amplitudes at lower frequencies and, as mentioned above, was not sensitive enough at higher frequencies. In the reliable range, the transmissibility decreased with the expected $1/f$ dependence. A best fit of the theory, resulted in a damping ratio of $\zeta = 0.58 \pm 0.01$. The lowest measured transmissibility was about 0.005 corresponding to -45 dB. Thus, based on the transmissibility, as designed, the vibration isolation system performed as a slightly underdamped ($\zeta \lesssim 1$) harmonic oscillator. After a step-like disturbance, such a system should exponentially relax back to its equilibrium position with some ringing oscillations. This transient behavior, we indeed observed (inset Fig. 1.5B). A fit of an exponentially damped oscillation resulted in a time constant of the exponential relaxation of $\tau = 0.36 \pm 0.01$ s and an oscillation period of $T = 1.39 \pm 0.01$ s. Thus, with a sub-second relaxation time constant, macroscopic disturbances were quickly damped.

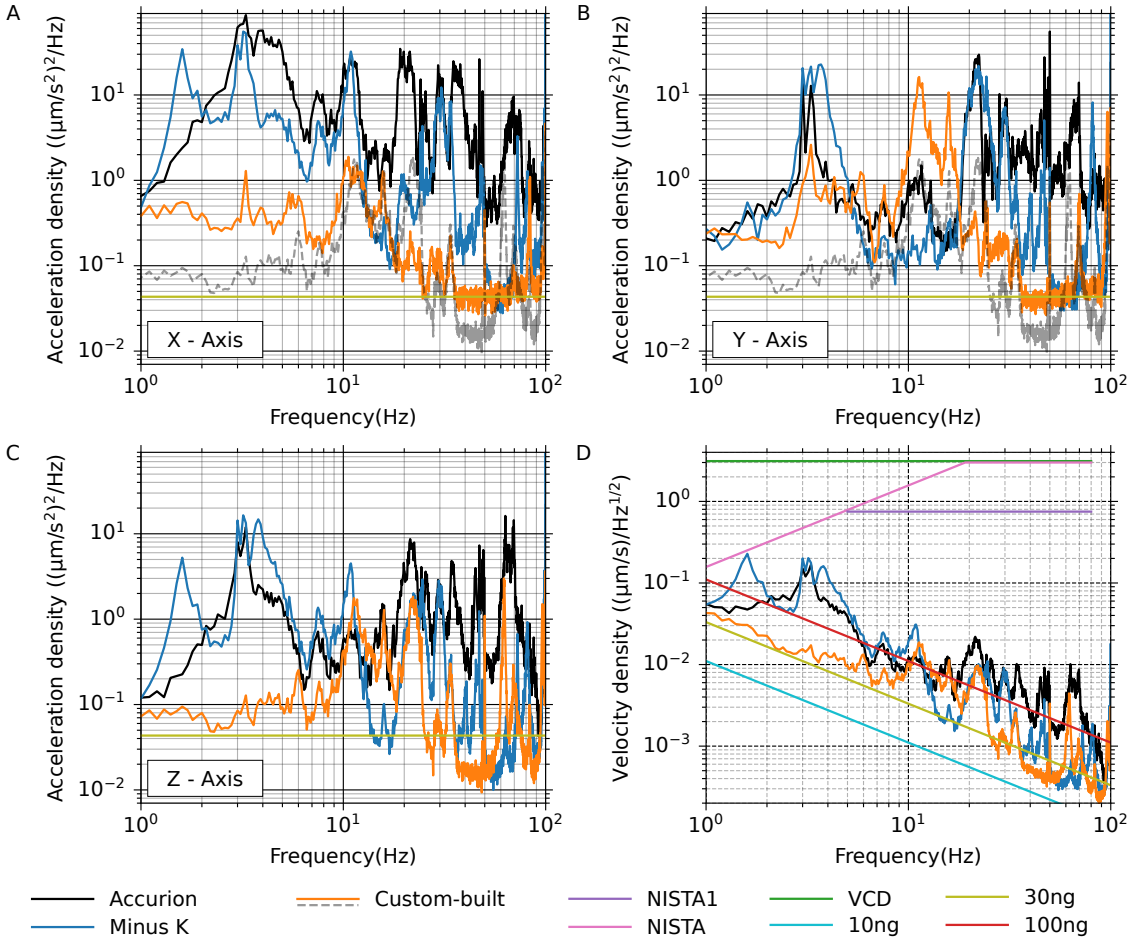

Fig. 1.6 | Performance comparison. (A,B) Horizontal acceleration, (C) vertical acceleration power spectral density for the each direction on top of optical tables isolated using a Minus K 500BM-1, Halcyonics_VarioBasic_90-300 (Accurion, Göttingen, Germany), and our optimized custom-built system. (D) Vibration rms velocity density for the same systems using the same color scheme as in (ABC). Also shown are vibration criteria (VC-E, NIST-A & A1) for facilities with sensitive equipment and reference lines in units of the gravitational acceleration. For comparison, the data for the vertical direction of our system is shown as a dashed grey line within the other X&Y - axes. Modified from [6].

1.3.2.3. Comparison to commercial systems

To evaluate the overall performance of our custom-built system, we characterized its performance relative to two commercial systems and common vibration criteria (Fig. 1.6). Since vibration criteria are expressed in terms of rms velocity (the square root of the vibration velocity PSD; see Materials and Methods [Chapter 1.2.2] for the conversion of the measured acceleration PSD to a velocity PSD), we measured the rms velocity in the vertical z-direction on three similar optical tables with similar weights (including the payload) in the same laboratory room each placed in similar walk-in chambers having comparable floor vibration amplitudes (Fig. 1.6D). Two tables were isolated from vibrations from a state-of-the art active and passive system, respectively, and one by our optimized custom-built system. While our system performed best between 1–10 Hz, above 10 Hz all three systems performed similar. Below 1 Hz, we could not measure any difference between the devices limited by the vibration analyzer. All systems performed better than the stringent NIST-A1 norm and well below the VC-D vibration criterion, which is 2-fold higher than VC-E and the recommended standard for SEM and TEM electron beam devices. The vibration level on the optical table isolated with our custom-built system was comparable to that induced by an acceleration of about 30 ng for most frequencies. Since viscous damping should perform equally well in all directions, we also compared the vibrations in the two horizontal and the vertical direction (Fig. 1.6A–C). For both horizontal degrees of freedom, with few exceptions in narrow frequency bands, our system outperformed the commercial systems significantly in the 1–100 Hz range. The good performance in all spatial directions indicates little coupling between the different translational degrees of freedom.

1.4. Discussion & conclusion

Our custom-built vibration isolation system was designed as a slightly underdamped harmonic oscillator with a resonance frequency of about 0.5 Hz. Since the springs were extended to their maximum extension, the total suspended weight was $m \approx 187$ kg (maximum load plus initial tension divided by gravitational acceleration) , which is consistent with our weight estimate. Using this value, the measured resonance frequency of 0.42 Hz, and Eq. 1.1.1, the spring constant of the individual springs was 0.33 N/mm—somewhat smaller than the specifications. Based on the measured extension and Eq. 1.1.1, the resonance frequency should have been 0.49 Hz. The frequency of 0.42 Hz corresponds to an extension of 1.42 m according to Eq. 1.1.1. Interestingly, this value corresponds exactly to the springs resting length plus its extension, $z_1 = z_0 + \Delta z$, implying that this length was the decisive length. Overall, we attribute the differences from the expected values to nonlinearities of the maximally extended springs deviating from the Hookean ap-

proximation. Apart from this small nonlinear response, we do not expect any other effects, like creep or failure, to occur when operating the springs at their maximum specified extension.

The oscillation period of the transient response was shorter compared to the expected period of the fundamental, "bounce" or "heaving" mode of the optical table. Thus, the table relaxed via a different mode. Since the springs and/or damping elements are not identical, each corner of the table relaxed with a different time constant resulting in a rotation around the center of mass of the table. The resonance frequency of this rotation for a weakly or uncoupled system is approximately $f_{\mathrm{rot}} \approx f_0\sqrt{3(1-4\frac{\Delta L}{L})}$, where L is the length or width of the table and ΔL the distance from the edge of the table to the point of suspension using $\frac{1}{12}mL^2$ for the table's moment of inertia [7, 26]. With the values $L = 1.4\,\mathrm{m}$ and $\Delta L = 0.12\,\mathrm{m}$, the period for the rotational oscillation is $T_{\mathrm{rot}} = 1.4\,\mathrm{s}$, which is in excellent agreement with our measured period. Thus, the table did not relax via its heaving mode, but rather by a rocking, rolling or pitching mode around its center of mass. Since the resonance frequency of this mode is higher compared to the fundamental frequency, the transient response was faster. Furthermore, the quantitative agreement of the measured rotational oscillation period with the theory implies that the coupling between translational and rotational degrees of freedom was small [26].

The transient response provides information about the amount of damping. Based on the measured mass and exponential relaxation time of the transient response $\tau = 2m/\gamma$, the systems's damping coefficient was $\gamma = 1.04\,\mathrm{kNs/m}$. This value is 6.9× larger compared to the Stokes drag of the spheres of $\gamma_0 = 4 \cdot 6\pi\eta r \approx 0.15\,\mathrm{kNs/m}$, where η is the viscosity of the silicone oil and the factor 4 accounts for the four damping elements. The difference can be explained by the nearby walls of the oil container. The drag of a sphere along the axis of an infinite cylinder with a distance to the cylinder wall, in our case, corresponding to 2.5 times the sphere's radius is increased by a factor of ≈3.5 compared to Stokes drag (e.g. [27], p. 318). In addition, the finite length of the cylinder needs to be accounted for, whereby our dimensions invalidate a linear approximation [28]. A lower estimate of the drag increase is given by how the drag increases for movements perpendicular to an infinite flat wall. In our case, this increase is $\approx 1.8\gamma_0$ [29]. Multiplying these two factors results in a total increase of about $6.3\gamma_0$, close to our measured value. Thus, for macroscopic displacements, the damping coefficient is significantly increased by the finite size and geometry of the oil container.

While the measured resonance and mass are consistent with our expectations, there is a discrepancy with respect to the measured damping coefficient and the expected transmissibility. Using the measured values for the damping coefficient, mass and spring constant results in a damping ratio of $\zeta \approx 2.1$. With $\zeta > 1$, the system should be overdamped inconsistent with the damped oscillatory transient response. We attribute the oscillation to the relaxation via the rocking mode and,

possibly, finite-size flow effects of the viscous oil in the cylinders. Also, based on this damping ratio, theoretically the transmissibility should be worse (green line in Fig. 1.5(B)). For comparison, we also plotted the transmissibility for $\zeta = 0.30$ (blue line)—the expected value without the wall effect. The best-fit resulted in $\zeta \approx 0.58$, a value that is closer to the Stokes drag estimate without walls. One possible explanation might be a non-linear, time-dependent viscous response. In the absence of large disturbances, the vibration amplitude on the table was ≈10 nm at 1 Hz falling off with roughly $1/f^2$ (i.e. 0.1 nm at 10 Hz). These amplitudes are much smaller than the dimensions of the spheres and cylinder used for damping. If the spheres move with these amplitudes on these time scales relative to the stationary cylinder, the full equilibrium flow profile in the cylinders may not have been established [30] resulting in an effective damping coefficient closer to the Stokes drag estimate. For small, short, and random amplitude fluctuations, the spheres effectively may not "feel" the presence of the walls. A non-linear damping coefficient that increases with deflection amplitudes could also explain the transient ringing behavior. Alternatively, since the walk-in-chamber is a vibration isolation system in itself, we have a multistage system that doubles high frequency attenuation. For frequencies well above the table and chamber resonances, the transmissibility of the combined system should roll off with $1/f^2$ [7, 15]. However, since the resonance of the chamber is about 11 Hz, this effect should only occur for significantly larger frequencies. At these frequencies, the measured transmissibility showed a broad peak at around 70 Hz. We attribute this peak to resonances of the table frame that supports the oil containers. A more rigid construction of the latter should improve the performance further. However, since at these frequencies the displacement amplitudes of vibrations are already on the sub-Å-level, we did not pursue this idea further.

Overall, our vibration isolation system combined the advantages of steel springs with viscous damping. Steel springs do not drift or creep and allow for a maximum extension in rooms with a common ceiling height allowing for good low-frequency isolation. Since springs are available in all dimensions, our design can be adjusted to different payloads and ceiling heights. For example, a 4-m high ceiling should allow for a resonance of ≈0.3 Hz. We could reduce the high-frequency transmission through the springs and internal resonances by adding soft damping elements to the springs themselves. The rocking motion inherent to the system was beneficial in the sense that it reduced the transient response time. The viscous damping based on four spheres, has the advantage that all translational and rotational degrees of freedom are damped simultaneously. For the horizontal translational modes of freedom, the resonance frequency is given by the well-known pendulum resonance. Since the pendulum length here roughly corresponds to the spring resting length plus its extension, $z_1 = z_0 + \Delta z$, the horizontal resonance is given by $f_0^{\text{horiz}} \approx \frac{1}{2\pi}\sqrt{\frac{g}{z_1}}$, which is even lower compared to the vertical direction (Eq. 1.1.1). Thus, horizontal

vibration isolation is expected to be at least as good as for the vertical direction. This expectation is supported by our data (Fig. 1.6A–C). Since the optical table's rotational degrees of freedom correspond to linear combinations of the translational degrees of freedom of the four individual damping elements, a good performance for the translational degrees of freedom also implies good performance for the rotational degrees of freedom with small coupling between the individual degrees of freedom as pointed out above. Therefore, the viscous elements provide independent damping for each of the three fundamental translational and rotational degrees of freedom of the optical table. The amount of viscous damping can be adjusted by the size of the spheres, the viscosity of the oil, and the distance of the spheres to the bottom of the oil containers. Since the drag coefficient diverges as the spheres approach the bottom [29], the damping coefficient can roughly be varied 10-fold using the latter approach. A lower damping ratio compared to the one we used, may reduce the transient response time, but will increase low frequency noise. The optimal damping depends on the application and vibrational noise spectrum. While commercial system are very compact and are designed to fit under an optical table, our system requires ceiling mounting and space for the springs, which may limit some applications. The better performance of our system compared to the commercial ones may be due to the truly viscous damping, which provides damping in all six degrees of freedom and may minimize the coupling between these degrees in contrast to common viscoelastic dampers. Also, our higher damping ratio may more efficiently reduce the ringing amplitudes of transients arising from the random, superimposed step-like disturbances coming from the building. Overall, the performance of our system meets stringent vibration criteria—it is better than VC-K—with a vibration level of about 30 ng in the vertical direction. The system is comparable to, and in the low frequency range better than, designed low-vibration laboratories [14, 31]. Our solution is cheap, simple to build, and possible to be scaled for different payloads. Thus, in the long term, we expect that our custom-built, high performance vibration isolation system can be used for many other delicate measurement devices such as super-resolution or electron microscopes and will enable sensitive experiments by effectively isolating the instruments from vibrations.

2. Custom-built force and fluorescence microscope for single molecule measurements

2.1. Introduction

Innovation in instrument building can rise by combining existing methods into one new device. Such combinations can open the field for new experiments that are not possible with each method separately performed. Here is a detailed description of the optical tweezers and how I combined it with fluorescence microscopy (TIRFM and tilted illumination), interference reflection microscopy (IRM), a heating laser (HL), and a temperature control (TC). The instrument is designed to perform simultaneous force- and fluorescence measurements close to the lower sample chamber's surface on membranes. From previous experiments [5], we learned that a single objective tweezers instead of a two objective tweezers is favourable for the planned and performed experiments. The upper space above the sample can be used for a simple microfluidic system that is necessary to perform experiments on giant unilamellar vesicles (GUVs). The necessary micro fluidic system requires a certain tube diameter, which increases the overall sample thickness to a degree where it would not fit in-between two high NA objectives as construed previously [22]. Also, micro aspiration pipette experiments are feasible [4, 32–34]. As an alternative to the commonly used forward scattering microsphere detection in optical tweezers, I implemented and optimized a back scattered detection (BSD) mode for this system. Finally, I will present the performance of the system, its mechanical and temperature stability as well as a calibration of optically trapped microspheres.

2.2. Materials & methods

2.2.1. Principle of optical trapping

Optical trapping is based on focused laser light that has been first used by Arthur Ashkin et al.[35] in 1986. He was rewarded with the Nobel prize in Physics in the year 2018. With an optical trap, micro-/nanometer sized objects can be trapped in the center of the laser focus. Displacements form the equilibrium position and

forces can be measured. Application for optical tweezers range from trapped atoms [36], trapped microspheres with attached motor proteins [37],trapping of single-cell green alga [38], to pulled membrane tethers [39] or other micro mechanical experiments.
In case of large object diameters $D \gg \lambda$ with D being the radius of the particle and λ the wavelength of the trapping laser, we can use the laws of geometric optics to explain the trapping effect[40, 41]. Due to its simplicity, a sketch of the ray refraction is provided in Fig. 2.1. The trapping effect is caused by the refractive index mismatch between the medium and the particle. This mismatch causes a refraction of the incident laser twice according to Snell's law. The momentum of the light changes by a certain amount Δ. According to Newton's third law, a momentum of equal magnitude but opposite direction is transferred to the microsphere, resulting in a force, namely the gradient force that acts on the microsphere. This gradient force is pulling a displaced microsphere back to the center of the focus. At the surface of the microsphere is a certain amount of light reflected, which depends on the material properties of the microsphere. This so called scattering force also transfers a certain amount of momentum to the microsphere opposing the gradient force. If the gradient force is larger than the scattering force, a particle can be stability trapped. Due to the scattering force, trapped microspheres have an offset above the laser focus. In case of object diameters $D \approx \lambda$, the Mie theory applies [42, 43], which has to be examined with numerical methods [44, 45].

All theories generate a gradient force. Within the center of the laser focus is a region, where the force F is directly proportional to the displacement Δx of the microsphere. The optical trap can be described as a 3D Hookean spring. The force necessary for a displacement can be formulated by the following equation

$$F = \kappa \cdot \Delta x, \tag{2.2.1}$$

where κ is the so called trap stiffness in, e.g. the lateral x direction. A displacement of a microsphere can be measured by the projection of the refracted or scattered light onto a quadrant photo diode detector[46] or a position sensitive detector [47]. The different approaches for microsphere detection and calibration will be discussed in the following chapters.

2.2.2. Backscattered mode of microsphere detection in optical tweezers

Ten years after optical tweezers have been introduced in 1986, microspheres have been detected by their backscattered light in 1996 [48]. Mostly optical tweezers detection is based on forward scattered light in the direction of the incident laser combined with back-focal plane interferometry[46, 49, 50]. In the forward mode of detection, scattered light from the trapped particle interferes with the unscattered light. The interference is measured in the back focal plane of the condenser

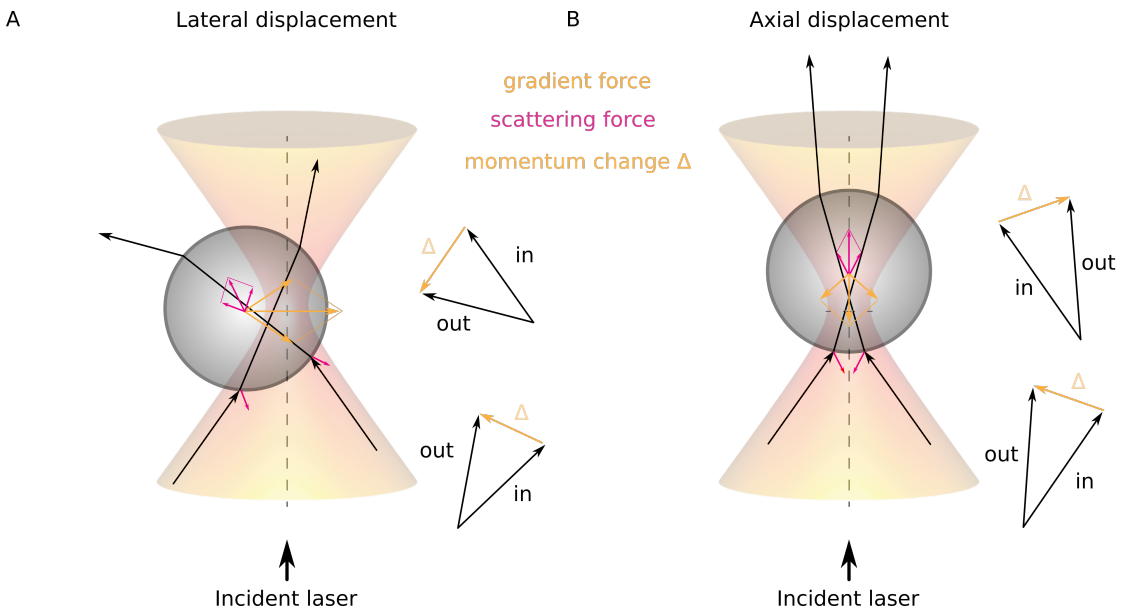

Fig. 2.1 | Optical trapping by geometric rays illustrates scattering and gradient force. The incoming focused laser light leads to a momentum change Δ of the microsphere. Here we collect the scattered light for detection. The schematic was adapted from Reference [22].

objective. The displaced microsphere changes the interference pattern that can be recorded with a detector. This configuration requires a second objective above the incident objection to collect the light scattered by a displaced microsphere. This second objective, with its mostly short working distance and a high NA, limits the thickness of the sample to the range of millimetres or below. In the backscattered mode of microsphere detection, a second objective is not necessary. One objective is used for trapping and detection. This method is thereby compatible with the geometry of objective based TIRFM[51, 52], IRM[53] or iSCAT microscope [54], where excitation and collection of (fluorescent) light is achieved with the same objective. Using only one objective in the inverted microscopy arrangements, clears the upper space of a sample for other methods to be combined with the optical traps such as demonstrated in measurements on e.g. DNA nano pores [55], rotational dynamic of nano fibres in PDMS chambers [56] or micro fluidic system [47] as I will use to perform measurement on GUVs. It has been shown that backscattered detection can provide atomic-scale localization precision, stability, and registration in 3D without compromise [57], when a silicon disk was used. The collection of the backscattered light has been achieved by different optical designs, some of the principles are simplified and reduced to the core features in Fig. 2.2A–F. In Friese et al. [48], simplified in Fig. 2.2A, a simple beam-splitter (presumably 50:50) configuration is used to isolate the backscattered light from a microsphere. The

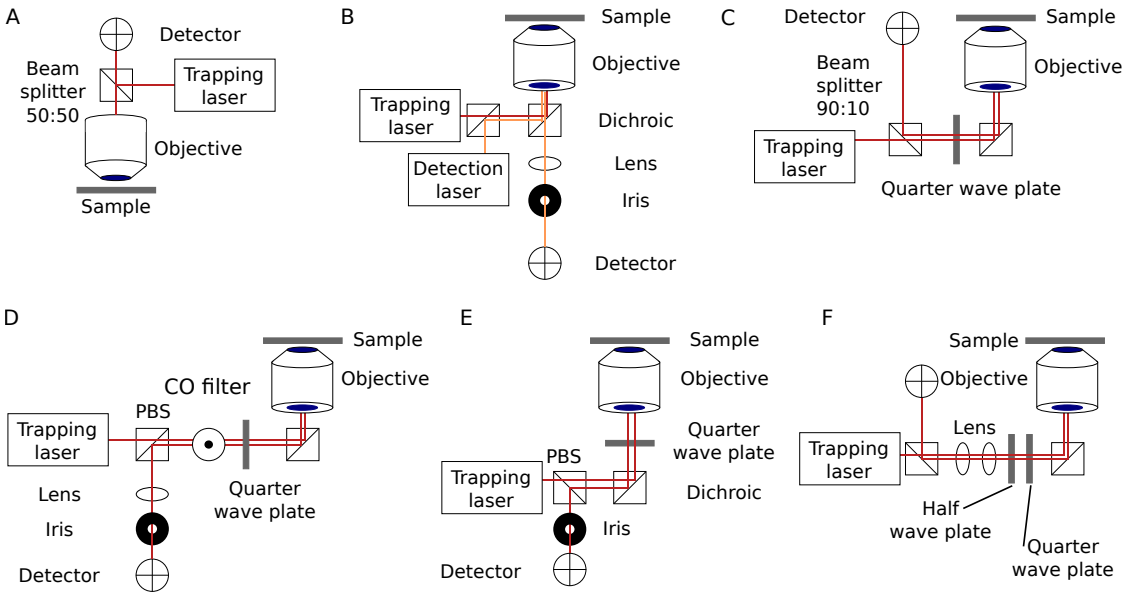

Fig. 2.2 | Existing optical designs for backscattering detection. Various optical designs have emerged based on beam-splitter (A-[48] & C-[47]), separating detection laser and trapping laser (B-[55, 58]) or polarization based (D-[59], E-[60], F-[61]). All of them verified the functionality by either performing microsphere scans or calibrating the microspheres with a power spectrum.

advantage is its simplicity with the shortcoming of loosing 50 % laser light for trapping and loosing 50 % of the backscattered signal. From experiments on existing custom system in the lab we know that experiments at 50-100 % laser power are common. Because of the reduction in maximum laser power, I did not consider the beam-splitter configuration for my system later on. In 1998 Shivashankar et al. [55, 58] suggested a different approach for backscattered detection by using a second wavelength to probe the microsphere position. They used a 830 nm laser for the optical tweezers and a second 633 nm laser for the detection of backscattered light from the trapped microsphere. The isolation of backscattered signal is achieved by using common dichroic mirrors projecting the light though a pinhole onto a QPD. The pinhole serves as a spatial filter, as in confocal microscopy. Since I wanted to combine two colour fluorescence with an optical tweezers, this configuration was also not favourable for my optical design. We planned to use Rhodamine B, which has an emission spectra in the region of the detection laser. In 2005, Huisstede et al. [47] used polarization optics to provide circular polarized light. Circular polarization results in an equal trap stiffness in both lateral directions[62]. For backscattered signal isolation a 90:10 beam splitter was used this providing more laser power for trapping but reducing the backscattered signal as a trade-off. An interesting new approach was tested by Sischka et al. in 2008 [59] with the implementation of a central obstruction filter. This central obstruction filter is placed in the incident trapping laser and blocks the center of the laser beam, thereby preventing a backscattering of light around the optical axis from reflective interfaces causing unintended interference effects [63]. Here, isolation is based on polarization. The incident laser light is linearly polarized (p-polarized) and passes the polarizing beam splitter (PBS). After the CO filter, the light passes a quarter wave plate and thereby changes its polarization to right-handed circular polarized light. Backscattering changed the light to left-handed circular polarized light. After exiting the objective the quarter wave plate converts the backscattered light into s-polarized light that is reflected by the PBS onto a detector with a lens and a spatial filter. A simpler approach is shown in Fig. 2.2E from Shipley et al. by using a similar polarization mechanism in 2012. Here, only an iris is used in front of the detector. Contrary to Sischka et al., the central portion of the laser beam is used to quantify the detector response. It has been stated that an iris is not required for all experimental conditions. Depended on the amount of backscattered signal from a glass-medium interface, an iris can improve the lateral sensitivity by isolating the central portion of the laser beam. In 2017 Ramaiya et al. [61] have shown that the backscattered signal can be used to measure rotational signals of birefringent microspheres as well as torque on these particles.

After evaluating our options, testing and optimizing we finally decided for a different approach shown in Chapter 2.3.3.4, which is, to my knowledge, a novel combination of the polarization based isolator for back reflected light, a central obstruction filter in the detection laser path, and back focal plane interferometry.

2.2.3. Optical tweezers calibration

The previous chapter dealt with the actual signal collection, which provides a displacement of the microsphere projected in some way or another on the detector in units of volt. To convert this voltage signal into a displacement in physical units or into a force, a calibration is necessary.
Three parameters need to be calibrated: first, the trap stiffness κ, second, the displacement sensitivity β, and third, the drag coefficient γ. The displacement sensitivity can be determined with a so-call microsphere scan. A microsphere, immobilized on the glass surface for example, by increasing the salt concentration to 100 mM KCl, will be scanned in all three axes with a closed loop piezo stage. From the scan, we can identify a linear region, where we can fit a linear function and extract the slope. The inverse of this slope is the displacement sensitivity β in units of volt per nanometer. The trap stiffness can be determined by the analysis of Brownian motion. The particle within the trap is exposed to the Brownian motion. This causes a certain variance $\langle x^2 \rangle$ in the detected displacement time signal. The measured variance can be related to the thermal energy and the trap stiffness by the so called equipartition theorem [41, 64]:

$$< x^2 >= \frac{k_B T}{\kappa}, \tag{2.2.2}$$

with T the temperature and k_B the Boltzmann constant. The drag coefficient can be assumed by the size of the microsphere and the temperature of the sample. Note that the full bandwidth well beyond the corner frequency needs to be measured. Otherwise, the signal is low pass filtered leading to an overestimated κ. A more novel approach to calibrate can be made by analysing the power spectrum of a trapped microsphere. Here the power spectrum can be described as a Lorentzian [65]

$$P(f) = \frac{D}{\pi^2(f_c^2 + f^2)} = \frac{k_B \cdot T}{\gamma\pi^2(f_c^2 + f^2)} \tag{2.2.3}$$

with D the diffusion coefficient, and the corner frequency $f_c = \kappa/(2\pi\gamma)$. The diffusion coefficient according to the Einstein-Stokes relation can be written as

$$D = \frac{k_B T}{\gamma}, \tag{2.2.4}$$

with γ being the drag coefficient for a spherical particle in a fluid with a low Reynolds number. The Lorentzian fit provides two values, a plateau value and the corner frequency. To calculate

$$\kappa = 2\pi f_c \gamma \tag{2.2.5}$$

and

$$\beta = \sqrt{\frac{kT}{\gamma D_{Volts}}}, \tag{2.2.6}$$

we have to know the drag coefficient γ. The drag coefficient can be determined by an additional sinusoidal oscillation applied by a closed loop stage with a know amplitude [66]. It is necessary to know the peak-to-peak amplitude of the oscillation. The oscillation is visible as a sharp peak in the powerspectra and appears as an additional term modifying Eq.2.2.3 to the following expression (from Eq.(9) in Tolić-Nørrelykke & Schäffer et al. [66])

$$P(f) = \frac{D}{\pi^2(f_c^2 + f^2)} + \frac{A^2}{2(1 + f_c^2/f_{drive}^2)}\delta(f - f_{drive}) \tag{2.2.7}$$

with A being the amplitude of the sinusoidal driving frequency f_{drive}. Since I will perform experiments near the surface additional effects have to be taken into account, which are not covered by the simple description above. The drag coefficient depends on the distance of the microsphere to the wall of the sample chamber [27, 67]. This height dependency can be measured in good agreement with Faxén's law [68]. Additional hydrodynamic corrections [66] are implemented because of interactions of a infinite plane with a microsphere. These corrections improve the accuracy of the calibration and are combined in the here used python based software [69] called "pyotic".

2.3. Results

2.3.1. Optical design overview

The optical design of the custom setup is optimized for the planned experiments. The key features are optical tweezers for mechanical manipulation and calibration of microspheres. Florescence microscopy is used to observe labelled proteins and lipid bilayer membranes in two colours, here optimized for GFP and Rhodmaine B. LED-based interference reflection microscopy is used to visualize non-labelled components of the sample like microspheres. The temperature feedback with sub-millikelvin precision allows a significant reduction of sample drift. Designing the instrument was challenging with four lasers (1450nm, 1064nm, 561 nm, 488 nm) and a LED (450 nm) combined for excitation and detection though a single objective (CFI Apo TIRF 60× oil, NA 1.49, Nikon Instruments). The space above the objective was used for a sample chamber with a simple microfluidic tube system. The tube system is used to immobilize the vesicles on the sample surface. To further improve the stability of the system an enclosure for the optics is divided into sub enclosures (i-vii) (Fig. 2.3). Heat generating components are removed from the interior. Most of the dichoric mirrors (DM) and filters have been acquired from AHF Analysetechnik (Tübingen, Germany), a list can be found in the Appendix A.3. Mirrors, lenses, lens mounts, rails, rail mounts, manual translation stages

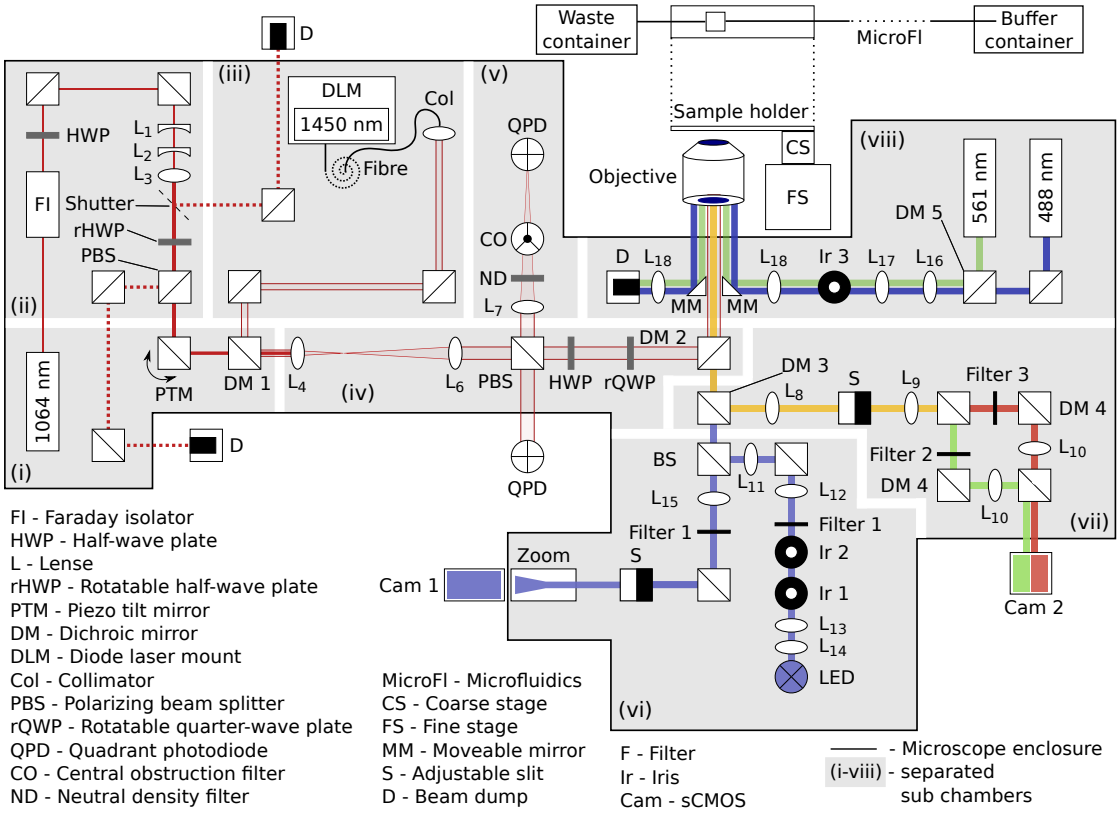

Fig. 2.3 | Custom setup, complete laser-light path. The setup is optically isolated with black construction cardboard (TB4, Thorlabs, USA). I added sub chambers into the setup's enclosure to separate potentially heated components on the table that could induce air convection. (i-v) contains the infra-red laser path of the optical trapping laser and the heating laser. (vi) marks the IRM path for with an LED for illumination. For thermal stability, camera 1 is placed on the outside of the setup's enclosure. (vii) shows the fluorescent detection path for two colour detection. Camera 2 is also mounted on the outside of the setup's enclosure. (viii) is the fluorescent excitation path with two lasers for TIRF, tilted EPI illumination and EPI. The distances between lenses and other components are not drawn to scale.

and standard other opto-mechanical components were acquired from Qioptic Photonics (Göttingen, Germany), if not stated otherwise. Custom mechanical components have been constructed with a CAD software (SolidWorks, Dassault Systemes, France). All components interacting with visible light, Fig. 2.3 sub enclosure (vi-viii), are mounted on an optical table (1000×1200×200 mm, 1HT10-12-20, Standa, Lithunia). An additional smaller optical table (600×600×70 mm, 1HB06-06-07, Standa, Lithunia) on top of the previously mentioned table contains the optical trap and the heating laser components (Fig. 2.3 sub enclosure [i-v]. The following sections will give detailed description of each feature combined into a hybrid optical tweezers.

2.3.2. System control and data acquisition

The custom built instrument is a combination of multiple opto-mechanical devices that need to be controlled remotely by the user. Most of the devices have been shipped with a proprietary software or a LabVIEW (National Instruments, Austin, USA) program provided by the manufacturer. To provide an overview of the system components, I sorted features on the left side of Fig. 2.4 and then show how the interactions are performed via a PC indicated by the connecting arrows. Data exchange is realized via USB, RS 232, PCIe, or analogue control and monitor signals integrated in a corresponding controller. The main component for data acquisition and analogue/digital control of devices is a NI PXI-1033 chassis equipped with four cards (NI-4472B, 2x NI-6221, NI-6733, National Instruments, Austin, USA). The major functions of the system are optical trapping, temperature control, sample movement, florescence microscopy (TIRF, tilted illumination and epi), interference reflection microscopy (IRM). A list of the used cards, power supplies, sensors and other devices providing technical details can be found in the Appendix A.3. After sample insertion, the system is completely motorized and can be remotely controlled via a LabView interface or other software.

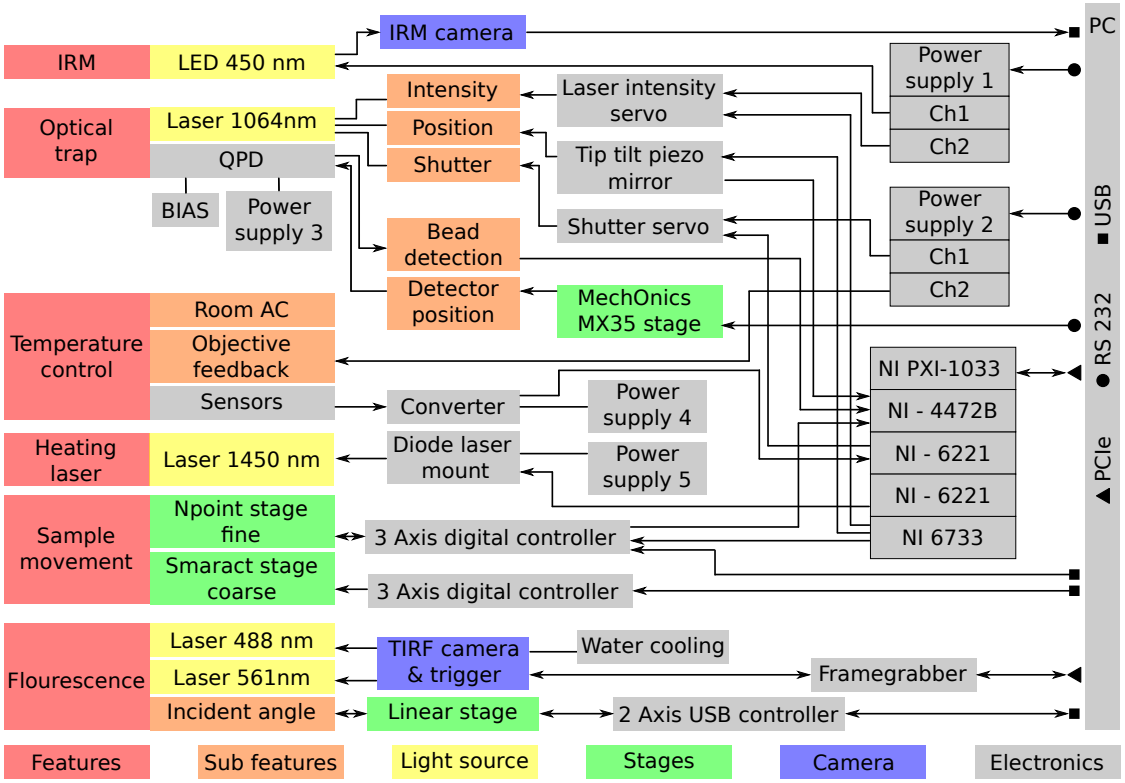

Fig. 2.4 | Setup control diagram. Shown are the features of the system on the left side and how the user interacts via the PC on the right side with the components. The direction of arrow indicates the information flow between devices.

2.3.3. Design of the optical tweezers

2.3.3.1. Trapping laser characteristics

The essential part of any optical trap is a focused laser beam. We use a 1064 nm continues wave laser with 3 W (SmartLasers Systems, Diode pumped Nd:YVO4, 3W cw). The laser is linearly polarized with the polarization orientation perpendicular to the optical table. The laser provides has the necessary stability for the planned experiments, which has been rigorously checked by colleagues using a similar [22] or equal model [24]. Therefore, stability controls will not be shown here. Intensity and pointing stability are important because any fluctuation will destabilize the trap position and induces noise to the system. To ensure a equilibrated system the laser is on continuous duty. In Fig. 2.5A the current-power(IP)-curve of the system has been verified after installation using a power meter (power-meter PM10, Coherent, USA) infront of the exit pupil. We also measured the laser power at 0.5 m and 1 m distance and recorded a loss of 7 % in laser emission. We attribute the loss of intensity to stray light that is leaving the laser cavity uncollimated. Since the power meter does not discriminate between wavelengths, some of the extra power may have originated from the pumping diode. We can use 2.86 W measured directly before the objective for trapping. The beam diameter has been measured with a beam profiler (Cinogy Technologies, Germany) at a distance of 1 m from the exit-pupil. The beam profile is shown in Fig. 2.5B with the marked major and minor axis. The $1/e^2$ value for a Gaussian fit resulted in a major width of 0.58 mm and a minor width of 0.49 mm. The corresponding line profiles are shown in Fig. 2.5C&D. The Gaussian beam profile has a beam quality factor $M^2 = 1.18$.

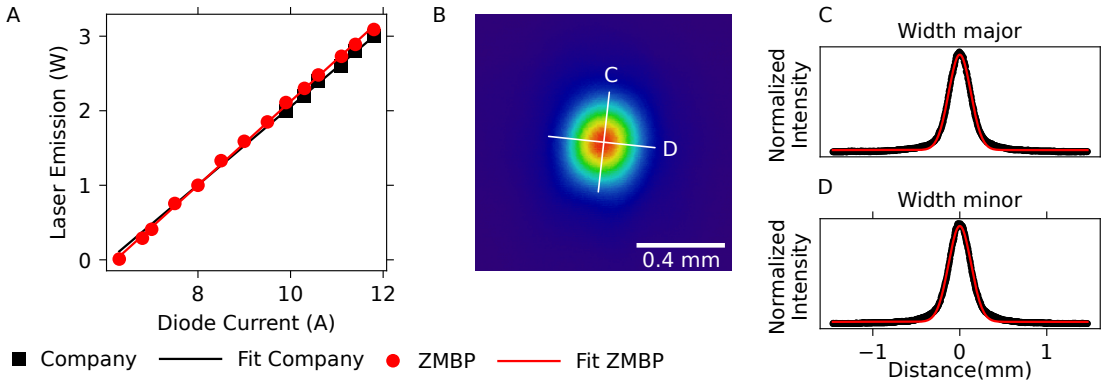

Fig. 2.5 | I-P curve and beam profile of trapping laser. (A) IP curve - shows how much power the laser emits at a certain pumping diode current. (B) The beam profile of the trapping laser. The lines show the minor and major axis of the laser profile. (C,D) Intensity profiles and fits for the major and minor axis shown in (B).

2.3.3.2. Trapping laser path

The laser path is illustrated, with accompanying pictures, by a dashed and solid red line in Fig. 2.6. First, the laser passes a Faraday isolator (FI, IO-3-1064-VHP, Thorlabs, USA) to prevent back reflections into the laser cavity [70] from upstream optics. For precise positioning we used two translation mounts with micrometer screws. The FI has been aligned for maximum transmission, specified with 0.928 by the manufacturer. We measured a transmission of

$$\eta_{FI} = 0.925\,\% \tag{2.3.1}$$

with the previously mentioned power meter. Since the FI rotates the polarization by 45 ° the polarisation is restored to its original orientation by a half-wave plate (HWP), after the FI. Two mirrors are used for precisely reorienting the laser to the optical axis. We use dielectric mirrors, which have different relativities depending on the polarization. The half wave plate's reorientation of the polarization axis prevents elliptic polarization [71]. This could cause an asymmetric trap potential. After the mirrors, a three lens Galilean beam expander with f_1 = -100 mm, f_2 = -100 mm and f_3 = 80 mm magnifies the beam to a diameter of 3.5 mm ($1/e^2$) characterized by the beam profiler. The advantage over a two lens Kepler telescope is the avoidance of a laser focus point. A focus point may heat the air and cause convection that can destabilize the optical trap or cause additional noise. The next component is a shutter: a mirror prism connected to a servo (RS-2 Servo, Modelcraft) that reflects the incoming laser. If the laser beam is shuttered, it is guided out of the system to minimize thermal drift close to any optics when using the shutter. In the next Chapter 2.3.3.3, I will document the calibration of a polarization based laser intensity adjustment unit that follows. A piezo tilt mirror (PTM, TT2.5, Piezoconcept, France), on which a mirror is mounted, reflects the light towards the dichroic mirror (DM1). There the heating laser and the trapping laser are combined. The following Kepler telescope projects the tilt of the PTM into the back focal plane of the objective resulting in a lateral movement of the focus in the image plane. The range of this movement can be estimated by [72].

$$\Delta r = 2 f_{Obj} \frac{f_4}{f_6} \Delta\theta = 13.32\,\mu m \tag{2.3.2}$$

with f_{Obj} = 3.33 mm, f_{L4} = 80 mm, f_{L6} = 200 mm and $\Delta\theta$ = 5 mrad. The very same telescope magnifies the laser beam by a factor of $M_{4,6} = 2.5\times$ to 8.8 mm. The following combination of PBS, HWP and QWP acts as a filter for backscattered light, later described in Chapter 2.3.3.4. The incident trapping light is further reflected by DM2 into the objective and forms the optical trap.

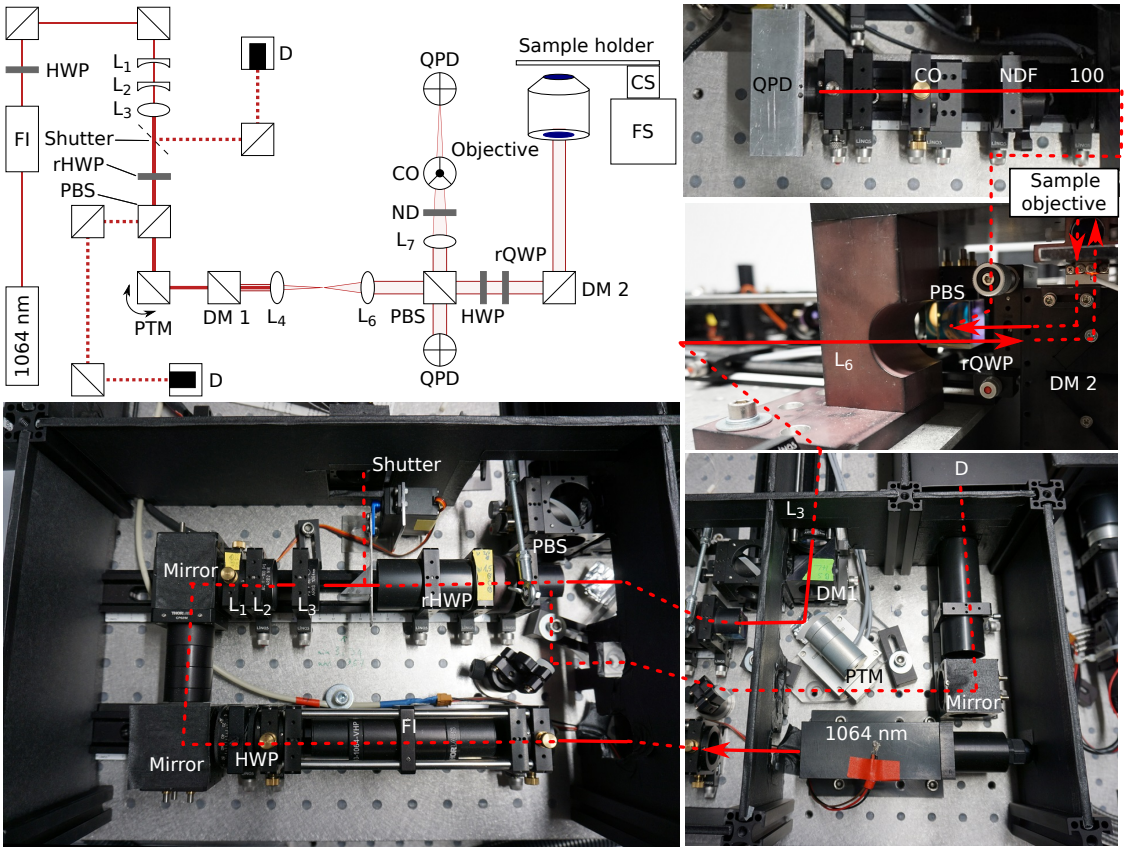

Fig. 2.6 | Optical tweezers setup. Schematic and foto of the components forming the optical tweezers. The red line indicates the laser path.

2.3.3.3. Laser intensity adjustment

It is possible to adjust the laser intensity by neutral density filters, continuously variable metallic filters or by using a HWP and PBS, similarly implemented by Huisstede [47] et al. As a cost efficient laser intensity adjustment unit, we use a remotely controlled servo (RS-2 Servo, Modelcraft) attached to a bearing via a lever. A change of the orientation of this HWP changes the fraction of laser light that is transmitted and reflected from the PBS. The reflected light is guided out of the microscope enclosure into a beam dump. The geometry shown in Fig. 2.7A results in a non linear transfer of servo motion to intensity change briefly described here. For each absolute servo position, I recorded the laser intensity that was has transmitted (Fig. 2.7B). The inverse intensity was fitted with a polynomial function

$$p(x) = a_0 + \sum_{i=1}^{9} a_i \cdot x^i. \tag{2.3.3}$$

The determined constants a_i are entered into a LabView VI. Another test has been performed to verify the correct calibration of the system by measuring the laser power. This overall laser power control solution provides a better thermal stability since the unused fraction of light is dumped outside the enclosure compared to reflection based ND filters with partial absorption.

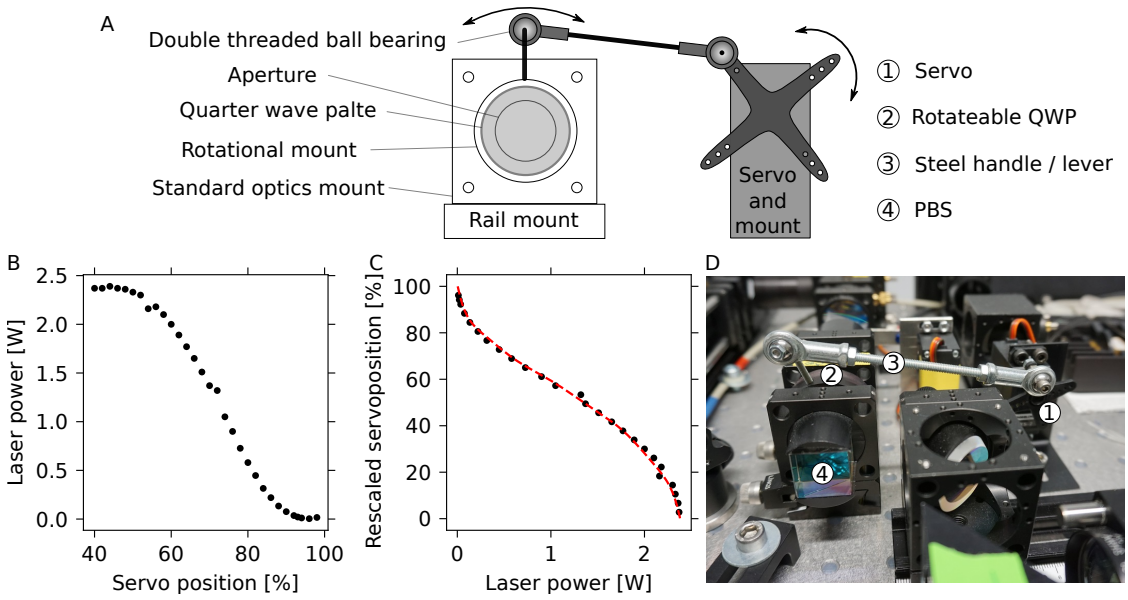

Fig. 2.7 | Laser intensity servo calibration. A, Schematic of the non-linear rotation transfer to the half-wave plate. The double threaded ball bearings allow for easy implementation. B, shows the non-linear response curve for a fraction of the servo positions. Between 50 and 80 servo position we have a fairly linear behaviour with a good adjustment for the laser intensity. For very high and very low laser intensities we can see a flattening of the response. One should be aware of that in these areas intensity changes might suffer on precision and reproducibility. C, Inverted polynomial fit for conversion. D, Image of the intensity adjustment unit.

2.3.3.4. Backscattered detection of a trapped micro sphere using a central obstruction filter

First, the backscattered light has to be isolated from the incident trapping light. We choose a polarization based isolation. The incident trapping laser is transmitted by the PBS, only p-polarized light can pass, after the telescope (L4&L6). The linear p-polarized light gets converted by a QWP into circularly polarized light. The combination of a HWP and a QWP mounted to a high precision manual rotational stage allows to maximize the backscattered signal. After the QWP, the light is reflected by DM 2 into the objective, forming the optical tweezers and for a trapped particle scattering light. The reflected light is collected by the objective. Compared to the incident light the reflected light experienced a phase shift of π. By passing the QWP, this phase shift translates into a linear s-polarization of the backscattered light and is now reflected by the PBS onto the QPD (QP154W-HVSD, First Sensor AG, Germany). The image of the back focal plane is projected with a lens ($f_7 = 100\,\text{mm}$) onto the sensor, thereby using back focal pane interferometry[46, 49] for measuring displacements of a trapped particle. To account for different laser intensities and to prevent saturation and damaging the QPD one can change a neutral density filter, which is mounted in a slider (Filter Support C, Quioptiq). Additionally a central obstruction (CO) filter has been implemented at the position one focal length from the relay lens. How the time signal of a trapped particle is affected is shown in Fig. 2.8A&B. The oscillations or unknown noisy fluctuations have been reduced to a typical noise level for a microsphere of this size. The initial 3D printed CO filter is made out of polylactide (PLA), a typical material for printers. We assumed a transmissiblity in the infra-red spectrum of 80-95 % [73] and there fore added a metal screw in the central region of the CO filter for filtering. The overall signal was reduced by 60 %, which was estimated by comparing the QPD-Z signal. With this filtered signal, I tested the detector response for an immobilized microsphere (Fig. 2.9). The microsphere scan was performed in all three axes. The linear range was fitted with a linear function shown as a red line in the second row of Fig. 2.9 for each axes. Clearly visible are oscillation in all three axis, especially in the residuals. I measured a linear range of $x_{range} = 400\,\text{nm}$, $y_{range} = 370\,\text{nm}$ for the lateral and $z_{range} = 1300\,\text{nm}$ for the axial direction. Since it has been reported that interference effects can occur in the backscattered detection, we investigated this effect in more detail. The interference of backscattered light from the microsphere and other back reflections from the sample surface or optics in the laser path cause an oscillation in the axial detector response of a trapped microsphere [59]. The used CO filter reduced the oscillation significantly(Fig. 2.10). The inference has a wavelength of $\approx 500\,\text{nm}$. The oscillation remained superimposed, but the amplitude was reduced. One can also identify an increased crosstalk between the axial axes and the lateral axis. Besides analysing the effect of the CO filter on the time signal, I calculated the Allan deviation [74, 75] of a trapped microsphere

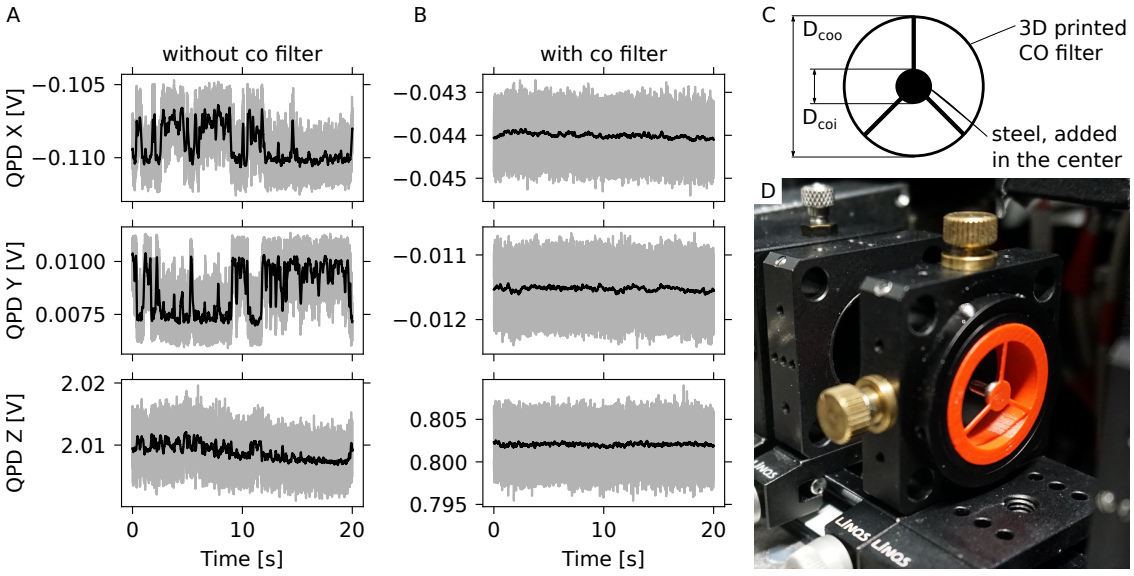

Fig. 2.8 | Time trace of a trapped microsphere at a fixed height before and after insertion of a central obstruction filter. A, time signal without a CO filter shows high fluctuations or even a flipping between two different positions. B, adding a CO filter clears the signal from fluctuations. C, Shape of the CO filter. Due to the high transmission rate of 1064 nm light for PLA, the used plastic, I added a steel screw with a diameter of D_{metal} =5 mm to the center. Dimensions of the filter:D_{COO} = 25mm, D_{COI} =5 mm. D, Picture of the CO filter.

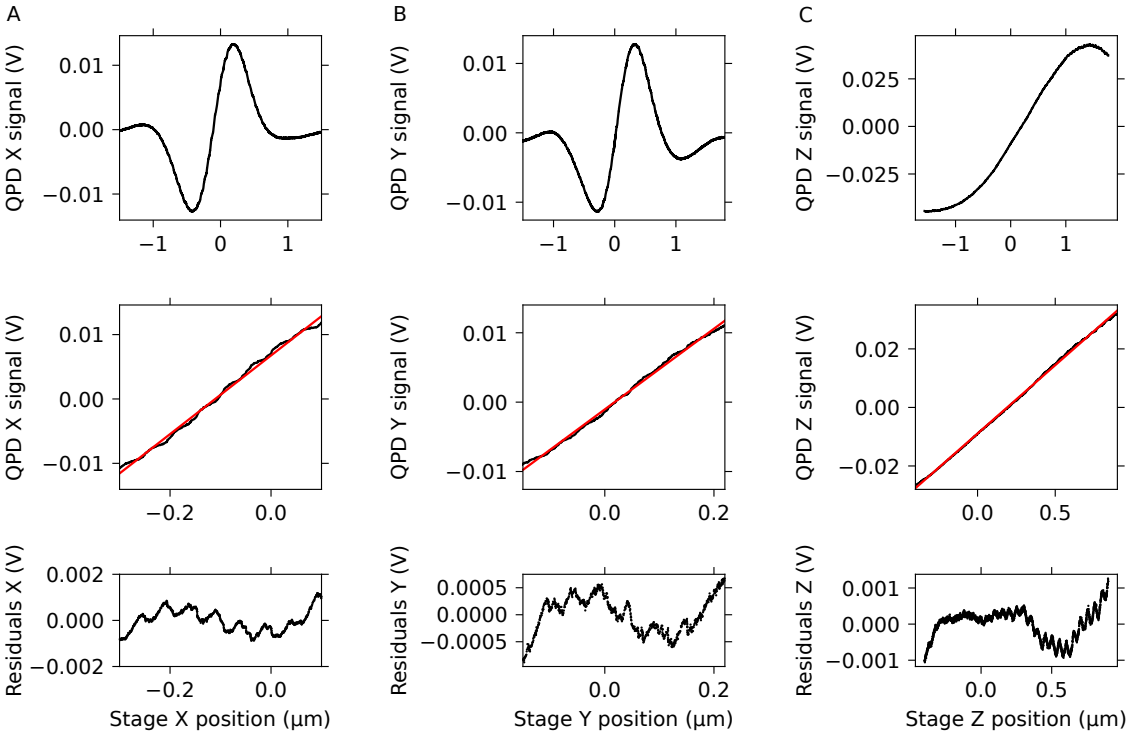

Fig. 2.9 | Bead scan of a fixed microsphere in backscattered detection mode. Shown is the detector response for all three axis. The second row shows a zoom into the linear response range with a linear fit. The last row shows the residuals for the corresponding axes.

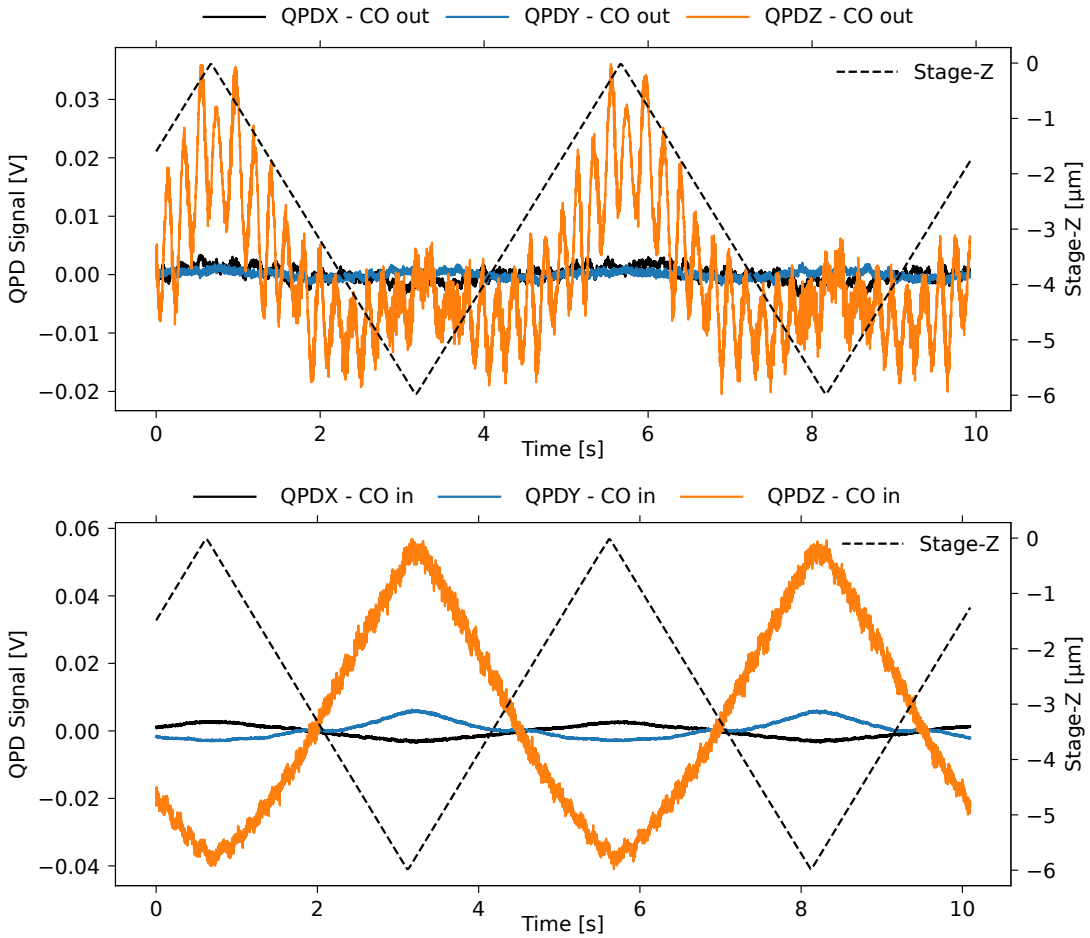

Fig. 2.10 | z-scan of a trapped microsphere in solution, with and without a CO filter. The z-scan without a CO filter shows a dominant oscillation with wavelength of about $\approx 500\,\mathrm{nm}$, which is approximately half the wave length of the trapping laser. The implementation of the CO filter reduced the oscillations to a tolerable amplitude.

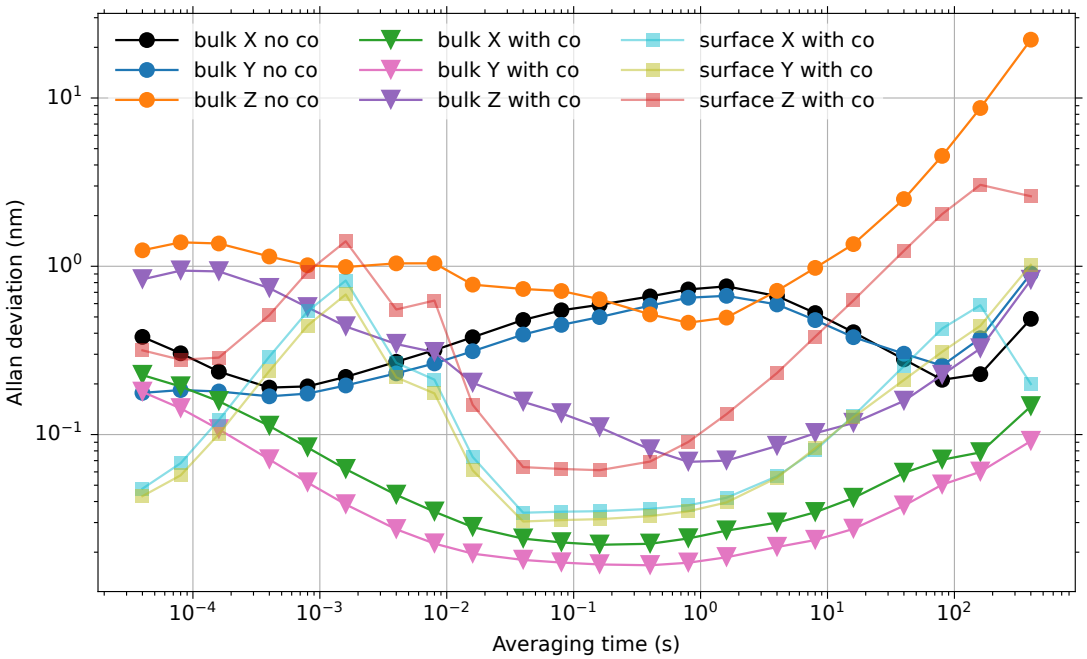

Fig. 2.11 | Allan deviation of trapped microsphere at fixed height with and without CO filter. Adding a CO filter improved the precision below the Å-level and shows a minimum around 0.2 s. Experimental paramaters $\kappa_x = 0.887\,\mathrm{pN/nm}$, $\kappa_y = 0.824\,\mathrm{pN/nm}$, $\kappa_z = 0.411\,\mathrm{pN/nm}$, $T = 301.35\,\mathrm{K}$, microsphere radius $r = 410\,\mathrm{nm}$.

(Fig. 2.11). The implementation of a CO filter allows to reach sub-Å noise levels for averaging intervals ranging from 0.001 s to 100 s. All measured axes show a characteristic drift behaviour at longer averaging times.

2.3.3.5. Microsphere height calibration using backscattered detection

The calibration of microspheres is performed by a PSD analysis. I performed a so-called height calibration [68] using the software package pyotic [69], where one can analyse the height dependence of β and κ. First a microsphere is trapped and the height roughly adjusted to about 3 µm above the surface. I recorded every a PSD 50 nm, the sample has been moved with the closed loop piezo stage in the axial direction moving toward the surface. This dataset of PSDs at different heights is automatically analyzed and fitted with the used python based software package. The measured height dependence can then be used in experiments to correct for a changing height while an experiment is performed. For working at a fixed height, a single PSD calibration is sufficient. A single PSD out of the dataset is shown in Fig. 2.12A. We can observe a corner frequency for x of $f_c = 1578\,\mathrm{Hz}$, y of $f_c = 1484\,\mathrm{Hz}$ and z of $f_c = 315\,\mathrm{Hz}$ axial. The corresponding diffusion coefficients are $D_x = 0.0063\,\mathrm{V}^2/\mathrm{s}$, $D_y = 0.0044\,\mathrm{V}^2/\mathrm{s}$ and $D_z = 0.0154\,\mathrm{V}^2/\mathrm{s}$. The difference in stiffnesses for the lateral axes visible in Fig. 2.12D. For circular polarized light they should be exactly the same for both axes. The asymmetry is a indicator for a slight ellipticity of the trapping light. The fine tuning of the backscattered signal was performed using birefringent microsphere that rotate at high frequencies for circular polarized light, kindly provided by Avin Ramaiya [61]. The last QWP before the objective in the trapping laser path is mounted on the high precision manual rotational mount. The signal has been optimized for the maximum rotation frequency of the microspheres. Therefore the backscattered light reaching the detector is higher with the trade-off of a small ellipticity that induces a lateral asymmetry in the trap stiffness. In summary, demonstrated that the backscattered detection mode is functional for back focal plane interferometry detection by making use of a CO filter.

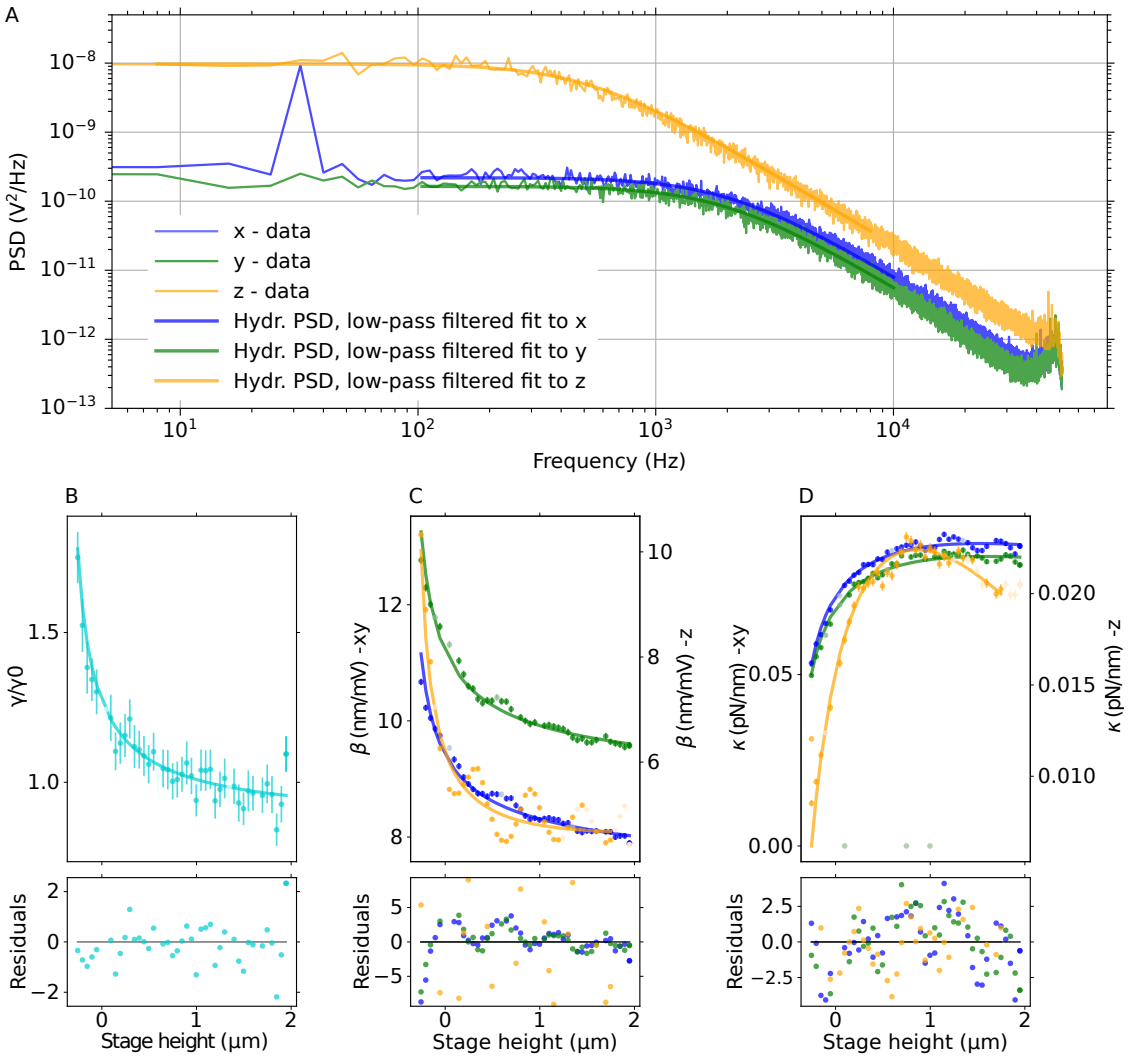

Fig. 2.12 | Optical tweezers height calibration. (A), Single PSD at one height out of the data set. (B) Typical height dependent drag coefficient. (C & D), The height dependence of β and κ. Due to interference effects, there is still an oscillation visible in all three axes.

2.3.3.6. Step response

To estimate the sensitivity of the system, I performed a so called step response experiment. In this experiment, I prepared a sample with cleaned glass slides, Protocol B.1. The washed 820 nm polystyrene microspheres are mixed with KCl to a final concentration of 100 mM. Under these conditions , microspheres bind to the surface . An immobilized microsphere ws then centered in all three axis using the piezo translation stage. Subsequently, a microsphere scan was performed to extract the displacement sensitivity. Further, we applied a square wave with an amplitude of 3 nm peak to peak and a frequency of 0.2 Hz. The recorded microsphere position and the stage movement are shown in Fig. 2.13. The minimal step size that can be applied though the controller card is 1.53 nm with a 16 bit resolution (NI-6733) and a travel range of 100 µm. Although I used a voltage divider to reach Å-level bits and below, I could not resolve smaller step sizes. This is in contrast to the measured Allen deviation (Fig. 2.11).

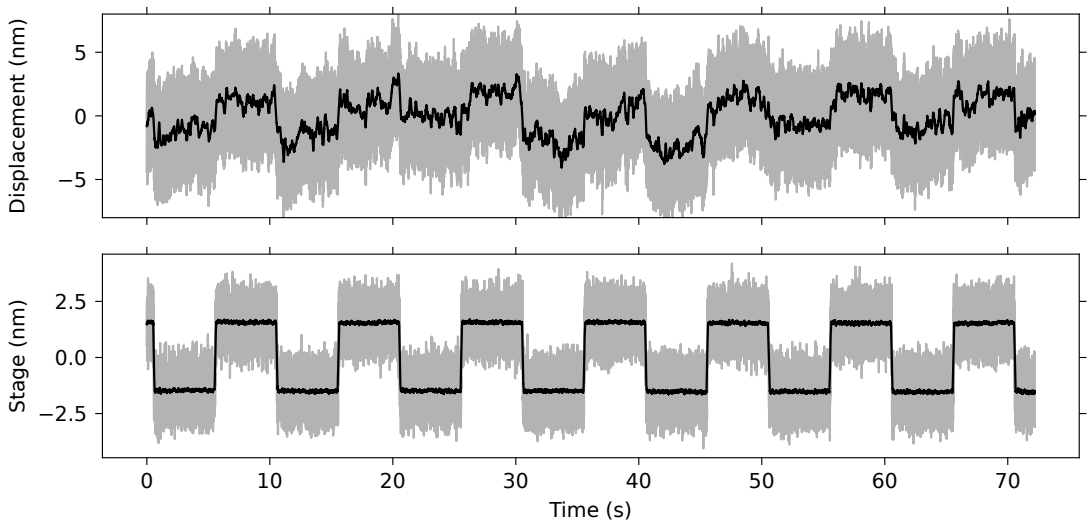

Fig. 2.13 | Resolution limit of the optical trap measured with a fixed microspheres step response. Shown is the displacement of a 820 nm microsphere with a square signal of the sample stage of 3 nm. Data is displayed at a sampling frequency of 25 kHz - grey, and filtered with a running mean to 10 Hz - black.

2.3.4. Design of the fluorescence microscope

The design of this fluorescent microscope unit is based on an objective coupled method utilizing a small rod mirror[52]. I will use GFP or similar marker in the green channel and Rhodmanie B as a marker in the red channel. Therefore, I used two diode lasers for excitation with $\lambda_{exGFP} = 488\,\text{nm}$ (100 mW, LuxX 488-100, Omicron-Laserage, Germany) and $\lambda_{exRh} = 561\,\text{nm}$ (100 mW, OBIS 561LS-100, Coherent, USA). The lasers are combined with a dichoric mirror (DM5, H488LPXR, AHF Anaysentechnik, Germany) and magnified by a telescope with $f_{16} = 30\,\text{mm}$ and $f_{17} = 100\,\text{mm}$. The magnification

$$M_{16-17} = f_{17}/f_{16} = 3.33\times \tag{2.3.4}$$

increases the laser diameters from about 1.3 mm to 4.3 mm. To provide a uniform sample illumination, we block the inhomogeneous edge of the magnified beam with a 1 mm diameter pinhole. Resulting in a maximum illumination difference between the center and the edge of the beam of less then 10 %. With this pinhole being projected into the back focal plane of the objective, we get an illumination sample area with a diameter of

$$d_{exci} = d_{beam}\frac{f_{Obj}}{f_{18}} = 41.6\,\mu m \tag{2.3.5}$$

with $f_{Obj} = 3.33\,\text{mm}$ and $f_{18} = 80\,\text{mm}$. This diameter is in agreement with the measured diameter of 42.8 µm for the excitation field. This limited illuminated area reduces photo bleaching of the sample. The small rod mirror (2 mm in ∅, Edmund optics) that is guiding the light into the objective is mounted on a linear stage (SLC-1730-M-E linear stage, CU-3DM-USB-TAB controller, SmarAct, Germany) on each side. It provides a travel range of 18 mm with an internal hard end stop and a step resolution of 100 nm. By mounting the lens L_{18} together with the rod mirrors (Fig. 2.14), we keep the optical path length constant, if we move the linear stage and thereby adjust the evanescent field depth. All lenses in the excitation laser path are made of fused silica. This should avoid any autofluorescence from the optics. Thereby we did not use additional clean-up filters. The movable mirrors can be set to an position where total internal reflection generates the evanescent field or to a position where a tilted illumination can be used similar to epi illumination.

The fluorescent emission light from 510 nm to 680 nm is collected and guided towards the camera unit with dichroic mirror DM3 (500DCSPRX, AHF Analysentechnik, Germany). This mirror is followed by a 1:1 telescope with $f_8 = f_9 = 100\,\text{mm}$, to generate a conjugate plane to the image plane. In the image plane of this telescope, I positioned an adjustable rectangular slit (Spalte SP 40, Owis, Germany) that restricts the field of view down to half the size of the camera chip. The following unit has been developed by a Steves Simmert [24] who kindly provided the

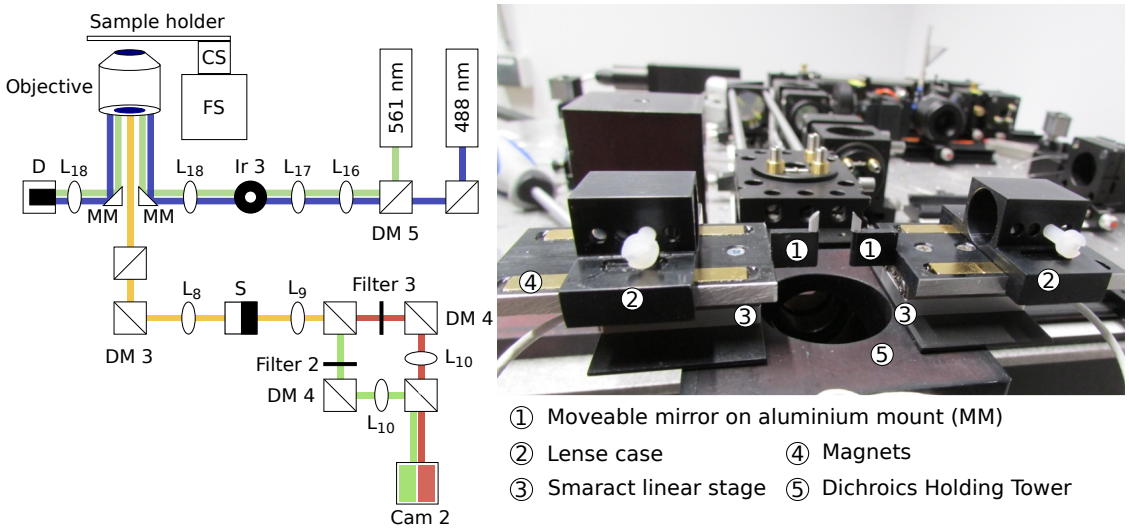

Fig. 2.14 | Fluorescence excitation and detection schematic. For excitation, we two lasers with 561 nm and 488 nm are available for TIRF or tilted illumination. The emission is collected between 510 nm and 680 nm and is split up at $\lambda = 560$ nm into two independent channels being projected on one sCMOS camera.

CAD drawings for my modifications. This unit is splitting the light at a wavelength of 560 nm using a dichroic mirror (DM4, HC beam splitter BS 560 Imaging, AHF Anaysentechnik, Germany). For each channel, a corresponding bandpass filter is implemented – Filter 2 (ET Bandpass 520/40, AHF Anaysentechnik, Germany) and Filter 3 (Bandpass Rhodamine 605/70 ET Bandpass, AHF Anaysentechnik, Germany). Two lenses (f_{10} =300 mm) focus each channel independently on the camera, the mirrors in the corners are used to position the separate images next to each other. The magnification, we achieved, is

$$M_{fl} = f_{10}/f_{Obj} = 300/3.33 = 90.1\times \tag{2.3.6}$$

The camera (Orca Flash 4.0 V2, Hamamtsu, Japan) has 2048×2048 pixel with a pixel size of 6.5 µm. With the 2x2 binning mode the final resolution is 70 nm/pixel. The camera and both lasers are controlled though the µManager [76]. The lasers are triggered via the camera's internal trigger outputs. The laser power can be controlled via the USB interface of the lasers. This control is combined in the software, where data acquisition patterns and videos can be recorded.

2.3.5. Design of the LED-based IRM

The LED-based IRM [53] is a simple alternative to differential interference contrast [77], phase contrast [78], darkfield [79] or iSCAT [54] and provides high contrast [80]

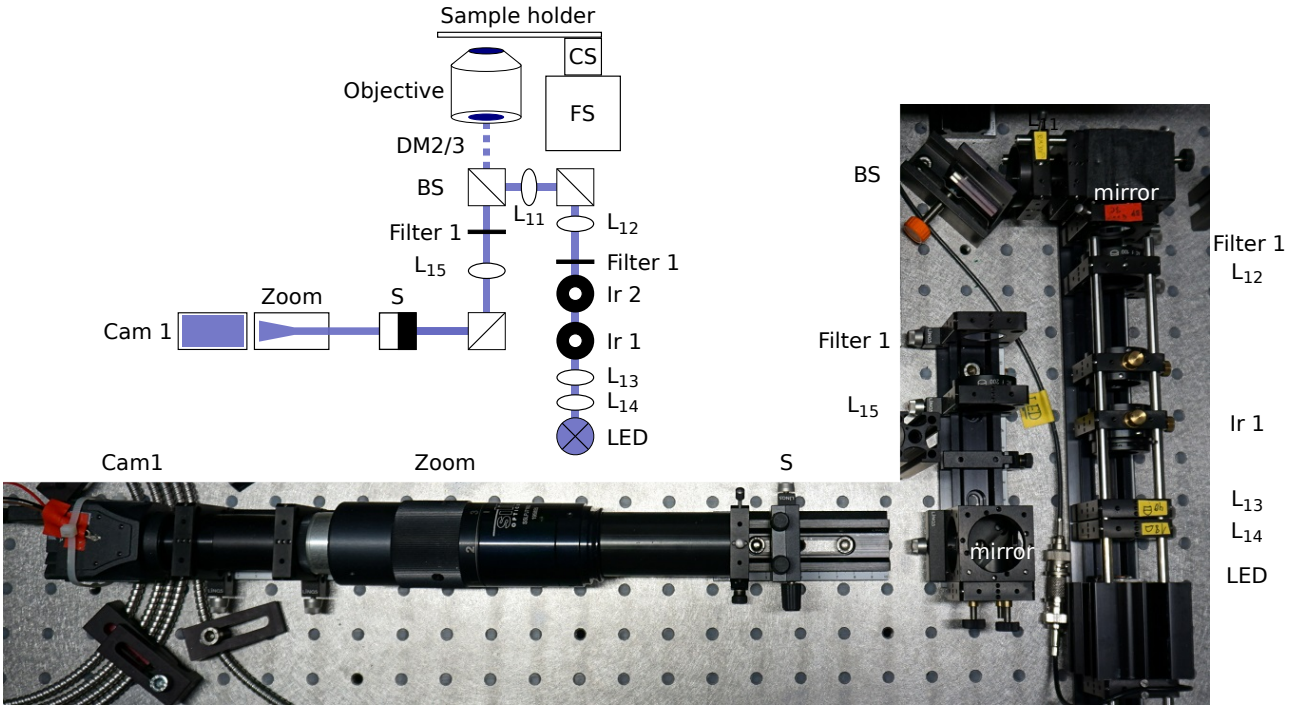

Fig. 2.15 | IRM design and implementation. The LED light is collimated and projected into the back focal plane of the objective to provide Köhler-illumination. Backscattered light is collected by the same objective and projected onto the camera.

for biological samples. I choose this method because its a reflection based design and operates with blue LED light suitable for implementation into the setup. The implemented LED-IRM provides sufficient contrast to image single microtubules, GUVs and membrane tethers - label free. The optical design has been explained in detail elsewhere [53]. For illumination I used a blue LED (Royal-Blue, LUXEON Rebel LED, Lumileds, Germany) with 450 nm ± 20 nm for mounted on an aluminum heat sink (Fisher Elektronik, Germany). To control the LED's brightness, we actuate the current provided by a DC power supply (Agilent E3648A, Keysight, Böblingen, Germany). The following lenses were used $f_{12} = 100\,\text{mm}$, $f_{13} = 40\,\text{mm}$, $f_{14} = 18\,\text{mm}$ and $f_{15} = 200\,\text{mm}$. The LED is magnified by two telescopes projecting the LED's image into the objective's back focal plane for Köhler-illumination. About 50 % of the light is reflected into the objective using a 50:50 splitter (50R/50T beamsplitter VIS, AHF Anaysentechnik, Germany). 50 % of the backscattered light collected by the objective is transmitted by the beam splitter. By implementing Filter 1 (ET Bandpass 450/30, AHF Analysentechnik, Germany), we block backscattered infra-red trapping light, fluorescent excitation and emission light that can leek though DM 2. After Filter 1 the tube lens crates

a image plane with 60 × magnification. In this plane I positioned an adjustable rectangular slit (Spalte SP 40, Owis, Germany). The following zoom (S5LPJ7163, WD front 93 mm, Sill Optics, Germany) provides a magnification from 0.7 ×-4.9 × with a standard C-mount connection to the camera (Lt225, 2048×1088 pixel, pixel size 5.5 µm x 5.5 µm, Lumenera, Canada).
I used the IRM setup to visualize microspheres for the later discussed experiments. For test purposes I imaged unlabelled microtubules, surface bound GUVs, staphylococcus aurelius, and blood platelets attaching to the surface. To illustrate the imaging power of IRM, Fig. 2.16 shows examples of the latter samples. Even for microtubules and GUVs a high contrast is achieved.

2.3.6. Design of heating the laser path

Local temperature control utilizing a heating laser has been used to study the effect of thermophoresis [81, 82] and in its applications for quantification of protein binding affinities [83, 84]. I want to use the local heating to adjust the membrane tension of an immobilized GUV. Increased membrane tension reduces the radius of a pulled membrane tether. For local temperature control we implemented a diode laser (QFBGLD-1450-150, QPhotonics, USA) with a wavelength of 1450 nm. This laser diode was mounted on a butterfly diode mount (LM14S2, Thorlabs), which is connected to an OEM laser diode/TEC Controller (ITC100D, Thorlabs, USA). The laser light is coupled into the system by a collimator (Col, F810APC-1550, Thorlabs, USA) with a focal length of $f_{col} = 37.13$ mm and a numerical aperture of 0.24. The beam diameter 0.7 mm was measured by Moritz Burmeister during my supervision of his bachelor thesis [85]. The heating laser is magnified by a factor of

$$M_{HL} = f_6/f_4 = 2.5\times \tag{2.3.7}$$

to a diameter of 1.75 mm. The laser is projected into the sample with the first order airy disk radius

$$r_{ariy} = \frac{1.22\lambda}{2\mathrm{NA}} = 2.37\,\mu\mathrm{m} \tag{2.3.8}$$

using a wavelength λ =1450 nm and a numerical aperture of NA = 0.39. The objective is not optimized for this wavelength and absorbs most of the heatinglaser's power. I measured a transmission of

$$\epsilon = I_{excident}/I_{incident} = 20mW/142mW = 0.141 \tag{2.3.9}$$

using a microscope slide power sensor (S170C, Thorlabs, USA). The heating laser's wavelength is within a spectral range that none of the cameras are sensitive to. Also, we cannot detect it with the 1064 nm infrared optimized QPD for backscattered signal of the optical tweezers. For coarse alignment, a detector card for infrared (VRC2, Thorlabs, USA) is sufficient. Since the objective is a very strong lens, fine

adjustments was necessary. We used the induced convection and 800 nm diameter tracer silica microspheres that follow the convection in solution, Fig. 2.16D. For a well aligned laser the microspheres follow the convective flow to the center of the focus in a symmetric fashion, illustrated with a schematic provided in Fig. 2.16C. The symmetry is further illustrated by the arrows in Fig. 2.16D&E, the kymograph of the dashed line.

2.3.7. Temperature profile generated by the heating laser

The previously induced convection is a quantitative indicator for a temperature increase accompanied bye monitored particle movement. A qualitative characterization of temperature gradients has been performed with a temperature sensitive flourophore [81]. The temperature sensitivity increases from a 10 mM TRIS buffer, which changes its pH with temperature. The flourophore 2',7'- bis - (2-carboxyethyl) - 5 - (and-6) - carboxyfluorescein (BCECF) is pH sensitive at 50 µM with a reported temperature sensitivity of s_{lit} = -2.8 %/K. We performed a control measurement with another temperature controlled fluorescent microscope in epi. A linear fit provided us with a temperature sensitivity of $s_{exp} = (-2.8 \pm 0.6)\,\%/K$ (Fig. 2.17A). To record the temperature gradient, we filled a thin sample with a height of ≈ 10 µm to prevent convection [82]. The raw intensity profile suffered from an inhomogeneous illumination of the sample with the IRM LED used for excitation of BCECF and dust particles on the optics. We applied a bleaching correction and normalized the image to a background image without the heating laser. This allowed us to extract radial averaged intensity profiles (Radial Profile Plot,FIJI plugin, Fig. 2.17B) from the corrected fluorescent images in Fig. 2.17D. The intensity profile decrease can now be converted into a temperature increase based on the previously determined calibration factor s_{exp}. This conversion is shown in Fig. 2.17C for the radial averaged line profile and is also visible Fig. 2.17D as a temperature coded image. As a control for the temperature, I applied the temperature gradient to melt a lipid bilayer made of 1,2-Distearoyl-sn-glycero-3-phosphocholine (DSPC, Avanti Lipids, USA) with a phase transition temperature of 55 °C. To visualize movements within the supported lipid bilayer, the fluorescent dye DIO has been added during the formation (Protocol B.4). The sample temperature was set to 26 °C with the temperature control. At 93 % heating laser power, movement of DIO in the SLB became visible. Based on the phase transition temperature we can achieve a temperature of 60 °C for 100 % heating laser power. This maximum temperature is well in agreement with the fluorescent image quantification.

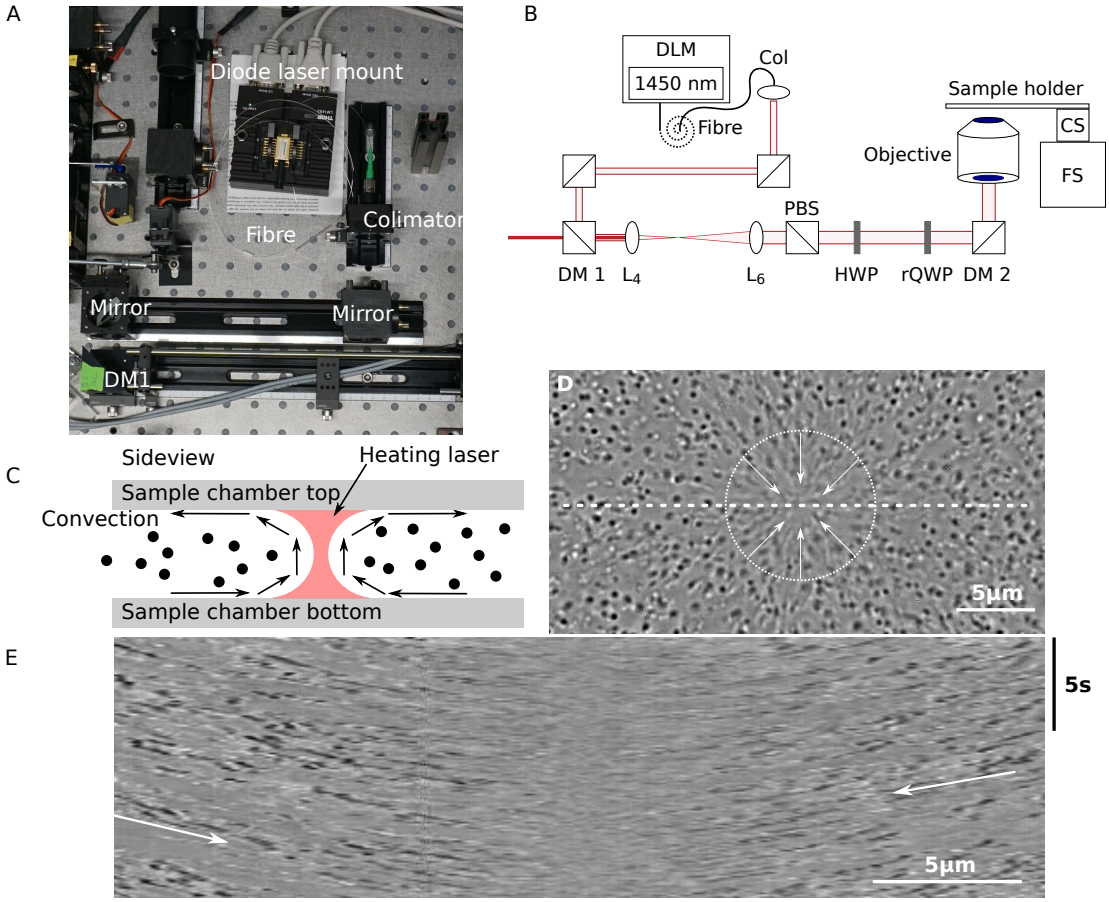

Fig. 2.16 | Heating laser, schematic and alignment procedure via convection of microspheres. A, Photo of the laser path illustrated the schematic in B. C, Schematic of the experiment illustrating the movement of the particles. D, One frame of a convection movie with the center of the field of view marked. In the center is the heating laser causing convection. C, Kymograph of the dashed line shown in D. Particles move out of focus. Therefore the visible traces are short. A symmetric flow of particles to the center is used as a indication for an proper alignment of the heating laser.

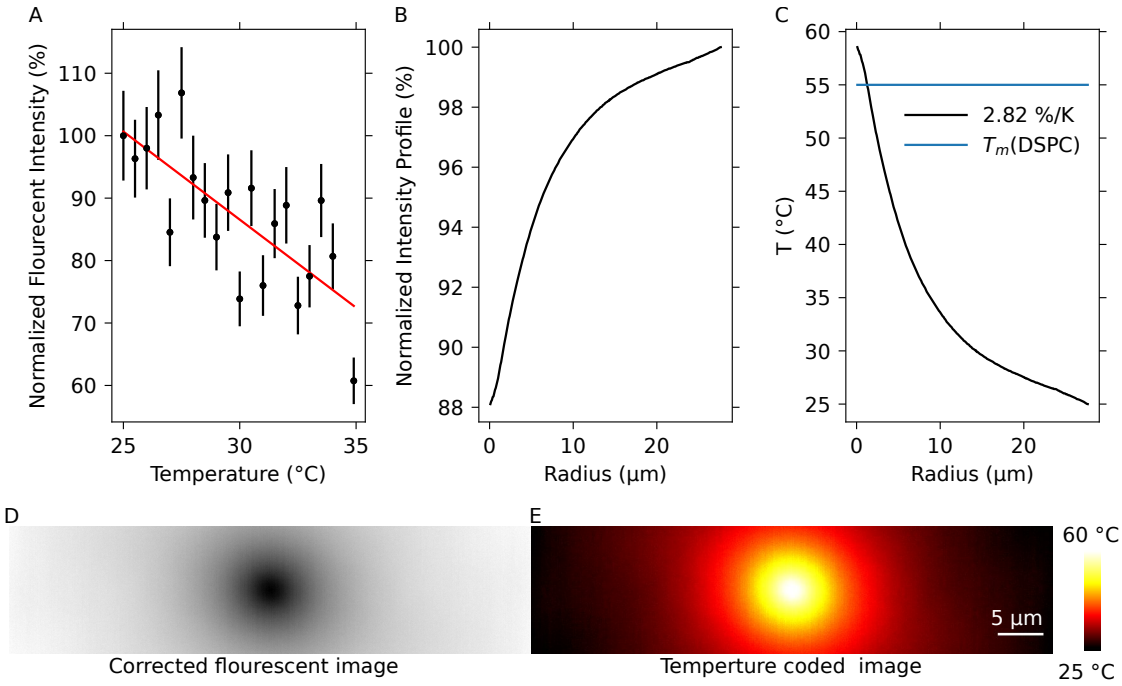

Fig. 2.17 | Heating laser temperature profile. A, Normalized fluorescent intensity of the flourophore BCECF at different temperatures. B, Normalized intensity profile, radially averaged around the center of a heating laser. C, Temperature-converted line profile of the heating laser. D, Fluorescent image of the BCECF with the heating laser after image corrections. E, Temperature encoded image of BCECF with the heating laser at 100 %.

2.3.8. Sample stage position stability

For optical tweezers calibration, a closed loop piezo translation stage was used to apply a sinusoidal motion during calibration. Additionally, this stage is used for quantitative displacements during experiments. We use a piezo stage (NPXY100Z50-244, Npoint, USA) in combination with a digital 3 channel controller (LC.403 3-CH DSP, Npoint, USA). The travel range of the stage is 100 µm for the lateral axes and 50 µm for the vertical axis. The company specifies the stage with 0.3 nm rms positional noise and a resonance frequency of 500 Hz and 550 Hz for lateral and vertical directions respectively. On top of this fine piezo stage, a coarse stage for sample positioning (12 mm travel range, 3x SLC1720, SmarAct , Germany) is mounted (Fig. 2.20). To evaluate the limit for positional noise the stability of the stage is important. Also, I test the limit of the system to detect displacements. Most of the experiments are planned directly at the surface or very close to the sample surface. Mechanical stability is important here, since disturbances are directly transmitted. To evaluate the performance, the representative time signals of each axis is converted into physical units with the provided conversion factors of 5 µm/V and 2.5 µm/V for the lateral and vertical axes, respectively (Fig. 2.18A). I calculated a rms noise for the three channels of $rms_x = 0.90$ nm, $rms_y = 0.83$ nm, and $rms_z = 0.46$ nm which larger compared to the values provided by the company. However, for the company value of 0.3 nm, the bandwidth is unclear. Furthermore it is possible to analysis these time signals in the frequency and time domain by calculating a PSD and the Allan deviation (ADV)[74, 75] respectively. A PSD visualizes the frequency information and its amplitude of a time signal. It is possible to identify electrical noise such as ground loops, which appear as sharp peaks, sometimes with overtones. Also, mechanical vibration noise can manifest itself with broad peaks in the PSD. In general, it is interesting to know to which extend averaging is going to improve the precision of a given quantity. This can be analyzed by the so called ADV [74, 75], given by

$$\sigma_x(\tau) = \sqrt{< (x_{n+1} - x_n)^2 >_\tau} \tag{2.3.10}$$

where x_n is the average value for the measured quantity over n - data points and τ the measurement time per sample. It is possible to correlate the slope of the ADV in a log-log plot with different types of noise [74, 86]. I measured the ADV for the monitor signals that show a minimum around 1 s with a ADV well below 1 Å for all axes. For longer averaging time, drift increases the noise level. Thus, knowledge of the ADV of a system allows to determine the optimal averaging time for an experiment. Axes drift was negligible with ≈0.0009 Å/s.

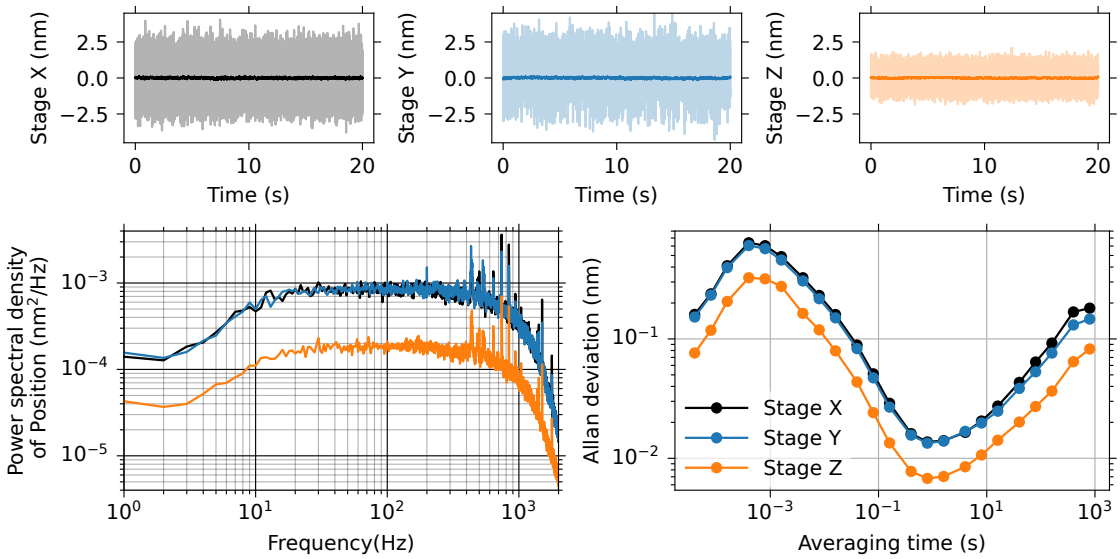

Fig. 2.18 | Noise level of piezo sample stage. A, Time trace of all three axes at a sampling frequency of 25 kHz filtered with a running mean to 10 Hz (dark lines). B, Power spectral density and C, Allen deviation for all three axes.

2.3.9. Tip tilt stage position stability

The tip tilt stage is used for moving the optical tweezers laterally in the image plane. As for the translation stage, the mechanical stability of the tip tilt stage is important for the overall precision that can be reached in an experiment. Therefore, the noise level of the used tip tilt piezo (TT2.5, Piezoconcept, France), with a range of 5 mrad and a resonance frequency of 4000 Hz has been measured. In Fig. 2.19 the time trace, PSD, and the ADV is shown. From Eq.(2.3.2) we can convert from the piezo sensor signal to a displacement in the image plane of the objective. From the time trace, I calculated a rms noise of $rms_x = 0.027\,\text{nm}$ and $rms_y = 0.026\,\text{nm}$ that will be transferred e.g. to the movement of a trapped microsphere. In the frequency domain, one can clearly see multiple sharp peaks starting from 4 Hz, with higher harmonics and 50 Hz also with higher harmonics. Due to the shape I assume that these peaks originate from the amplifier that scales the 0–10 V analogue control signal to −5–150 V to for driving the piezo. The position stability is even for 25 kHz below Å-level and therefore will not limit the precision of the instrument.

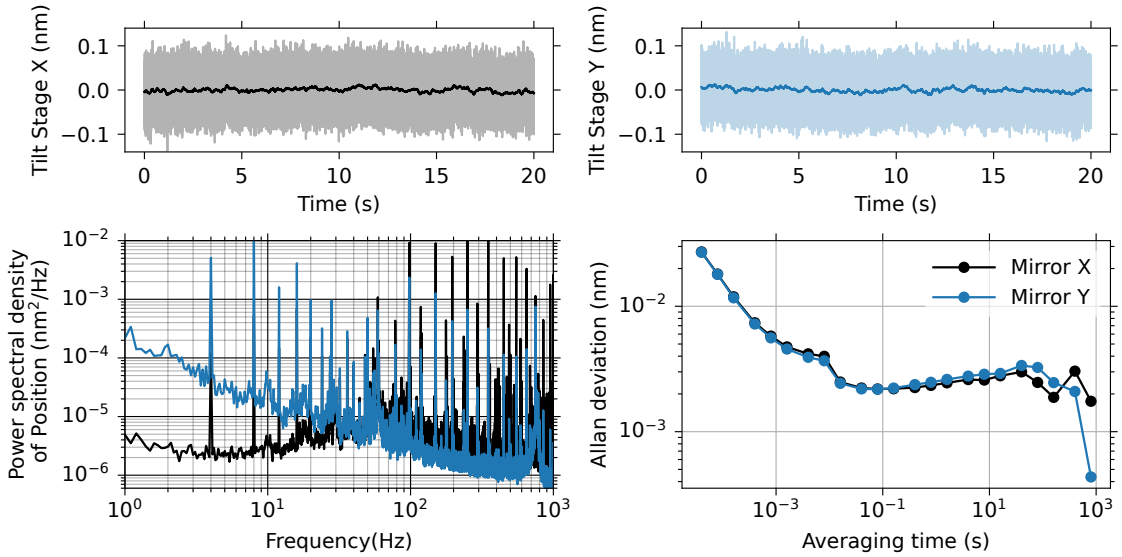

Fig. 2.19 | Noise level of the tip tilt piezo stage. Time trace, power spectral density, and ADV for both axes at a sampling frequency of 25 kHz and filtered with a running mean to 10 Hz.

2.3.10. Temperature control

Temperature stability or the reduction of sample drift becomes essential for high-precision microscopy and optical tweezers measurements. In the case of long-term measurements, temperature drift causes a loss of image plane focus. For optical tweezers temperature drift and drift in general cause a significant change in the drag coefficient that would lead to errors in forces. To illustrate the order of magnitude of the effect we assume a temperature fluctuation with a standard deviation of 1 mK. Temperature fluctuations cause a expansion of the objective by a certain thermal expansion coefficient of brass . An expansion ΔL with respect to the overall length of the object $L = 5.5\,\mathrm{cm}$ is calculated with the following relation

$$\frac{\Delta L}{L} = \alpha_L \cdot \Delta T. \tag{2.3.11}$$

For $\Delta T = 1\,\mathrm{mK}$ the objective expands by $\approx$1 nm shifting the laser focus by the same amount. Thus, milikelvin temperature changes can lead to nanometer-sized drift. To reduce such drift, I will present my efforts to implement and test a temperature control. The difference to previously installed versions [24, 87], this is a single objective feedback. We assumed that the previous sandwich structure of a double feedback with two high NA objectives would shield the sample more efficiently from temperature fluctuations. Here, we will show that the single objective feedback system provides the same temperature stability as the sandwiched configuration.

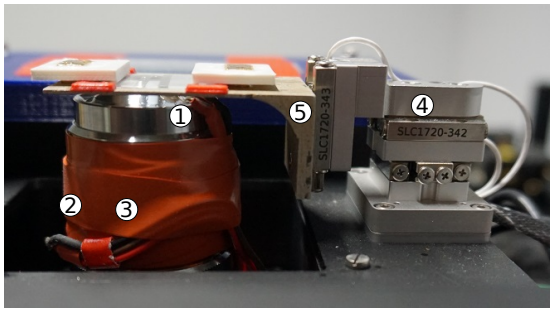

①② PT100 Temperture sensors
③ Heatingfoil
④ SmarAct sample stage
⑤ Sample holder

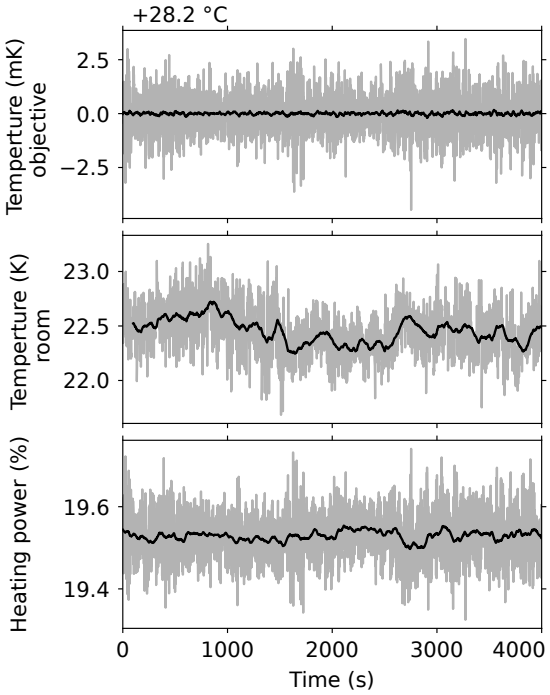

Fig. 2.20 | Temperature feedback implementation and stability. (A) Implemented feedback system. Sensors are glued to the objective with a two component thermal conductive glue. The heating foil is wrapped around the objective and held in place by an extensible rubber band. The feedback achieves a stability of 0.7mk over 4000 s at a set point of 28.2 ℃. Sampling frequency for grey was 0.25 Hz, filtered to 2.5 mHz (black line).

2.3.10.1. Implementation and stability

We used platinum temperature sensors (PT100, Omron, Germany) and analogue converters (PXT-10, 24V DC, Brodersen Controls, Denmark) to measure the temperature. The temperature sensors are fixed with thermal conductive glue on the objective (positions are marked in Fig. 2.20 with 1 and 2.) To heat the objective we used a heating foil ($2.5 \times 10.1\,\mathrm{cm}^2$, Telemeter, Germany) that is connected to a power supply (E3631A, Agilent, USA). The heating foil is wrapped around the objective and fixed with orange silicone rubber tape. The calibration of the temperature sensors and the procedure to optimize the PID feedback parameters are described elsewhere[24, 87]. Briefly, the analogue converters convert the temperature dependent resistance to a voltage, −50–100 ℃ correspond to 0–10 V. This voltage is measured differentially using two analogous inputs (NI6221 card). For calibration of these converters we use resistors (82 Ω, 100 Ω, 120 Ω, Vishay Beyschlag, Germany) with a low tolerance (<1 %). The linear conversion of the

resistance can be calibrated using the gain and the offset of the converters. For calibration, the resistors are replaced for the PT100 elements which correspond to a certain temperature(−45.73 ℃, 0.00 ℃ and 51.57 ℃). The lowest temperature/resistor will be used to adjust the offset and the highest temperature/resistor will be used to adjust the gain. The intermediate resistor will be used as a control data point. To control the temperature an existing temperature feedback VI program was used. The LabVIEW VI provides a PID feedback that has been optimized by the Ziegler-Nichols-Method [88]. The parameters are the set point temperature $T_{setpoint} = 28.2\,℃$, the proportional gain k_c =5, the integral time $T_i = 0.1\,\text{min}$ and the derivative time T_d =0.01 min. With these parameters, we measured a temperature of the objective of $T_{Obj} = (28.2000 \pm 0.0008)\,℃$ (standard deviation) while the fluctuations of the room were $T_{Room} = (22.5 \pm 0.2)\,℃$ over a time period of 4000 s. The measured standard deviations would correspond to a thermal expansion deviation of $\Delta L_{Obj} = 0.7\,\text{nm}$ and $\Delta L_{Room} = 552\,\text{nm}$.

2.3.10.2. Response times, relaxation and laser induced drift

To make an estimation how long one should wait for the setup to be equilibrated after, e.g., opening the shutter for trapping of a microsphere, I tested the response of the system to disturbances. First, for the case that the temperature control setup has been off for a certain time, I demonstrate the behavior for turning the control back on (Fig. 2.21A). After 40 min the system reached a stable state. However, from experience with the system, we know that the temperature control is slowly heating all components in the room and the room itself. After ≈2 days, we consider the system to be fully equilibrated. The slow relaxation is visible in the long decay of the heating foil power. In Fig. 2.21B, I demonstrate the step response for a change of the set point by 100 mK for a previously equilibrated system. After ≈5 min we reach similar standard deviations as before the set response. A typical situation during an experiment would use the optical trap at different laser powers as shown in Fig. 2.21C. Even though the feedback regulates the actual temperature within a few seconds we can still see a drift in the heating foil power for both trapping laser intensities (20 % and 50 %). The surrounding such as the objective mount, the microscope body and also the optical table has to adjust to the new temperature as well. To estimate the time constants for a system that is not temperature controlled, the feedback has been turned off (Fig. 2.21D,E and F). First, I tested how an equilibrated system reacts when the feedback is turned off (Fig. 2.21D). I fitted a double exponential with the time constants $k_1 = 1.24\,\text{min}^{-1}$ and $k_2 = 14.8\,\text{min}^{-1}$. The fast relaxation corresponds to heat dissipation of the objective, the slow to the objective mount. With the feedback turned off, I turned on the trapping laser at 20 % (Fig. 2.21E). The trapping laser heats the objective due to the poor transmission of ≈40 %[41] by ≈1.6 ℃ at 20 % trapping power. The time constants are in this situations $k_3 = 1.88\,\text{min}^{-1}$ and $k_4 = 64.2\,\text{min}^{-1}$. The

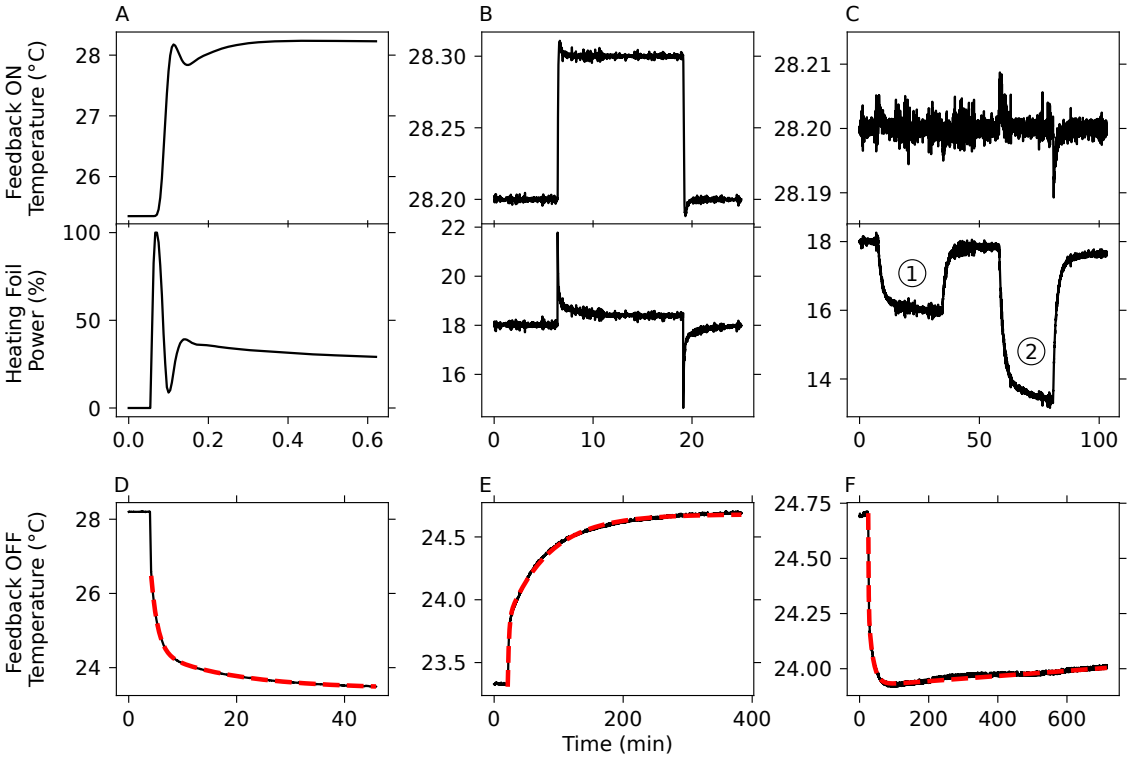

Fig. 2.21 | Temperature feedback dynamic response. A, Feedback turned on from the off-line state. B, Step response of a 100 mK set point change. C, Response for trapping laser turned on for different laser powers. ① - 0.57 W ② - 1.43 W . D, Relaxation times after temperature control fitted with a double exponential. E, Trapping laser induced heating without temperature control. F, Relaxation and drift shown after trapping laser was turned off.

heating laser can heat the objective by ≈0.15 ℃ with the feedback turned off, the time trace is not shown here. The time constants were comparable to the ones using the trapping laser. In the last situation, the trap was turned off. The temperature of the objective drifts unexpected after a fast exponential decay ($k_5 = 1.03\,\mathrm{min}^{-1}$ and $k_6 = 13.3\,\mathrm{min}^{-1}$) with a linear drift ($m = 2 \cdot 10^{-9}\,℃\,\mathrm{min}^{-1}$).

2.4. Discussion & conclusion

The novel optical tweezers system provides the following features that have been tested and verified for functionality.
First, optical trapping with a backscattered detection mode in a novel design was tested by performing a microsphere scan and a height calibration. The introduction of a CO filter in the laser path of the backscattered signal was the main improvement leading to a viable signal. The position of this CO filter is in the front focal plane of the objective since L_7 acts as a tube lens in this configuration. Yet we measure displacements in the back focal plane of the objective that is projected on the QPD. The corresponding time signal for a trapped microsphere without a CO filter showed a flipping between two states. Two states suggest a double trap produced by some sort of back reflection in the system. A second possibility is that we measure a certain rotational signal superimposed with the translational signal in the absence of the CO filter. Rotational signals were detected in an optical micro protector configuration similar to this design [61]. A flipping between two states means that two stable axes of the particle exist, maybe due to a small shape asymmetry in the trapped particles. The particles used here are made out of polystyrene, which has no reported intrinsic birefringence that would cause a torque transfer stimulated by the laser's polarization. Typically, polymer chains are randomly oriented, are optically isotropic, and thereby exhibit no birefringence[89]. As an example, though an exaggerated shape asymmetry, a poly(methylmethacrylate) nanofibers[56] or a rod like shaped structures [90] can exert a certain torque induced by an optical trap. There is the possibility that the polystyrene particles have a certain ellipticity, which induces something like a shape birefringence. The power spectrum of such an unfiltered signal, not shown here, showed a second Lorentzian-like plateau in the low frequency band. This plateau could easily be mistaken for low frequency noise, which is hard to investigate or may be assigned to suboptimal mechanical stability of the system and noise in general [91]. With the CO filter, the detection provided a linear response range that is similar ($x_{range} = 400\,\text{nm}$, $y_{range} = 370\,\text{nm}$, $z_{range} = 1300\,\text{nm}$) to the ones reported (300 nm lateral, 750 nm axial)[59] for backscattered detection and a CO filter. The step response measurement lacked the assumed precision in the Å-range. The thermal stability, position stability of the sample stage, position stability of tip tilt piezo and even the ADV from a trapped microsphere suggest that steps below 1 nm would be possible to resolve. However, it was not possible to resolve steps with smaller peak-to-peak step sizes than 3 nm. The backscattered signal suffered from interferences, that did not completely vanish with the implementation of the CO filter. If the measurement has been taken by chance at a certain height in a minimum of such an oscillation, the sensitivity would be reduced or even vanish. Placed in such a minimum, a displacement in either a positive or negative direction would not cause s detector response. This would mask the shape of the step response. Another possibility

is that in such a local minimum the displacement sensitivity is much small then the global sensitivity for lager displacements, which has been measured in a microsphere scan. In principle, the displacement sensitivity could even vanish in the center of the minimum.
Second the temperature control performs with a comparable performance as previously built systems [22]. We achieved a standard deviation of 0.7 mK over 4000 s, even though the system is basically open an unshielded for convection above the sample. This might be a point to improve the system: a proper convection block above the sample.
Third, by the implementation of an additional heating laser, we achieved a local heating capacity of $\Delta T \approx 35\,^{\circ}\mathrm{C}$ on sub-second timescales. This has been verified by a temperature sensitive flourophore and the phase transition of DSPC, which has been indirectly observed with a florescent marker diffusing in a supported lipid bilayer (SLB). The current implementation is a stationary heating laser. While performing experiments, it turned out a lateral steerable heating laser would be useful.
Fourth, the implemented imaging methods, IRM and the fluorescent path with TIRF/tilted illumination, complemented the backscattered methods. The mirror-based fluorescent system has a certain advantage for the choice of lasers. In principle, every excitation wavelength could be chosen since this path is decoupled from the imaging and trapping laser path. The trade-off here is that a certain amount of emission light is cut off by the mirrors. The evanescent depth of the TIRF field has not been calibrated so far. The excitation profile could be measured by tilted microtubules[92].
By combining fluorescence, an IRM microscope, a heating laser, a sub-millikevlin temperature feedback with an optical tweezers system we have constructed a advanced system that allows new exciting experiments. First we will use this combined optical tweezers system to perform experiments on membrane tubes in the next chapter. In the subsequent chapter, interactions of the membrane binding protein DPR1 with such tethers will be investigated.

Part III.

Membrane tethers: pulling via optical tweezers & membrane tension tuning via a heating laser

3. Tether pulling with DOPC vesicles

3.1. Introduction

The formation of membrane tethers has been first observed for red blood cells attaching to a glass substrate [93]. Further investigations discovered tubular networks in vivo and in vitro formed by membrane associated membrane proteins moving along micro tubules [94–98]. It is possible to pull single or multiple membrane tethers a variety of experimental techniques such as hydrodynamic flow [2, 99], atomic force microscopes [100–102], magnetic tweezers [103, 104] as well as optical tweezers [3, 4, 105–110]. Optical tweezers have been used to extract membrane tethers from neuronal growth cones and other cells and measuring length depended extrusive forces[111–113]. The previously mentioned formed tethers have been mostly membranous, lacking cytoskeletal components like actin or microtubules[114, 115] and are generated in *in vivo* studies. The first innovative *in vitro* method originally developed by Heinrich and Waugh [1] allowed to generate a single membrane tether with a diameter of 10–100 nm. This has been achieved by aspirating a giant unilamellar vesicle with a micro pipette and pulling a tether with a micrometer sized microsphere by magnetic tweezers. This method has been mostly used with optical tweezers instead of a magnetic tweezers in more recent years [3, 4, 105–110]. Using the insight from these studies, considerable efforts have been made to understand membrane tube formation in theory and experimentally [116–121]. The free energy of a pulled membrane tube from a GUV aspirated by a micro pipette can be written as [120, 122–124]

$$\mathcal{F} = \int \frac{\kappa}{2}(2H)^2 dA + \sigma A - pV - fL \tag{3.1.1}$$

where $\mathcal{F}$ is the free energy, σ the membrane tension, p the pressure inside relative to the outside, A the surface area of the vesicle, V the volume of the vesicle, κ the bending rigidity, H the mean curvature of the membrane. At a vanishing pressure difference $p = 0$, and a length L of the tube with a radius R and a force f to generate the tether, the free energy can be written as

$$\mathcal{F}_{tube} = \left[\frac{\kappa}{2R^2} + \sigma\right] \cdot 2\pi RL - fL \tag{3.1.2}$$

The membrane tension acts to reduce the radius of the tube, while the bending rigidity favors flat membranes. Minimizing the free energy with

$$\frac{\partial \mathcal{F}}{\partial R} = 0, \frac{\partial \mathcal{F}}{\partial L} = 0, \tag{3.1.3}$$

we can obtain a relation that only depends on the tension σ and the bending rigidity κ of the system.

$$R_0 = \sqrt{\frac{\kappa}{2\sigma}} \tag{3.1.4}$$

$$f_0 = 2\pi\sqrt{2\sigma\kappa} \tag{3.1.5}$$

with typical values for lipid bilayer membranes for $\kappa \approx 40\,\mathrm{pN\,nm}$ and $\sigma \approx 0.05\,\mathrm{pN/nm}$, one can find a radius $R_0 = 20\,\mathrm{nm}$ and a force $f_0 \approx 12.6\,\mathrm{pN}$[120]. In practice, the membrane tension is adjusted by the micro pipette. The membrane tension itself can be calculated form the aspirated portion of the GUV, i.e. the geometry of the system [125]. By recording the force f_0, from a calibrated optical tweezers for different tensions it is possible to extract κ by plotting f_0 over $\sqrt{\sigma}$ and fit a linear function. With κ and σ one can calculate R_0, for example demonstrated bye Sorre et al. [3](Fig. 2A). Since I will not use a micropipette, we do not have the possibility to use the mentioned procedure. I will present an alternative that allows to determine R_0 from the fluorescent intensity and with that value with the once from the force measurements performed with optical tweezers.

3.2. Materials & methods

3.2.1. Microsphere functionalization

For the experiments in the following chapters, I used polystyrene microspheres (diameter = 820 nm, Bangs Laboratories) that were pre-carboxylated. These microspheres were functionalized by a single step peptide cross-linking of NH_2 groups with EDC and NHS. The crosslinking mechanism is described in Bugiel et al. [23, 126]. The protocol has been developed by Marcel Ander[127] and Tobias Jachowski. Here, a 2kDa PEG(122000-2, Rapp Polymere GmbH, Germany) is used in combination with a rhodmaine antibody (anti-tetramethylrhodamine, rabbit, life Technologies, USA). The functionalized microsphere solution was stored at 4 ℃ and was stable up to 4–6 month. To verify the functionality, a complete tether pulling assay has been performed. A detailed protocol with comments can be found in the appendix under Protocol B.5.

3.2.2. GUV formation

The GUV formation protocol is based on electroformation [128], a commonly used version is the deposition of lipids on platinum wires [129]. A mixture of lipids dissolved in chloroform was deposited on two platinum wires (99.9 % platinum, 0.5 mm diameter, Goodfellow, England) of a custom made PTFE formation chamber shown in the appendix Fig. B.1. To remove remaining solvent, the lipid coated platinum wires were dried in a vacuum desiccator for 10 min. The PTFE formation chamber were then filled with a 150 mM sucrose solution and closed. The electroformation was performed in a heating block (Compact Drybath S 100-120V, Thermoscientific) at 45 ℃. The temperature was chosen to be above the phase transition temperatures of the lipids and above. To grow the vesicles I set the function generator (Function Generator, H-Tronic, FG 250 D or Voltcraft 7202 Sweep / Function Generator) to 10 Hz and 2.7 V with a sinusoidal signal shape for 2 h. To remove the vesicles from the platinum wires, I reduced the frequency down to 2 Hz for 1 h. The formation chambers were then removed from the hot plate to the lab bench to cool down to room temperature. To transfer the GUVs, a 1 ml pipette tip was cut off with a scissor to reduce shear forces induces by the water. The GUVs are then transferred into a fresh Eppendorf tube which contained 155 mM glucose and vitamin C as an oxygen scavenger[130]. For handling the GUVs it is always recommended to cut the tip of the pipettes tip. The used lipid mixtures(given in molar percentages) used in Chapter 3.3 contains 94.5 % DOPC, 5 % DSPE-PEG-Biotin, and 0.05 % NBD-PE. In Chapter 4.2 I used the so-called mitochondria mimicking lipid mix (MLL-mix) [131] with 48 % egg L-αphosphatidylcholine (egg PC), 26.1 % egg L-α-phosphatidylethanolamine (egg-PE), 9.9 % bovine liver L-α- phosphatidylinositol (PI), 10.05 % 18:1 phosphatidylserine (PS), 4.35 % cardiolipin (CL), 1 % L-α-phosphatidylethanolamine-N-(lissamine rhodamine B sulfonyl) and 0.1 % 1,2-distearoyl-sn-glycero-3-phosphoethanolamine-N-[biotinyl(polyethylene glycol)2000)] (biotin-PE). All lipids were obtained from Avanti lipids, USA. Further details are available in the appendix: a protocol for the formation (Protocol B.3) and a list of lipids (Table A.2).

3.2.3. Sample chamber preparation with supported solid lipid bilayers

The sample chamber consists of a spacer sandwiched between a 22×22 mm cover slide (#1.5, Corning) and a 18×18 mm coversilde (#0, Menzel). Both glass slides were cleaned with ethanol and mucasol in a sonicator according to Protocol B.1. The final geometry of the sample is depicted in Fig. 3.1 and shows a closed sample with a tube system attached (Protocol B.2). For membrane experiments, previously I tested [5] different sample constructions. For sample geometries without tubings, I was not able to insert GUVs into the sample without destroying a majority of the

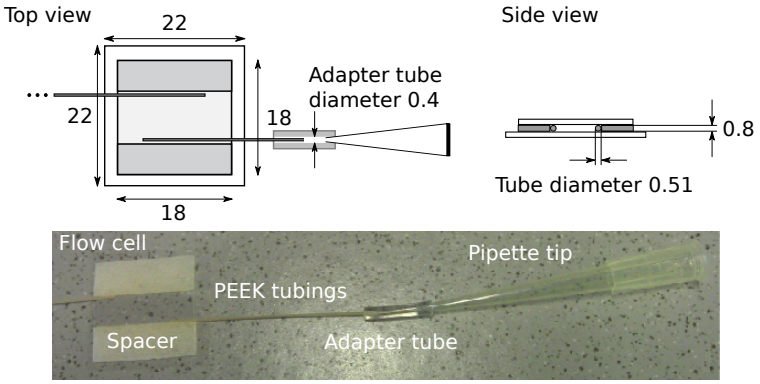

Fig. 3.1 | Sample chamber construction with PEEK tubings. The sample uses common cover slides in two different sizes (22×22 mm and 18×18 mm). The outer diameter of the tube is 0.51 mm while the inner tube diameter is 0.36 mm. The tube system is then glued together with epoxy that seals the chamber. A standard tube that is used as an adapter allows to connect to e.g. a syringe pump. Here we used for practical reasons a pipette tip. This allows to easily exchange the sample volume and prevent mayor evaporation effects. The used spacer is a combination of double sided sticky tape, glass slides and parafilm. All dimension are in millimeters.

large diameter (5–20µm) GUVs. Adding a tube system did not solve the problem initially due to an insufficient inner tube diameter. After increasing the inner diameter of the tubes, I ended up using PEEK tubings (Tub PEEK Nat, 1/32 x 0.015 ft, WO:1109924, IDEX Health & Science, USA) with an outer diameter of 510 µm and an inner diameter of 360 µm. The adapter was a standard tygon tube (inner diameter 0.4 mm, Masterflex Tygon E-lab tubuing, X100FT, Cole-Parmer Instruments LCC) held together by the pressure caused by, the diameter difference. I chose a supported lipid bilayer with traces of biotin-PE as a surface template for immobilization of GUVs. The supported-lipid-bilayer formation protocol is based on Unsay et al. [132], which is a vesicle deposition method using $CaCl_2$. The used lipids were 99.9% 1,2-distearoyl-sn-glycero-3-phosphocholine (DSPC) and 0.01% biotin-PE. DSPC has a phase transition temperature of 55 ℃. To achieve proper mixing of the lipids, the formation of the bilayer was performed at 65 ℃. After the lipid deposition, NeutrAvidin was flushed in and covered the surface. This NeutrAvidin can then be used to bind GUVs that contain biotin-PE. A detailed protocol is noted down in Appendix B.4.

3.3. Results

3.3.1. Tether pulling assay

Here, I will describe an *in vitro* assay to pull membrane tethers form immobilized vesicles. A sample chamber with an already formed supported solid lipid bilayer will be used to immobilize vesicles on the bottom surface of the sample chambers. The supported lipid bilayer contains biotin-PE incubated with NeutrAvidin for binding the biotin-pe containing GUVs. The tension of theses GUVs has been lowered by an osmotic pressure reduction using a 155 mM glucose solution instead of a 150 mM sucrose formation solution. The lower tension will lead to a hemispherical to semi-hemispherical shape after attaching to the surface [133]. The combination of these sugars has a second function: it is used to sediment the vesicles to the bottom of the chamber due to a density difference [134]. After immobilization on the surface the remaining free binding site of the surface-bound NeutrAvidin were blocked with biotin. In the next step, membrane and biotin was removed form the sample. The sample will be flipped upside down every 2 min while ≈4 ml of rinsing solution were flushed though the sample using the tube system. The applied flow was very slow. The procedure took about 30 min. By flipping the sample, we allowed unbound GUVs to move to the channel center where they were picked up by the liquid flow and carried out of the sample. From here on, the sample was mounted in the setup and microsphere were added. The next step was the search on the surface for a well-formed spherical GUV. Ideally, the surrounding of the GUV was free of any other vesicles or membrane material bound to the surface. These would increase the background signal in the florescence. Once a vesicle has been chosen, a microsphere was trapped and positioned at a distance of 10–20 µm on next to the vesicle. As a starting point in z, the vesicle was focused at the equator. For these steps, the coarse sample stage was used to navigate inside the sample. Subsequently the closed loop piezo stage was used for navigation. The fine piezo stage operates in closed loop mode, meaning we that can navigate with a readout for the absolute position relative to the starting point. This point will be called reference point and will be used to measure the force to hold a pulled membrane tube. The GUVs membrane and the microsphere were moved close together until contact was observed. To improve binding of the microsphere to the membrane, the stage was moved orthogonal to the direction of pulling. This "rolling" of the microsphere on the membrane attaches more binding sites. After attachment, the stage was moved back to the reference point and a membrane tube was formed. The displacement between the microsphere position with and without the membrane tube multiplied by the trap stiffness is the previously introduced force f_0. Depending on the initial tension of the vesicle, we observed different forces and radii. With the membrane tube formed, the heating laser can be focused on the GUV for the experiments described in this chapter or proteins can be infused

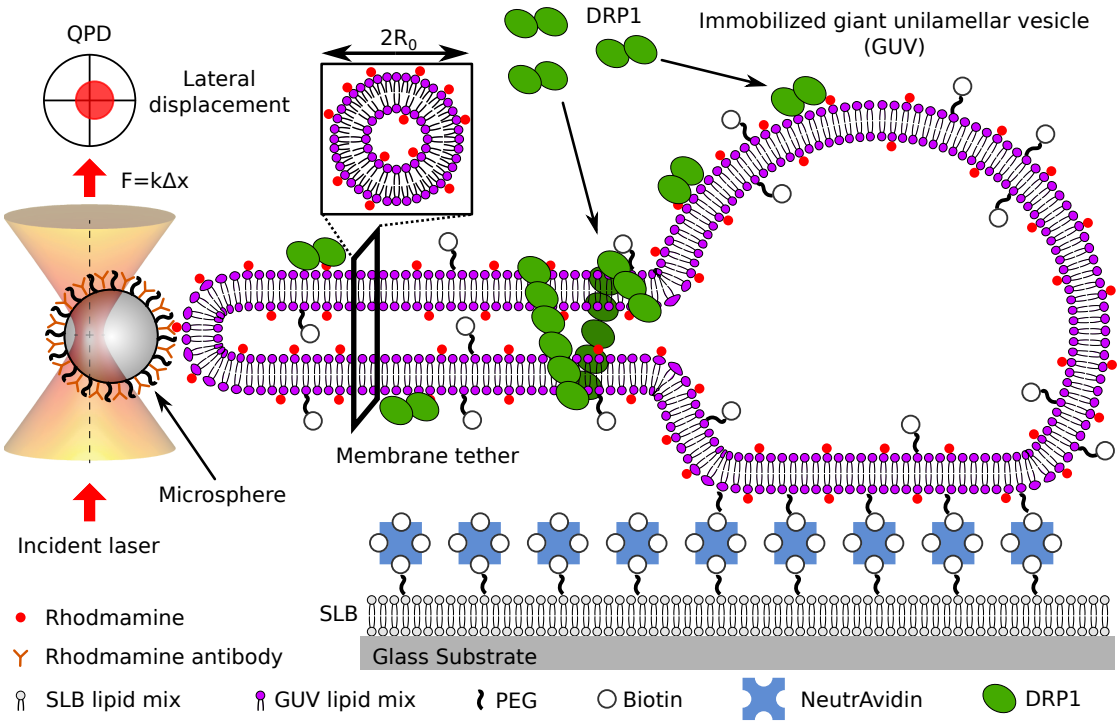

Fig. 3.2 | Schematic of the tether pulling assay, side view. A GUV is fixed on a supported lipid bilayer(SLB) by NeutrAvidin and biotin-conjugated lipids. From this immobilized vesicle, a membrane tether is pulled using optical tweezers. With a pulled membrane tube, we can study e.g. the interaction of DRP1 binding to the membrane or perform other experiments with this tether.

to observe binding or interactions with the membrane.

3.3.2. Principle of tether radius measurement

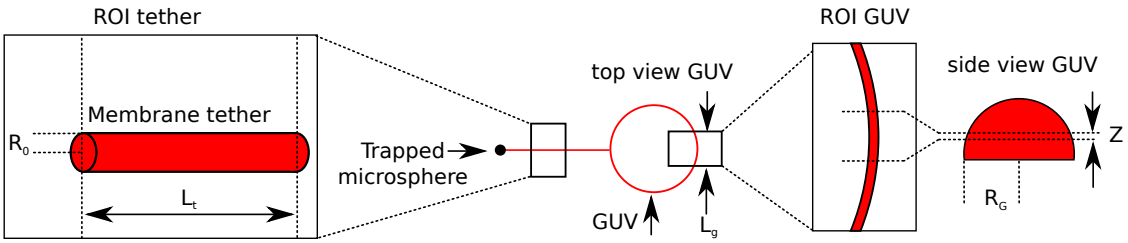

Fig. 3.3 | Principle of tether radius measurement, top view. Here I compare the intensity in both cross-sections under the assumption of constant flourophore density in both lipid formed structures.

Extracting a membrane tether radius from the comparison of fluorescent intensities has been demonstrated on supported membrane tube assays [135, 136] and in aspiration pipette optical tweezers assay [32]. The first one compared the intensity of supported lipid bilayers with the intensity of the membrane tubes only based on the geometry and flourophore density conservation. The second used a tension dependent measurement of the pulling force f_0 in combination with the micro pipette to determine the radius. We will extract a fluorescent profile from the tether and from the GUV and calculate the radius in a similar fashion. We assume both profiles share the same membrane composition. Therefore, they have the same density of fluorescent lipids. This is valid under the condition that the used lipids do not have a preference for curvature [137]. We can formulate the surface density of the membrane tube

$$\rho_{tube} = \frac{I_{tube}}{2\pi R_0 \cdot L_{tube}}, \tag{3.3.1}$$

where I_{tube} is the intensity of the tube, R_0 the radius of the tube, and L_{tube} the length of the tube. A similar approach has been taken for the surface density of the GUV

$$\rho_{GUV} = \frac{I_{GUV}}{Z \cdot L_{GUV}}, \tag{3.3.2}$$

where Z is the depth of field, I_{GUV} the intensity signal of the GUV, and Lg the length contour of the membrane section. Furthermore, we extracted a profile that had the same length of the membrane section meaning $L_{GUV} = L_{tube} = L$. Assuming $\rho_{tube} = \rho_{GUV}$ and solving for the tether radius results in

$$R_0 = \frac{I_{tether}}{I_{GUV}} \cdot \frac{1}{2\pi} \cdot Z \tag{3.3.3}$$

For the measured intensity, we used the Gaussian contribution of the fitted profiles, i.e. the integrated intensity. This procedure should be less prone to errors of a slightly defocused image plane or out of focus light compared to using the peak intensity comparison [32, 135, 136].

3.3.3. Tether radius measurement via fluorescence

Here, I demonstrate a tether radius measurement based on the fluorescent line profiles. First, the selected image in Fig. 3.4A was used to extract a line profile with a size of $60 \times 40\,\mathrm{px}^2$ from the tether and the GUV. The tether line profile was rotated straighten that the tube orients along the y-axis. The curved GUV profile was processed by the "Straighten" tool of a segmented line in FIJI[25]. The line profile of the tether was averaged along the long y axis fitted with the function

$$\Phi_t = c_t + m_t \cdot x + a_t \cdot \exp\left(\frac{-(x-\mu_t)^2}{(2\cdot\sigma_t^2)}\right) \tag{3.3.4}$$

where c_t is the offset, m_t the slope of an illumination gradient, a_t the amplitude of the Gaussian contribution, σ_t the width of the Gaussian, and μ_t the center of the Gaussian. For the GUV profile we included a step like function because of the geometry of the experiment. The attached membrane area on the bottom surface contributes out-of-focus fluorescence and leads to a step-like increase at the edge of the vesicle. The fitted function for the GUVs line profile has been extended by a hyperbolic tangent function to

$$\Phi_g = c_g + m_g \cdot x + j_g \cdot \tanh(m_j \cdot (x-\mu_g)) + a_g \cdot \exp\left(\frac{-(x-\mu_g)^2}{(2\cdot\sigma_g^2)}\right), \tag{3.3.5}$$

where m_j is the size of the step and μ_j corresponds to the slope at the jump position, which I assumed to be the same as the Gaussian center position μ_g. Due to diffraction, the overall area under the curve is considered as a signal since we assume out of focus light contributions. The absolute intensity difference was visualized by plotting only the Gaussian contributions for each line profile in Fig. 3.5D. For a diffraction limited object we would expect that the width of the Gaussians should be the same. Because the GUVs membrane is curved and there are out-of-focus contributions, we expect that the GUV profile is wider as observed. For the example given, we calculated a radius of the tube of 64.2 nm.

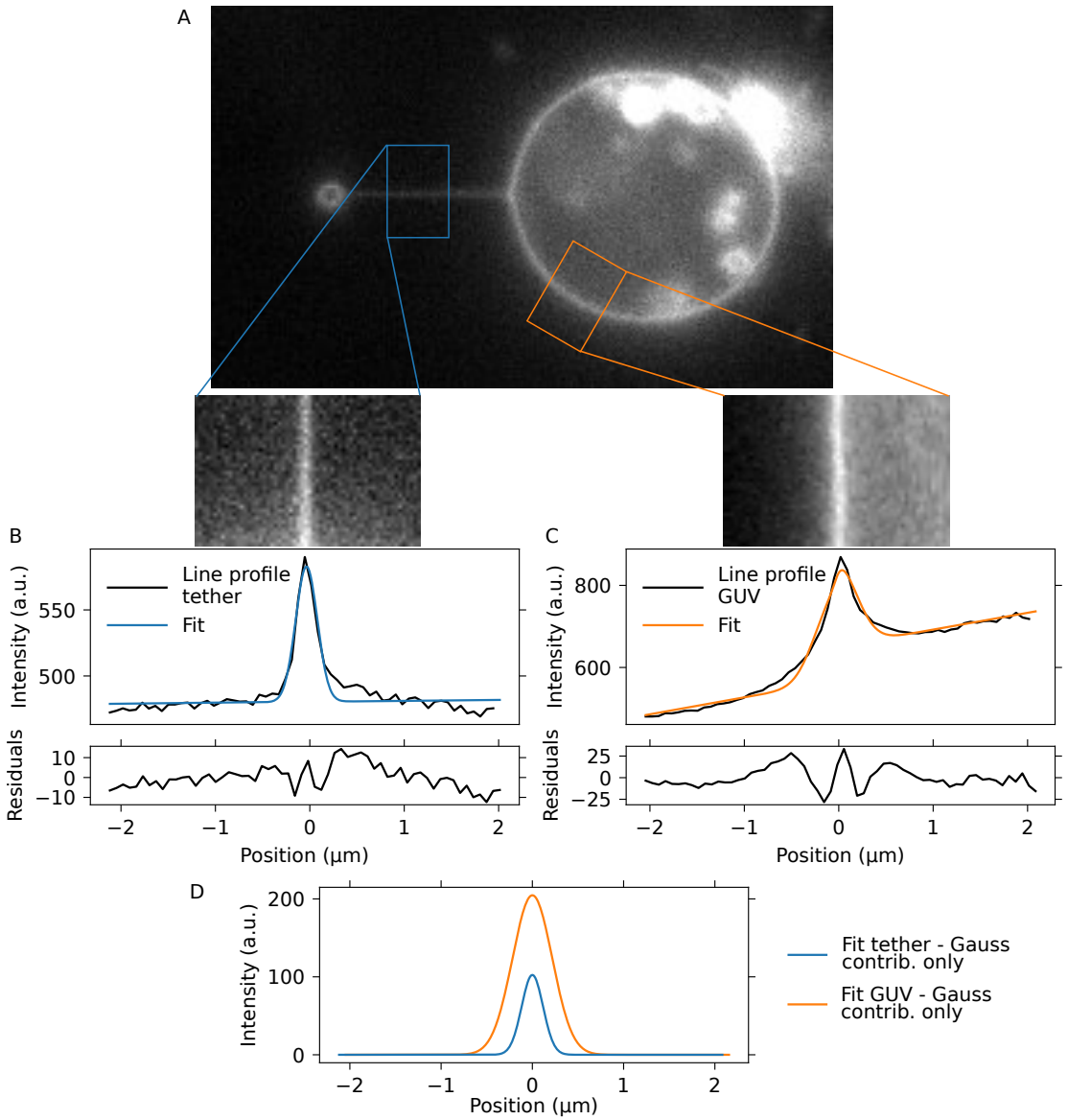

Fig. 3.4 | Membrane tether radius measurement from fluorescent a profile fit. A, Tether pulled from GUV. Regions of interest are marked. B, Extracted line profile and fit for the tether. C, The line profile was straightened in FIJI before extraction and fitting. D, Intensity relation between membrane tether and GUV membrane.

3.3.4. Tether radius change induced by heating laser based on the intensity

The membrane tether radius could be changed by a heating laser. A trapped microsphere was used to pull out a membrane tube. The heating laser was focused on the center of the GUV and, when turned on, heated the water inside the GUV. Due to thermal expansion of the water, we expected a membrane tension increase. The increase should translate into a decrease of the tube's radius(Equation (3.1.4)) and force increase (Equation (3.1.5)). Before and after the experiment, a reference picture was taken to check for irreversible membrane deformation and photobleaching that may have been induced during the experiment. The heating laser intensity was varied in the following fashion. We started with the laser turned off (0 %) followed by the highest here applied heating laser intensity of 20% for 30 seconds to equilibrate the new condition. Then, the heating laser was turned off and another laser intensity for heating was set. The time course of the experiment is illustrated in Fig. 3.5B. We started with the highest heating laser intensity because it would cause the largest decrease in membrane radius. A subsequent reduction of the heating laser intensity should show a recovery of the radius. In the opposite order, we could not distinguish an intensity decrease from bleaching. The temperature dependence of the lipid's bending rigidity will here was neglected since it appears to be constant above the phase transition temperature for dipalmitoylphosphatidylcholine (DPPC) [138]. The temperature dependence of bending rigidity for DOPC is unclear with a reported decay by Niggemann et al. [139] and a more recently reported almost constant value over a 30 ℃ range by Pan et al. [140]. As described before profiles for the tether and for the GUV were recorded. Here only the first GUV profile of this set was taken as a reference for the analysis. The temperature sensitivity of rhodamine [83, 141] suggested that the GUV profiles at higher temperatures would show a reduced measured intensity resulting in a underestimated radius R_0 compared to the reference GUV profile without the heating laser. For clarity, I plotted only the fitted line profiles form the membrane tethers at different heating laser intensities. There was a significant difference intensities in between the different heating laser powers. The reference measurement before and after the use of the heating laser overlapped. The quantification of the signal as described in the previous chapter is now visualized in Fig. 3.5. The signal is shown as a function of the heating laser intensity. We expected to have different starting membrane tensions for different GUVs. GUVs Vary in size and initial tension due to the used electro formation process. In Fig. 3.5E shows a how the radius changed. The radii typically changed by a factor of 2–5, which is similar to reported radii with other methods ranging from 10 nm–100 nm.

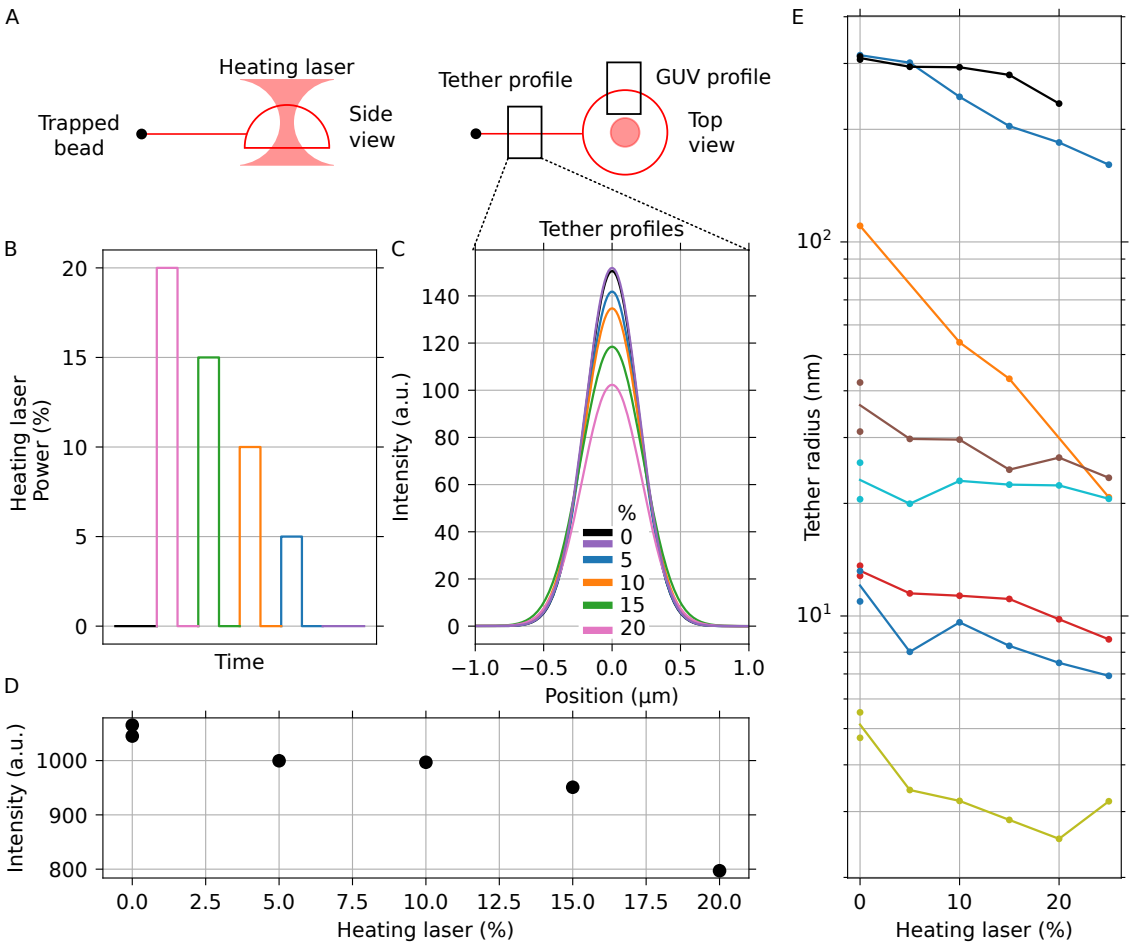

Fig. 3.5 | Tether radius change induced by the heating laser. A, Sketch of the GUV and tether profiles. B, Heating laser power for the set of line profiles as a function of time. Between each laser power change the heating laser was turned off. C, Gaussian contribution to the tether profiles. Notably, the first and the last zero heating laser power measurements were almost identical indicating reversibility. D, Integrated intensity area as a function of heating laser power. E, Tube radius as a function of heating laser power using different GUVs.

3.3.5. Tether radius change induced by heating laser based on the force signal

In this chapter, we will have a closer look at the force signal during an experiment utilizing the heating laser. A microsphere was trapped and a reference position was recorded in the force signal. Then a tether was pulled and the microsphere was back positioned to the reference position. From the relative microsphere displacement I calculated a force $f_0 \approx 6\,\mathrm{pN}$ shown in Fig. 3.6B. A change of $\Delta f_0 \approx 2\mathrm{pN}$ was observed for a heating laser power of 25%. For the lower value of 10 % heating laser power, there was no visible change in the force signal. From each force plateau,

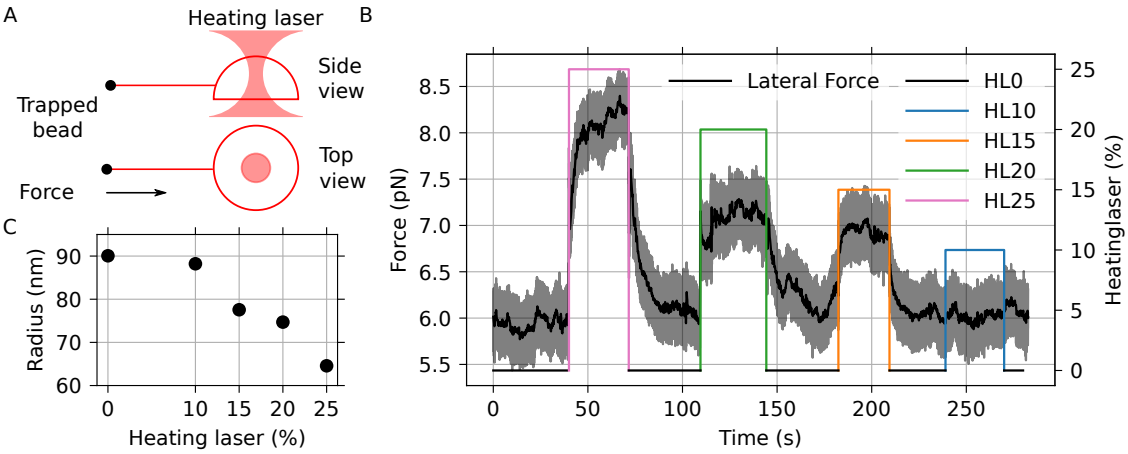

Fig. 3.6 | Tether force changes with heating laser power induced membrane tension change on the GUV. A, Sketch of the experiment with the position of the heating laser on the GUV and the direction of additional force indicated. B, Calibrated force versus time signal in an overlay with the heating laser. C, Tether radius as a function of heating laser power based on the data in B. Data is displayed at a sampling frequency of 25 kHz - grey, and filtered with a running mean to 10 Hz - black.

the last 5 second were averaged and used as a force to calculate the radius for the membrane tube, by using a bending rigidity $\kappa = 7.6 \cdot 10^{20}\,\mathrm{J}$ and equation (3.1.5). In Fig. 3.6C, we can observe a radius change from 90 nm to 65 nm.

3.3.6. Tether pulling force

The formation of membrane tethers generates a characteristic force curve [105, 120, 121, 142]. To measure such curves, we trapped a microsphere and recorded the force signal during the formation of the membrane tether (3.7). In the beginning of the experiment, the microsphere was in close contact with the membrane. In Fig. 3.7 are two plateaus visible, before the extraction and after the extraction. The bump

in the force signal was probably remnant membrane material or a microsphere that may have been trapped altering the force signal by a few pico newton. To determine the radius of a pulled tether and the GUVs membrane tension and bending rigidity, we can use the measured tether force and radius determined via the fluorescent intensity. Using Equation (3.1.5),(3.1.4) we can solve for

$$\sigma = \frac{f_0}{4\pi^2 R_0} \tag{3.3.6}$$

and

$$\kappa = \frac{R_0 \cdot f_0}{2\pi} = (4.6 \pm 1.3) \cdot 10^{-20} J, \tag{3.3.7}$$

averaged over three values (mean±SEM). The measured bending rigidity is within the spread of literature values for DOPC with $8.5 \cdot 10^{-20}$ J [143], $7.6 \cdot 10^{-20}$ J [140] and $(1.6 - 1.7 \pm 0.5) \cdot 10^{-20}$ J at 21 ℃ and $(2.4 - 6.1 \pm 1.2) \cdot 10^{-20}$ J at 23 ℃[139]. Clearly visible is an overshoot in force that has been reported to depend on the amount of contact area with a radius R_P on the microsphere. This overshoot arises of a bent GUV surface collapsing to a pulled membrane tether. Koster et al. [142] provided a numerically solved dependence of the overshoot height on the contact area size & tether radius

$$\frac{f_{over}}{f_0} = 1 + 0.5\frac{R_P}{R_0} \tag{3.3.8}$$

For the overshoot force f_{over} in Fig. 3.7A and a membrane tube radius $R_0 = 87$ nm based on the fluorescence intensity. I estimate the contact area between the microsphere and the membrane tether to have a radius of $R_P \approx 97$ nm. This radius is comparable to the tether radius and about 2 0% of the microsphere radius. For overshoot force to be equal to f_0 as happened in Fig. 3.7A, the patched area will be very small compared to the radius R_0. There the membrane tether might be pulled by only a few or even a single antibody connection.

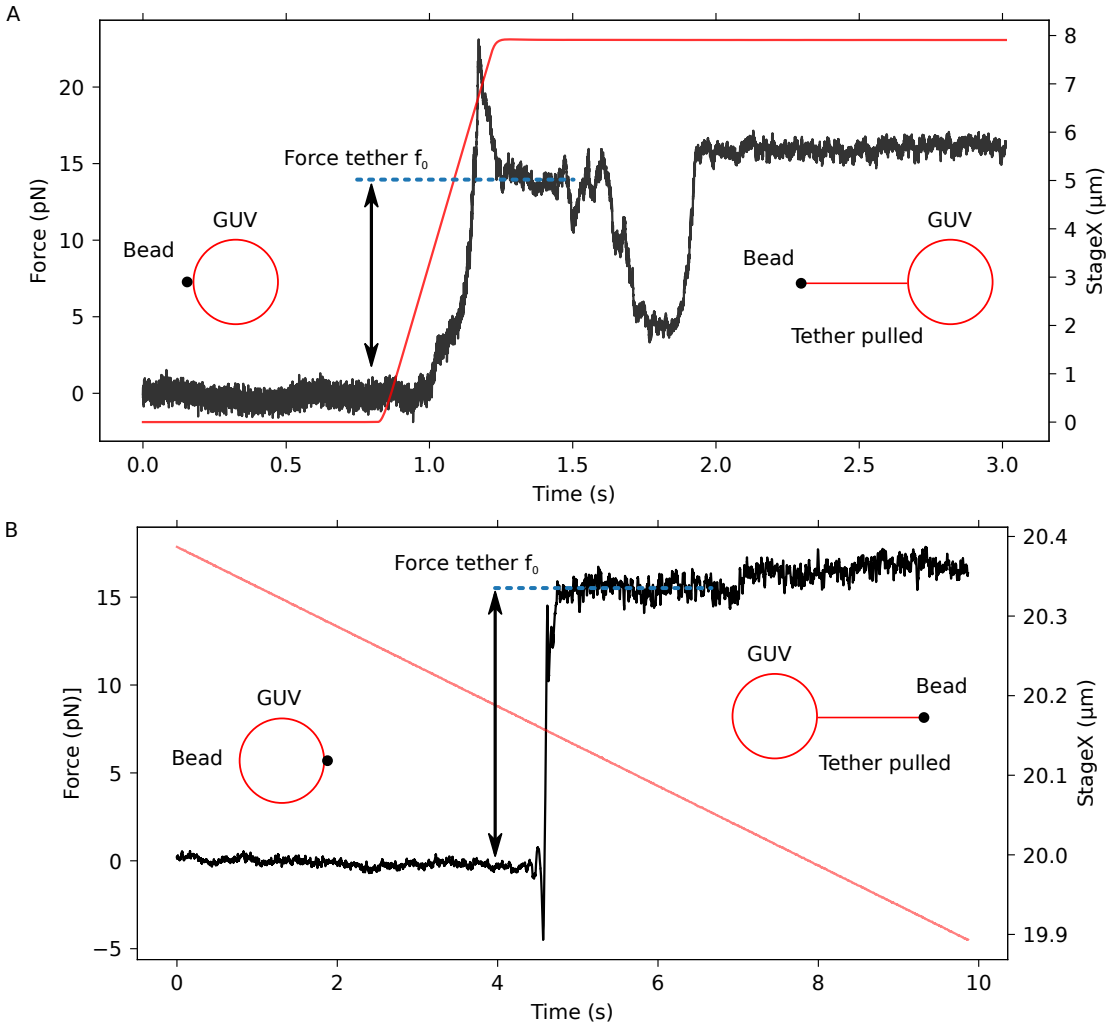

Fig. 3.7 | Membrane tether force extrusion curve. A, The left inset sketch show the microsphere pressed against the vesicle to get contact with the membrane. The right inset shows the pulled membrane tether and a new plateau force. An overshoot in force is visible with $f_{over}/f_0 = 22.5\,\text{pN}/14.5\,\text{pN} \approx 1.6$. B, Same procedure while the microsphere was position on the other side of the GUV as indicated in the inset. Here no overshoot in force is visible.

3.4. Discussion & conclusion

I demonstrated a novel method to pull a membrane tether from a GUV immobilized on a supported lipid bilayer. The tether can be pulled close to a sample surface and the radius can be changed by the use of a heating laser. This technique has in principle the potential to pull membrane tether in the evanescent field of a TIRF microscope eventually providing single-molecule sensitivity. Unfortunately, my efforts to pull tethers in the evanescent field did not succeed and therefore not shown here. Most of the membrane tethers stuck on the surface while I was pulling the membrane tubes or adhered to the surface over time. The adherence could arise from small defects in the supported lipid bilayers. Small defects in surface coating can occur for PEGylation as well and was intentionally used to fix supported membrane tubes [135, 136] on surfaces. Using the supported lipid bilayers was still a very good alternative to the previously used hydrophobic absorption based surface coatings [68] that I tested. Membrane tethers might have also bound to insufficiently blocked NeutrAvidin or due to the regular biochemical turnover of the biotin-NeutrAvidin interactions.
The use of a heating laser has the disadvantage of convection. Even tough the convection can be useful for alignment of the heating laser, it can transport membrane debris and microspheres to the optical trap. If these particles are trapped, which occurred often, force measurements are disturbed as seen in Fig. 3.7. Depending on the laser power of the optical tweezers, we can also observe convection for the trapping laser itself starting to become relevant around 50 % laser power. I chose heatings laser power in the experiments below 25 %, which corresponds to a local temperature increase of $\approx 8.75\,^{\circ}\mathrm{C}$. The convection close to the bottom of the surface is dragging microspheres and membrane remains into the field of view or even into the optical trap as just discussed. For the fluorescence measurement this effect can increase the background locally. This could lead to an over or underestimation of the intensity-based radius measurement. The induced convection turned out to be useful to attract microsphere. The experiments were performed with a low concentration of microspheres, roughly one per field of view. Convection allows to find a microsphere for pulling a membrane tether in a short amount of time. The radius change, we can apply depends on the starting conditions, i.e. the membrane tension of the GUV, which can be adjusted through the osmotic pressure. If we increase the surrounding sugar concentration compared to the GUVs inside it should lower the tension and provide larger tether starting radii. We could in principle follow a similar approach by using an intermediate heating laser power as a starting radius. I note that with this method, we can only reduce the membrane tether radius. In the micro aspiration pipette method one typically adjust the starting tension towards a intermediate radius while maintaining a range for larger and smaller radii. The established method will be further used in the next chapter to study the interaction of a membrane protein with a pulled nano tube.

4. Dynamin related protein 1 (DRP1) interactions with microtubules & membrane tethers

4.1. Introduction

Membrane associated proteins (MAPs) are involved in a variety of biological processes such as transport of cargo, signal transduction, catalysis of reactions, membrane shaping and stabilization. It has been estimated that over 60% of the possible drug targets are MAPs [144, 145]. Therefore MAPs are an interesting field to study with a huge potential in drug development. Synthetic membrane systems have been developed to study MAPs in an isolated environment with a controlled lipid composition and depending of the chosen system a controlled curvature. The variety of these developed *in vitro* systems can range from small- (25–50 nm), over large- (100–400 nm), to giant unilamellar vesicles (GUVs) $< 100\,\mu m$ and jetted vesicles ($< 200\,\mu m$) up to whole sample surfaces covered with a supported lipid bilayers [146]. I will give a brief introduction to the study of membrane proteins in *in vitro* by using a supported lipid bilayers or GUVs and dynamin related protein 1 (DRP1). These model system are used in this thesis in a novel combination to investigate DRP1.

GUVs provide a large, free-standing and freely accessible membrane for proteins of many kinds. It has been shown that membrane proteins can be reconstituted on the inner leaflet[4, 109], outer leaflet [32, 34] or inside the membrane [147]. It is e.g. possible to study the tension sensitive, curvature-coupled voltage-gated potassium channel (KvAP)[147]. In these experiments, a GUV was fixed with a micro aspiration pipette and observed using fluorescence. For imaging, the bottom of a large GUV had been chosen to provide a certain area to track diffusing KvAP and a non-tension sensitive aquaporin 0 (AQP0) as a reverence. Another example is the study of shape transitions of GUVs depending on the enclosed polymers, proteins or DNA [148]. The spherical shape and accessibility of the GUV system makes it difficult to be used e.g. in a TIRF microscope, which would increase the sensitivity in fluorescence.

Supported lipid bilayers on the other hand are reconstituted membranes mostly on flat glass substrates. Thus the membrane is located at the optimal position for a

TIRF microscope. Supported bilayers can be also used to study the interaction of proteins with lipids or incorporated proteins [149]. One can obtain e.g. information about the stoichiometry [150] or diffusion coefficients [151, 152] by single particle tracking (SPT) / fluorescence recovery after photobleaching (FRAP) experiments. A disadvantage on glass surfaces is that the surface can lead to two population in diffusion coefficients of lipids or membrane proteins. One population is due to molecules facing the glass surface and the other due to the ones that face the medium. In case of transmembrane proteins, it can even result in immobile proteins [153].
I will use supported lipid bilayers and GUVs in combination to study dynamin-related protein 1 (DRP1). DRP1 is a 80 kDa dynamin like GTPase mediating mitochondrial and peroxisomal division. Mitochondria are termed as the powerhouse of the cell, because they provide cellular ATP and also host other metabolic reactions [154, 155]. They are a dynamic tubular network that is continuously reshaped by fusion and fission events. The regulation of this fission and fusion of mitochondria is critical for maintenance of this system [156–158]. Mitochondrial dynamics or malfunction of it seem to be linked to neurodegenerative diseases such as Parkinson's, Alzheimer's or Huntington's disease[159–161]. DRP1 is required for mitochondrial division in eukaryotic cells. The recruitment of DRP1 from the cytoplasm to the outer mitochrondrial membrane can be regulated by mitochondrial fission factor or mitochondrial dynamic proteins (MiD49, MiD51) [162–168]. The affinity between DRP1 and its adapters seems to be regulated by the different isoforms of DRP1 [169, 170]. DRP1 has a four domain structure, GTPase domain, a bundle-signaling element, a stalk, and B insert[171–173]. DRP1 oligomerizes into filaments around mitochondria [168]. The GTPase domain faces towards the outside of the filament and the B-insert is facing towards the membrane (Fig. 4.1). DRP1 contains a variable domain (VD-domain) that is unstructured. Its function is still debated but it was possible to correlate with negatively charged membrane binding [174, 175]. DRP1 is further involved in the cell cycle while it colocalizes with microtubules bundles of the midbody during cytokinesis [176]. Since the E-hook (the last 10 and 18 C-terminal residues of a- and b-tubulin) of a microtubule is negatively charged [177] and unstructured, interactions could take place similar to binding of DRP1 towards negatively charged membranes. In contrast to the classical dynamins, DRP1 lacks a pleckstrin homology domain (PH-domain) that is required for membrane binding [136, 178] and has been associated with curvature sensing [179, 180]. The number of DRP1 molecules contributing to the formation of a functional fission complex on mitochondria has been approximated to ≈ 100, in *in vivo* experiments [181]. While in *in vivo* experiments isolated fission capability of DRP1 was unclear, it has recently been shown that DRP1 (isoform 3) can sever *in vitro* as well [182]. In contrast severing for isoform 1 of DRP1 has not been observed, yet [39]. Here we have found that DRP1 isoform 2 binds and bundles around three microtubules *in vitro*. Furthermore, it was possible to show

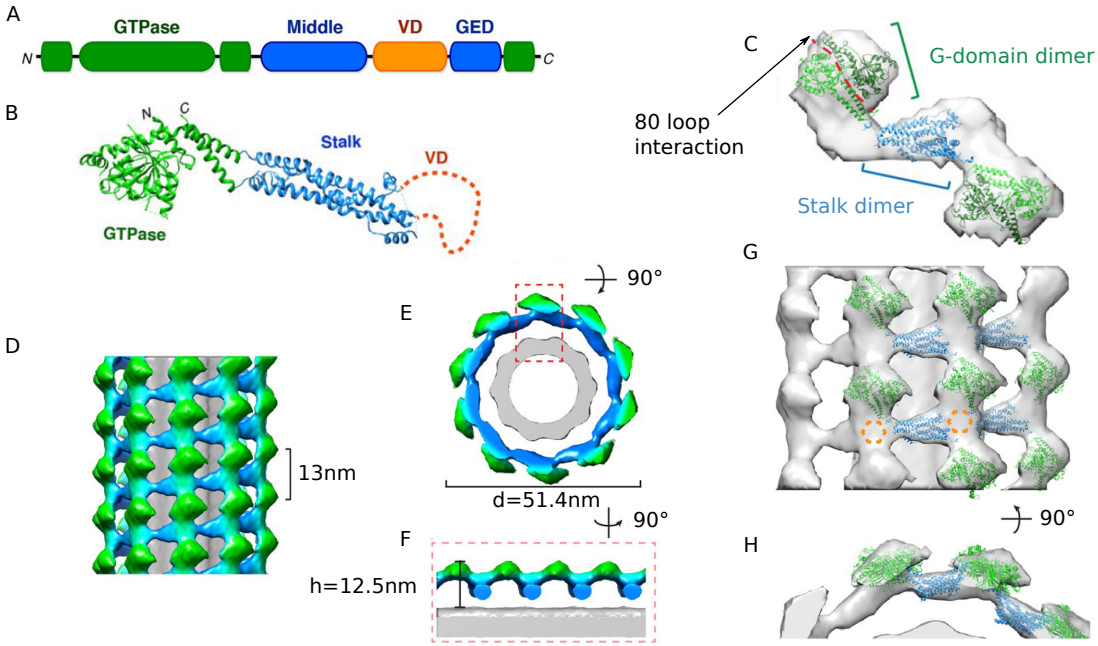

Fig. 4.1 | Structural information about DRP1 based on cryo-EM studies. A, Primary structure of DRP1 with highlighted domains. B, Tertiary structure of DRP1 (PDB ID 4BEJ). C, Fitted structure of a DRP1 dimer is shown. D–F, 3D reconstruction of DRP1 while present on a membrane tether. G, Side view a fitted structure and H, rotated view of the same structure. Source: Adapted from Fig. 1 in Francy et al. [175], with permission under CC BY 4.0 international license.

that DRP1 isoform 1 is binding and severing membrane tethers. The here used low concentration of DRP1 allowed me to track single oligomers with the size of a few hundred monomers and larger.

4.2. Results

4.2.1. DRP1 and microtubule co-localization

Based on the interactions of DRP1 with microtubules during cytokinesis by Strack et al. [176], we tested the binding behavior in an *in vitro* assay with purified components. To this end, we prepared microtubules. Porcine tubulin was polymerized into microtubules in PEM buffer with 10 % rhodamine-labeled tubulin. Microtubules were stabilized 10 µM with taxol [53]. The microtubules were incubated with 1 mM GTP, 50 nM DRP1, and 10 µM taxol in GTPase buffer. For imaging, the mixture was diluted 10 × and an oxygen scavenger—glucose oxidase and catalase—the GODCAT system [183] was added. In the presence of GTP, isolated microtubules were covered with DRP1 as shown in Fig. 4.2A. The intensity of a DRP1 covered microtubules and the intensity of a single microtubule next to it was analyzed in the same fashion as described for membrane tether intensity profiles in Chapter 3.3.3. We compared the integrated area of the Gaussian contribution of the line profile. By dividing the bundle signal by the single microtubule singal, we get the number of microtubules per bundle plotted in Fig. 4.2B. The histogram was fitted with two Gaussian distributions where the main peak result in 3.14±0.07 (standard error of the fit) micro tubules per bundle and a second peak at 6.3±0.6 microtubules per bundle. Control measurements have been performed with a mutant S590E, in which serine (neutral net charge) has been exchanged to a glutamic acid (negative net charge) at the position in the VD-domain. For an electrostatic interaction of a positive charged VD-domain and a negatively charged E-hook of the microtubules, this mutation should abolish binding, which we observed in the presence of GTP. In the presence of GDP, for DRP1 isoform 2, large oligomers of DRP1 have been formed that only partially correlate with microtubules. GTPase activity assays have been performed in collaboration with Begoña Ugarte-Uribe. The GTPase activity of Drp1 was assayed using a colorimetric assay as described in Ugarte-Uribe et al. [131]. Briefly, 0.5 µM of Drp1 was incubated at 37 °C in 20 mM HEPES buffer (pH 7.4), 150 mM KCl, 1 mM $MgCl_2$, and 10 µM taxol in the absence or presence of microtubule bundles (0.5 µM). Reactions were stopped at the indicated times by diluting 20 µl of the sample in 100 mM EDTA (final concentration) in a plate. Samples were then incubated with 150 µl of malachite green stock solution (1 mM malachite green and 10 mM ammonium molybdate in 1 N HCl), and the absorbance at 620 nm was determined using Thermo Scientific Multiskan GO microplate reader (Thermo Scientific, Darmstadt, Germany). The amount of released phosphate during the hydrolysis of GTP to GDP and inorganic phosphate (Pi) has been calibrated with a known standard concentration. The combination of DRP1 and microtubules showed the highest conversion of Pi. The S590E mutant with and without microtubules showed no significant difference in the presence or absence of microtubules. The here presented results show, to my knowledge for the

first time, *in vitro* DRP1-microtubule interactions in form of microtubule bundling and microtubule stimulated GTPase activity of DRP1. These interactions might be due to electrostatic interactions in analogy to DRP1-membrane interactions. Microtubule-DRP1 bundles may act as a reservoir for DRP1 molecules.

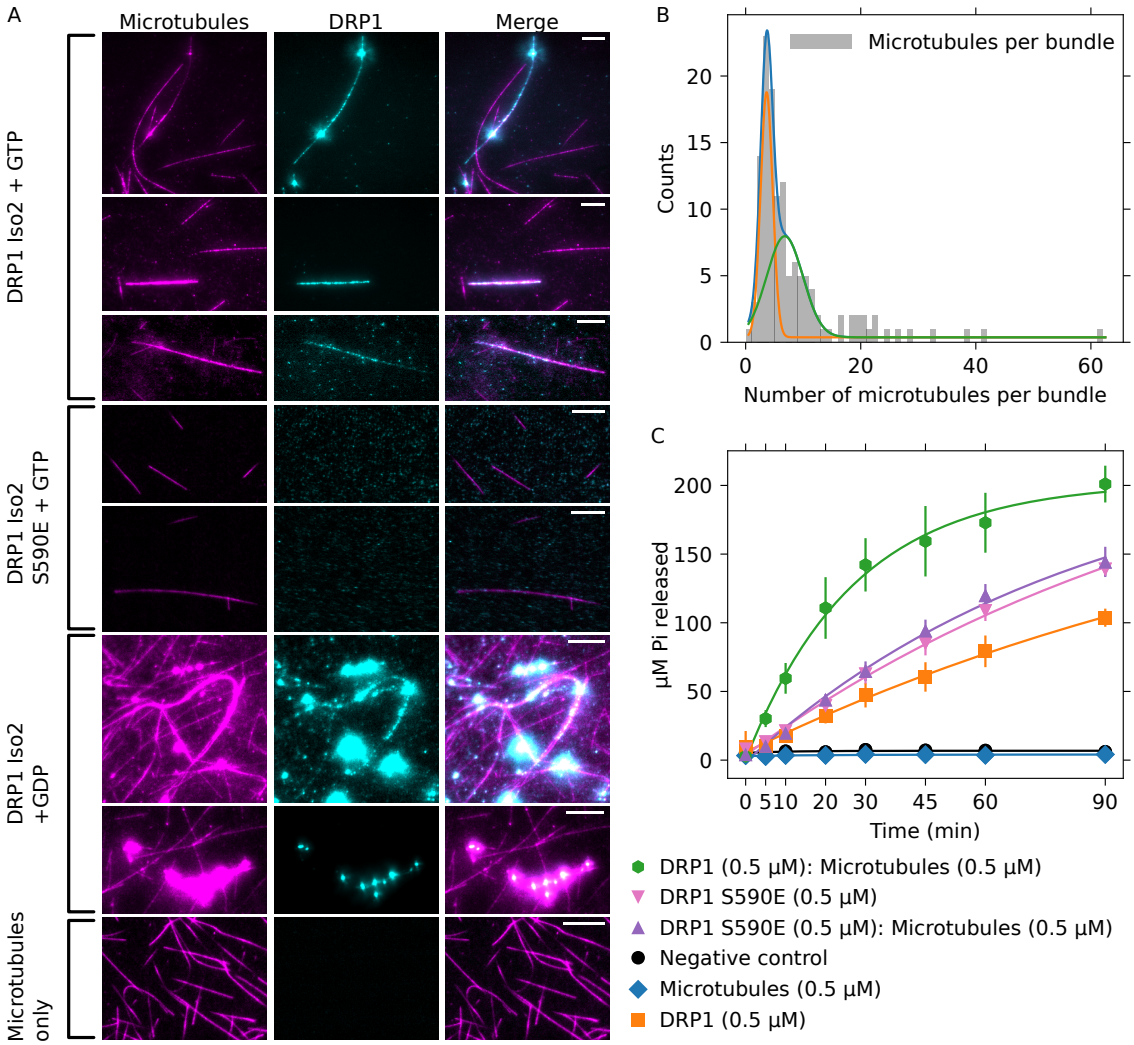

Fig. 4.2 | DRP1 bundles microtubules. A, Fluorescent images of DPR1 and GTP, DRP1 S590E mutant and GTP, DRP1 and GDP, and microtubules as a negative control. Scalebar: 5 µm. B, Histogram for the number of microtubules per bundles, 130 data points. Here the intensity of a a single microtubule was measured and compared to the intensity of a bundle. C, GTPase activity of DRP1 was measured by a colorimetric assay.

4.2.2. Fluorescent intensity calibration via photo bleaching

The amplitude of the fluorescence signal can be used to estimate the stoichiometry of labelled molecules [184, 185]. To estimate the number of labeled DRP1 molecules that interacting with membrane tubes, I measured bleaching steps and determined the mean intensity of a single flourophore. The experiment was performed in the following way. I prepared a solution of DRP1 with a concentration of 10 pM and 1 mM GTP in GTPase buffer. As an oxygen scavenger I used ascorbic acid [130] and the commonly used glucose oxidase and catalase—the GODCAT system [183]. The sample was prepared as mentioned in Protocol B.2. On a clean glass surface the protein is absorbed and bleached over time in steps after flourophore excitation using a tilted illumination. Form the recorded videos, I extracted a 5×5 pixel ROI and analyzed these with Fiji. Each ROI was processed using the z-Project function to generate a time trace. In Fig. 4.3A, a typical time trace is shown for an oligomere. To analyze the bleaching steps, I used a python package [186] that allows to set a variety of parameters for step size and dwell time analysis. With this package it is possible to detect steps in a time signal. I used 34 DRP1 time traces and plotted a histogram of the step size in Fig. 4.3B. The shown histogram has two maxima one of around -10 counts and the other at $+10$ counts. Positive counts are landing events and negative counts are bleaching events. Blinking may contribute to both. The higher count on the negative side is due to fields of view where proteins were sticking on the surface before recording. Therefore, more steps were detected on the bleaching side. To determine the average intensity for one flourophore I fitted a Gaussian to the orange marked portion of the histogram. The fit resulted in a mean intensity value of $I_{mean} = -10.4 \pm 0.6$ SEM per flourophore at a laser power of 50 mW in the tilted illumination mode with 100 ms exposure. To apply this value to different excitation laser intensities, we assume that the intensity of a flourophore scales linearly with the laser power. I calculated a threshold for the lowest number of molecules that we can detect with a signal to noise ratio of 2 at the later used laser power for of 1 mW. Using the standard deviation of the noise level at 1 mW excitation power and 100 ms exposure time of 7 counts, I estimated $N_{min} = \text{SNR} \cdot \text{Noise}/(I_{mean}/50) = 2 \cdot 7/(10.4/50) = 70$ fluorophores. With a labeling ratio of 1–2 fluorophores per DRP1 molecule, 35–70 DRP1 molecules need to be in a cluster to be detected with 1 mW excitation power.

4.2.3. DRP1 oligomers bind to diffuse on membrane tethers

In this chapter, I will describe the results from tracking diffusing DRP1 oligomere on a pulled membrane tube. First a microsphere was trapped and a membrane tube was pulled as previously described. To calculate the starting diameter of the membrane tube, I took a reference pictures for the fluorescence analysis. Subsequently, DRP1 was infused at a final concentration of 10 nM with 1 mM GTP.

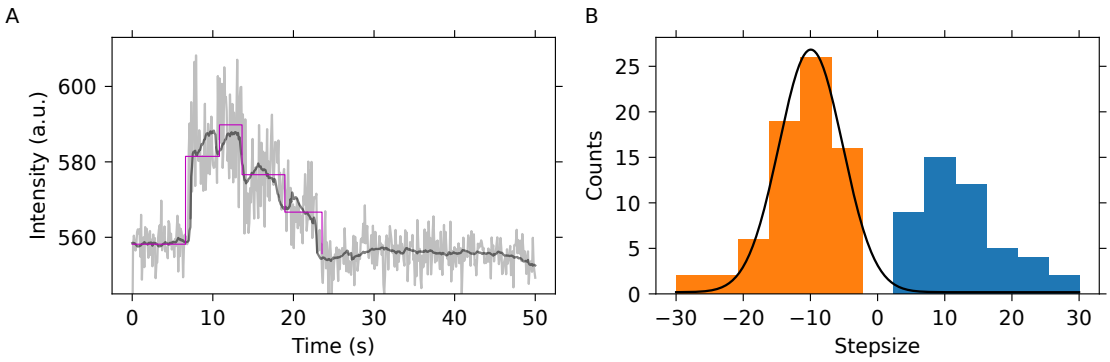

Fig. 4.3 | Bleaching steps for fluorophore intensity calibration. A, Exemplary trace for an oligomer of approximately 3 fluorophores bleaching over time. B, Histogram of step size found by the stepfinder. The negative values have been fitted with a Gaussian.

I used trackpy [187], a python package, for particle tracking and a mean square displacement analysis. From this package, a table with the position, spot characteristics and the frame number is generated. Fig. 4.4A shows the spatial projection of all tracked particles. In the next step, I used a linking procedure to link detected spots to particle traces. I applied an additional filter for the position in the y coordinate to exclude molecules beyond (4.4B). To visualize the tracked traces on the membrane tether, I plotted the tracked coordinates and a kymograph in an overlay (4.4C). Many detected DRP1oligomers landed and diffused on the tethers. Some dissociated again. The mean time that clusters interacted with the tether was xyz seconds. From the tracked position, the mean square displacements can be calculated. I used a one-dimensional diffusion relation because this had been used for KvAP diffusion in a membrane tether [188],

$$\mathrm{MSD} = 2Dt + c \tag{4.2.1}$$

where t is the lag time, D the diffusion coefficient, and c an offset that can be used to account for localization precision [189]. The extracted diffusion coefficient for every DRP1 trace was plotted into a histogram (Fig. 4.4D). Diffusion coefficients varied from about 0.003 to 0.1 $\mu m^2/s$. For comparison, the diffusion coefficient of a single cardiolipin is $\approx 5\,\mu m^2/s$ [190] and for microdomains $0.001\,\mu m^2/s$ [191, 192] depending on the size. To test the lower limit of the tracking procedure I tracked a few DRP1 oligomers that were stuck on the surface. I determined a diffusion coefficient of $D_{fixed} = 5.5 \cdot 10^{-5} \pm 0.6 \cdot 10^{-5}\,\mu m^2/s$. Thus, all measured DRP1 diffusion coefficients were significantly larger than the tracking precision.

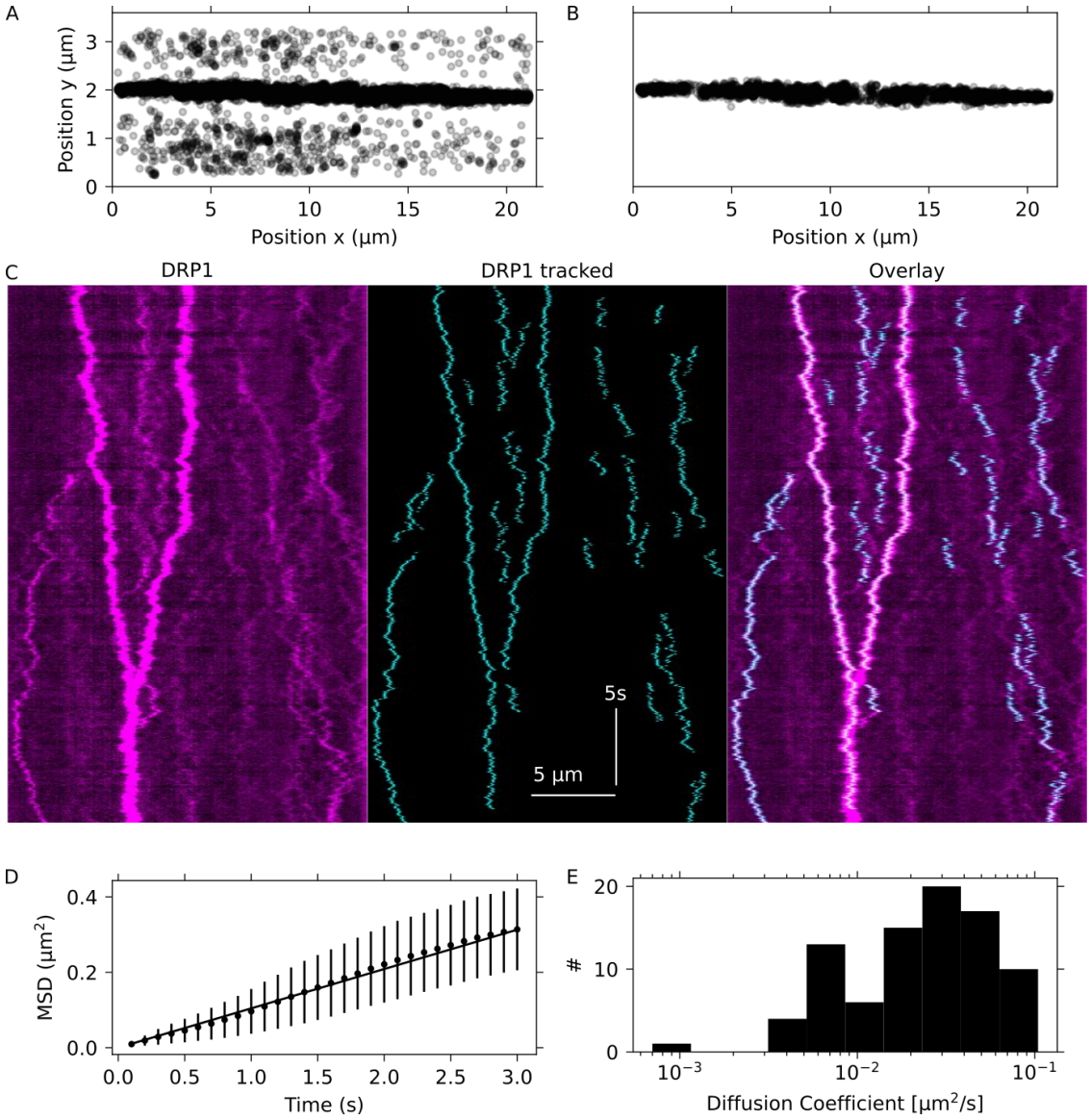

Fig. 4.4 | Single particle tracking of DRP1 oligomers on a membrane tube. A, All tracked DRP1 oligomers without filter. The threshold for the minimum intensity was set in such a way that DRP1 in solution was also detected. B, A position filter, threshold for visibility in the video and a maximum distance filter was applied to the data from A. C, Kymograph made from the fluorescent image series and the tracked coordinates of DRP1. D, MSD of one trace with a diffusion coefficient of $D = 0.0521 \pm 0.0012\,\mu m/s^2$. E, Histogram of 87 tracked DRP1 oligomers from all experiment performed.

4.2.4. Oligomer number estimation via fluorescent intensity

Because the diffusion coefficients varied by about two orders of magnitude, we wondered how the diffusion coefficients correlated with the oligomer size. Therefore, we measured DRP1 oligomere size based on the fluorescent intensity. I performed an intensity measurement at the beginning of each tracked trace and calculated the oligomeric state based on the calibration in Sect. 4.2.2. The diffusion coefficients as a function of the number of DRP1 molecules is shown in Fig. 4.5 with the additional color-encoded information of the membrane tube radius the oligomers are bound to. Diffusion along membrane tethers has been described based on the Saffman-Delbruck Theory [193], by Daniels and Turner [194]. In the limit of $R_0/\mathrm{a} \gg 1$, they obtained from the derived diffusion coefficient

$$D = \frac{k_B T}{4\pi\eta} \sum_{m=1}^{\infty} \frac{1}{m} \exp(-ma/R_0) \cdot \cos(ma/R_0) \tag{4.2.2}$$

the approximation

$$D = \frac{k_B T}{4\pi\eta} \ln\left(\frac{r}{a}\right) \tag{4.2.3}$$

where k_B is the Boltzman constant, T the temperature, η the viscosity of the membrane, R_0 the radius of the tether and a the protein size. Since it is unknown how exactly DRP1 is binding towards the membrane I made a few assumptions based on the current literature. Starting with the size of DRP1 Domain that interacts with lipids. The lipid (cardiolipin) interacting domain is proposed be the VD-domain variable domain of DRP1 is binding towards the membrane. This assumption is based on structural Cryo-EM studies that could show for a depletion mutant of this domain, no binding to membrane tethers was observed [175]. This domain is unstructured, located at residues 517—639 [174]. With an average mass per amino acid of 118.9 g mol^{-1} [195] I estimate the molecular mass of the VD-domain to m_{VD} ≈14.5 kDa based on the number of residues [174]. The lipid interacting domain is proposed to be the VD-domain [175]. For a quantitative comparison of the measured DPR1 diffusion coefficients with the diffusion model, we approximate the VD-domain with a sphere that is embedded in the membrane. The density of globular protein is on average ρ_{Prot} =1.38·10^3 kg·m^{-3} [196]. The volume of one VD-domain is

$$V_{\mathrm{VD}} = \frac{m_{VD}}{\rho_{Prot}} = 1.61 \cdot 10^{-26}\,\mathrm{m}^3 \tag{4.2.4}$$

corresponds to a sphere with radius

$$r_{\mathrm{VD}} = \sqrt[3]{\frac{3V}{4\pi}} = 1.56\,\mathrm{nm}. \tag{4.2.5}$$

We assume that the protein radius a in Eq. (4.2.2) depends on the square root of the number N of DRP1 moelcules according to $a = r_{\mathrm{VD}}\sqrt{N}$. Additionally for the diffusion model we approximated, the viscosity of the membrane with $\eta = 6.5 \cdot 10^{-10}\,\mathrm{Jm}^{-2}$ [188], which corresponds to a 90 % PC mixture. The used MLL-mix is more complex and the viscosity is not available, but contains 48 % PC which as the main component. Experiments have been performed at 28.2 °C. With these assumptions, we can compare the measured diffusion coefficients (from SPT) and the oligomeric state (from fluorescence) with the model (Eq.(4.2.2), Eq.(4.2.3) in Fig. 4.5). Since the diffusion coefficient is depends on the radius of the tether and the protein size diffusing, I plotted the dependency with a parametrized tether radius. The increment in radius is 25 nm and the color of the theoretical curves and data points correspond to measured and parametrized radius, respectively. Agreement between the model and theory is poor. Also, the assumption of the model that $R_0/\mathrm{a} \gg 1$ R_0 does not hold since very small oligomers diffusion coefficients imply that $R_0 \approx a$. Thus a different model is needed to describe the oligomer diffusion.

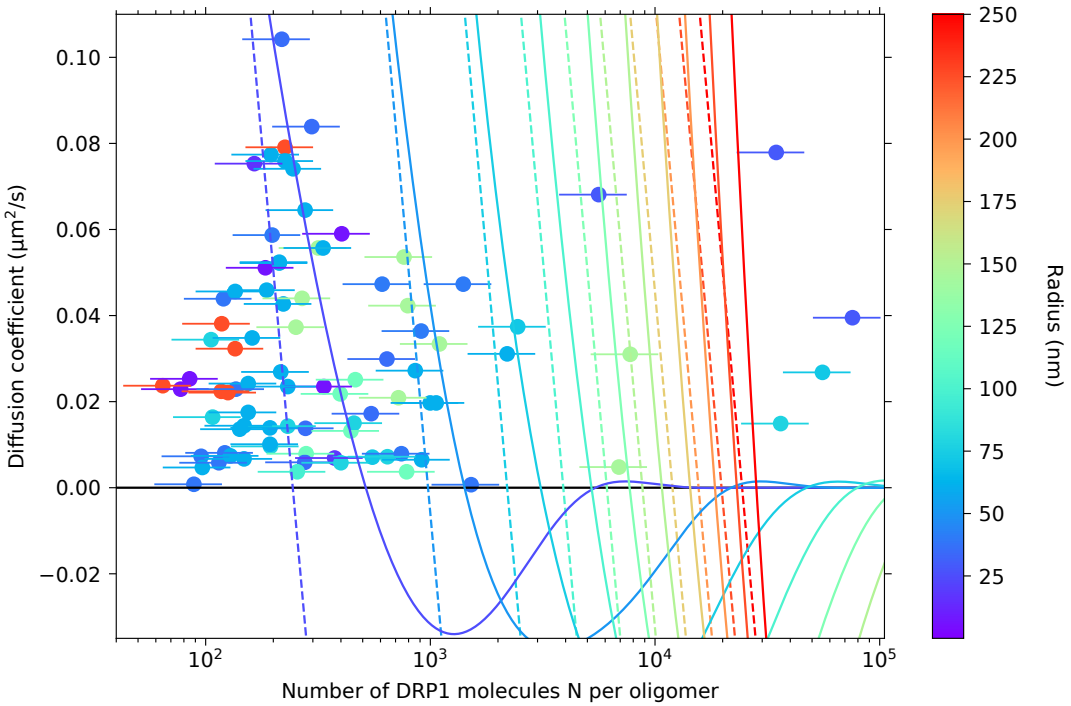

Fig. 4.5 | Comparison of diffusion coefficients and oligomer size with the existing model for diffusion in membrane tethers. Each data point is encoded with a color that represents the radius of the membrane tether they bound to. The error bar is a systematic error calculated from the labeling stoichiometry of 1–2 fluorophores per DRP1. From Eq.(4.2.2), the diffusion coefficient with m_{max} =2000 solid line is shown. The approximation from Eq.(4.2.3) is plotted as dashed lines.

4.2.5. Oligomer size estimation

Does the diffusion coefficient depend on the size of the DRP1 polymer? For a monomer they measured a size of about 9 nm×13 nm on cardiolipin containing tubes. One can calculate the theoretically covered membrane tube length by comparing the membrane tube surface area with the area that one DPR1 dimer can cover. Based on the existing literature, I derived a simplistic view to on the surface coverage. The dimensions for a DRP1 homolog, DNM1, are about 9 nm×23 nm for a dimer [172]. Additional structural information of DRP1 are provided by Francy et al. [175].This size corresponds to an area of about $A_{\mathrm{DRP1}} = 117\,\mathrm{nm}^2$ per DRP1. Assuming a helical polymer structure [175], results in a length of the DRP1 around the membrane tube of

$$L_{tube} = \frac{N A_{DRP1}}{2\pi(R_{tube} + h)} \tag{4.2.6}$$

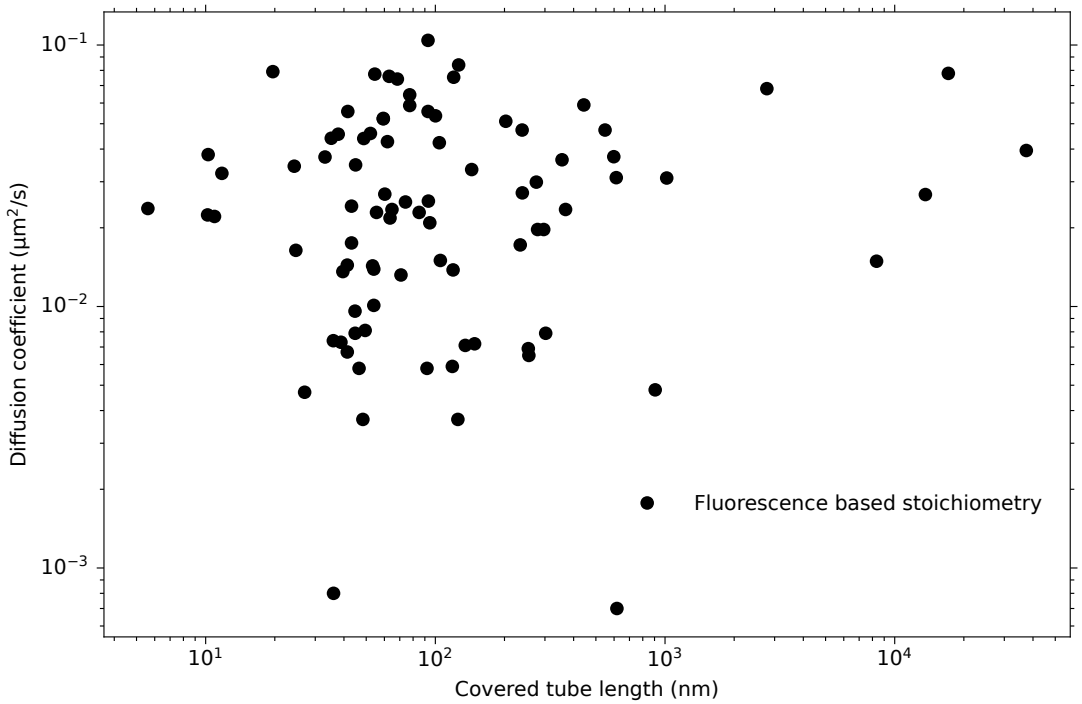

Fig. 4.6 | Comparison of the oligomeric state measurements with respect to the theoretical covered tether length. Diffusion coefficient as a function of expected DRP1 oligomer membrane tether coverage.

where N is the number of monomers based on the fluorescent intensity, h the space between the GTPase domain and the membrane [175], R_0 the radius of the membrane tether. The diffusion coefficient plotted versus this length did not show any obvious correlation (Fig. 4.6). Also the calculated length was sometimes longer than the size of the observed, diffraction limited DRP1 oligomers. This observation suggests that, in particular for large oligomers, DRP1 polymers did not fully wrap around the membrane tubes. Thus, in the following, we estimate, based on the diffusion coefficients, how many DRP1 molecules per oligomer did form contacts with the membrane.

4.2.6. Tether-bound fraction of DRP1 based on the diffusion coefficient

The calculated covered tether length based on the fluorescence from the last chapter led us to question of how many bound DRP1 molecules contribute to the diffusion coefficients. Here I will suggest a simplistic model based on the binding behavior of DRP1 and its VD-domain interacting with cardiolipin. Since cardiolipin has up to two negative charges [197] and the VD-domain has been proposed to interact directly with negatively charged lipids-[131, 174, 198], we investigated the properties of the VD-domain in Fig. 4.7A. The sequence of the VD-domain residues (wild type [199]) correspond to the points in the plot. Based on the local net charge, per amino acid one can identify six positions that have at least two positive charges close to each other for potential binding of cardiolipin. Additionally, the hydrophobicity is shown. Hydrophilic and positive charges coincide and potential areas that can insert into the membrane exist around residue 20, 60, and 75. Based on the diffusion coefficient of cardiolipin ($\approx 5\,\mu m^2/s$-[190]), we calculated the number of lipids that were bound to diffusing DRP1 oligomer with

$$N_{\mathrm{cl}} = \frac{D_{\mathrm{cl}}}{D}. \tag{4.2.7}$$

We assumed that the drag coefficient scales linearly with the number of bound molecules. In Fig. 4.7A and B, we show the number of bound cardiolipin as a function of DRP1 measured by florescence. The solid line indicates a 1:1 ratio and we choose to plot the data both on a linear and logarithmic scale. The grey area indicates data points that have 0.66–5 cardiolipin molecules bound to one DRP1 molecule.

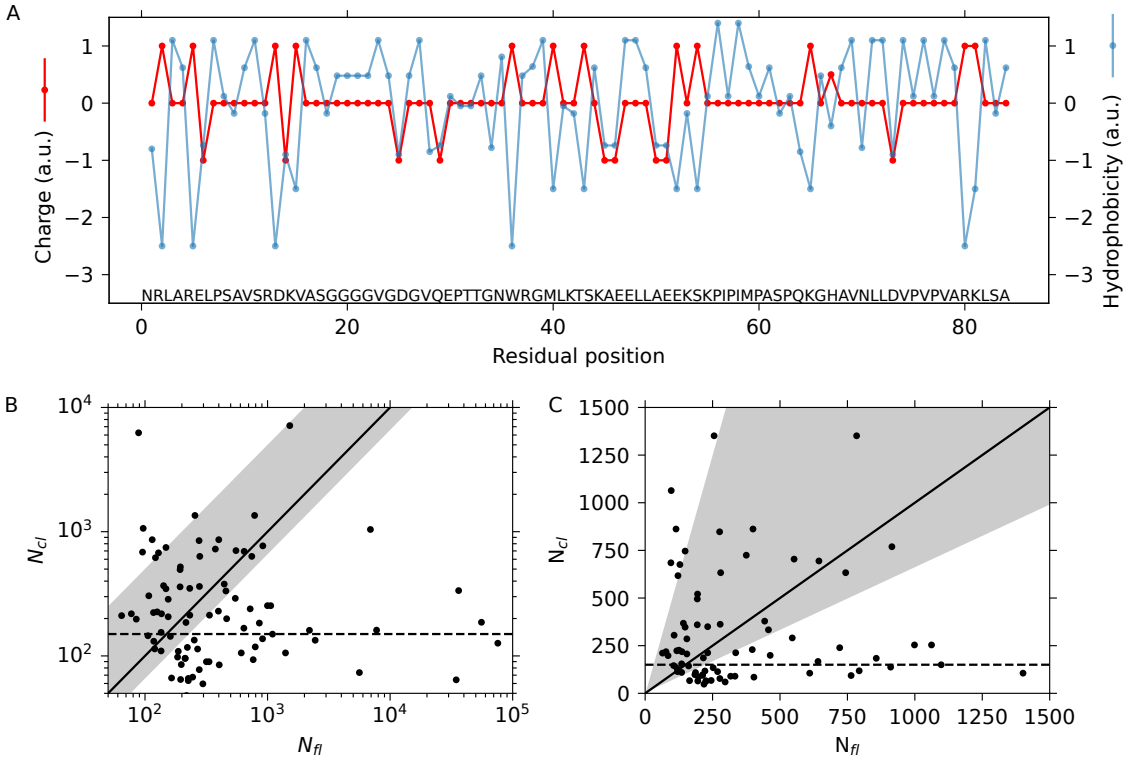

Fig. 4.7 | Number of cardiolipin that is potentially bound by DRP1. A, Sequence characteristics of a WT-VD-domain where the properties of the individual residues are shown in terms of charge and hydrophobicity. B, Double logarithmic plot of the number of bound cardiolipins vs. the number of DRP1 molecules per fluorescent oligmer for the whole dataset. C, Linear plot for the region with smaller stoichiometries. Black lines correspond to a 1:1 stoichiometry. The grey area corresponds to a stoichiometry of 0.66–5 cardiolipin per DRP1.

4.2.7. Oligomer merging of DRP1

Within the particle traces analysis, I observed that some of the tracked particles fused together and changed their diffusion coefficient. To further investigate this effect, I plotted the tracked traces of DRP1 and a time resolved diffusion coefficient (Fig. 4.8). The time resolved diffusion coefficients has been calculated by splitting each trace into smaller section, for example the blue trace in Fig. 4.8A has been split into 3 segments where the black trace has been split into 10 segments that correlate with the number of diffusion data points. The lag time has been chosen two be rather short with 0.3 s, which corresponds to three frames, to calculate a segmented MSD. The error bar corresponds to the standard error of the fit from the MSD analysis. Both experiments were performed as described in Chapter 4.2.3. Two example traces are shown in Fig. 4.8. One had a membrane tether radius of 145 nm (Fig. 4.8A) and the other a membrane tether radius of 61 nm (Fig. 4.8B). While the fluorescent intensities of the merged oligomers roughly corresponded to the sum of the individual oligomers prior to the merged, the diffusion coefficient only changed for the large membrane tube radius in the time resolved diffusion coefficient. Thus, DRP1 oligomers diffusion may depend on the tube radius and membrane tension. On the other hand if I calculate the diffusion coefficient without segmentation. We can see a reduction in both cases, Fig. 4.8A — $0.01757 \pm 0.0008\,\mu m^2/s$ (blue), $0.03728 \pm 0.0004\,\mu m^2/s$ (black), $0.0011 \pm 0.0002\,\mu m^2/s$ (orange) and in B — 0.0385 $\pm 0.002\,\mu m^2/s$ (blue), $0.0321 \pm 0.002\,\mu m^2/s$ (black), $0.009 \pm 0.002\,\mu m^2/s$ (orange). Due to the high density of oligomers on the membrane tethers, it was difficult to analyze merging events and their consequence for diffusion and fission.

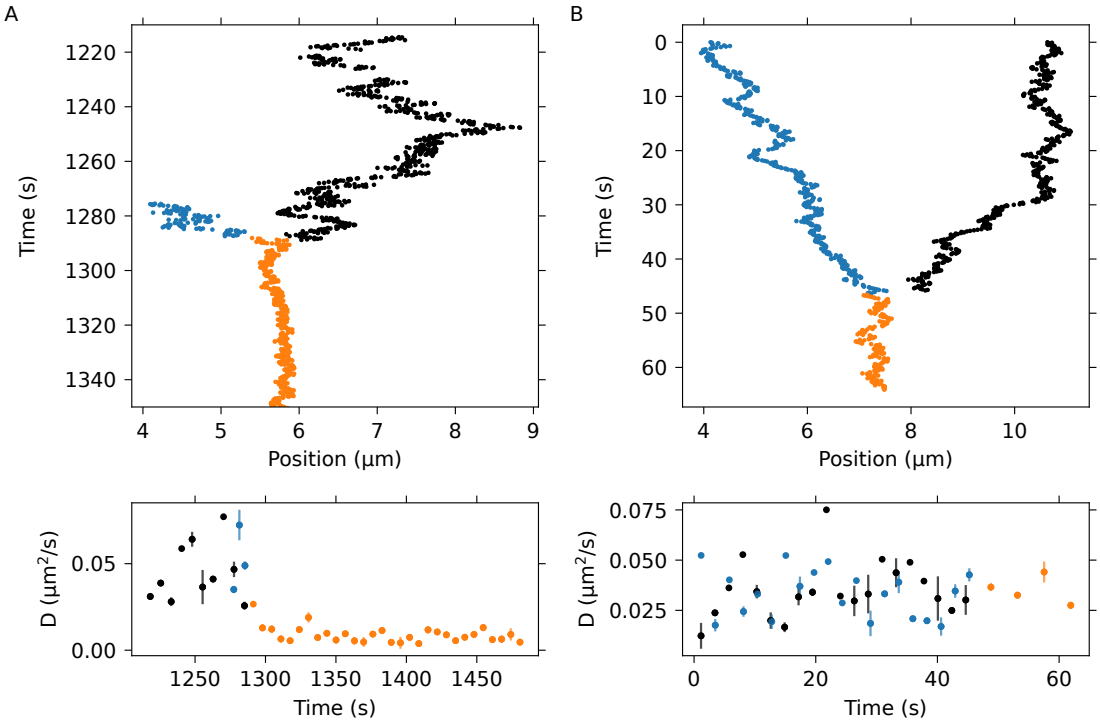

Fig. 4.8 | Oligomer merging while diffusing on a membrane tether. A, Two DRP1 oligomers merged and show a significant reduction in the time resolved diffusion coefficient by approximately a factor of 10 (mean oligomer size based on t fluorescence 297 (black), 285 (blue) and 495 (orange). B, Two clusters merge in florescence but do not show a significant change in the diffusion coefficient (mean oligomer size based on the fluorescence 165 (black), 189 (blue) and 472 (orange).

4.2.8. Bouncing membrane inclusion

Apart from merging DRP1 oligomers, I mad an observation. I recorded a fast movement of a membrane inclusion inside a pulled membrane tube. Some of the GUVs prepared by electroformation contained small membrane fragments or small vesicles. One of these small vesicles was pulled into the membrane tether during its formation. The sample was prepared as mentioned before in Chapter 4.2.3. Snapshots of the video are shown as a time series along with the tracked position in Fig. 4.9. In a periodic fashion, the inclusion moved very fast away from the GUV over micrometer distances and then slowly moved back to the GUV. In general, for visualization it turned out that the geometry of the membrane system lead to a significant halo around the GUV. We attribute the halo to the close proximity of the image plane and to the sample surface. The attached bottom surface of the hemispherical GUV is a fluorescent disc. The image plane is a few micrometer above the glass surface and, therefore, is causing out-of-focus fluorescent intensity in the image plane. Near the GUV this out-of-focus contribution causes a halo around the GUV that extends several micrometers along the membrane tether. Therefore, it was difficult to set a reasonable contrast setting for the whole image. I decided to normalize the image and thereby remove the constant background in analogy to iScat experiments [200]. In Fig. 4.9, the membrane channel is shown, normalized the fluorescent intensity to the median of the whole video. From the tracked position I, also calculated a frame to frame velocity in Fig. 4.9C, which was on average $\approx 800\,\mathrm{nm/s}$ in the beginning decreasing to $\approx 500\,\mathrm{nm/s}$ after about 100s. Maximum speeds $v_{\max}$ were around $5\,\mu\mathrm{m/s}$. Based on the estimated size of the inclusion, the drag force it should experience

$$F_{drag} = 6\pi\eta r v_{\max} = 0.5\,pN \tag{4.2.8}$$

using a viscosity of $\eta = 0.9\,\mathrm{mPas}$ for water at a temperature of 28.2 ℃and a radius of $r = 630\,\mathrm{nm}$. Since the movement of the inclusion also effected the membrane. That has a higher viscosity, drag forces were likely higher. Nevertheless, piconewton forces were generated by an active mechanism in the presence of DRP1.

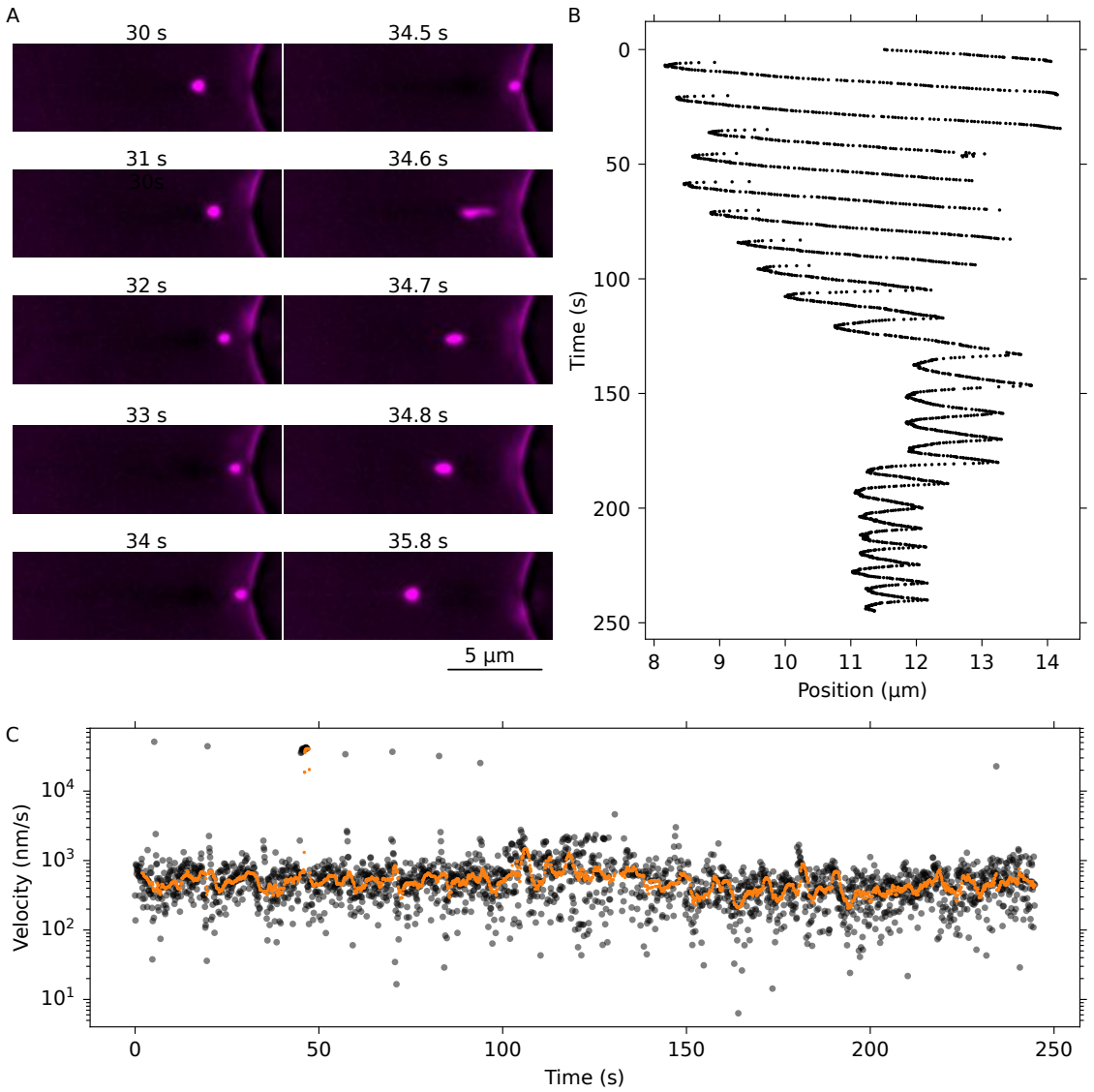

Fig. 4.9 | Bouncing membrane inclusion. A, Time series of a moving membrane inclusion in a tether. B, Tracked position of the membrane inclusion as a function of time. The traces in the beginning show remarkable velocities and therefore, could not be tracked as a single trace with the software. Traces were stitched together manually. C, Sequential speed calculated form the frame to frame displacement (grey points). Orange point were filtered by a window 20 data with a rolling mean.

4.2.9. Tether fission

Severing of a membrane tether has only recently been observed in vitro for the first time in 2018 [182] in the presence of DRP1. In my experiments it was possible

to reproduce this effect under different experimental conditions. In Fig. 4.10 and 4.11 I show two examples for a membrane bound DRP1 oligomer freely diffusing on the GUVs surface or on the membrane tubes surface, suddenly changed its diffusion coefficient and then severing the membrane tether. To correct for the GUV halo , a background image after the severing was chosen. Therefore, the optical trap position appears to be darker then the background signal. After severing the cut membrane tube was pulled back into the trap by the membrane tension and remodeled itself. In Fig. 4.10 I displayed a time series where DRP1 is binding mainly on the GUV. Since a cross-section is displayed, DRP1 oligomers are diffusing in and out of the focal plane. Also over time more oligomers were binding. Unfortunately, in 180 s and 364 s of the experiment, a membrane bound DRP1 was trapped in the optical tweezers introducing a background signal. The tracked oligomeres in Fig. 4.10A have a size of 232-464 (black) and 363–727 (blue). At around 490.8s, a DRP1 oligomer stopped its free lateral diffusion on the GUV surface and was locked in place at the point where the membrane tether originated from GUV. From this point it took $\approx$ 16.5 s until the membrane tube was severed.

We also observed that DRP1 oligomers diffused on the membrane tube and severed the tether in the middle. In Fig. 4.11A, we tracked two diffusing DRP1 oligomers. A sudden change in the diffusion coefficient can be observed at $\approx$400 s. The marked time points Ⓑ,Ⓒ, and Ⓓ show the corresponding fluorescent images and line profiles in Fig. 4.11B–D. In Fig. 4.11D we correlated an intensity change in the red channel of the membrane with the slowly diffusing oligomer in the green channel. At this position, the membrane tether is severed. From the time-resolved diffusion coefficient in Fig. 4.11E, we observed that a step-like reduction occurred after $\approx$400s. Four ROI of 5×5 pixel termed quadrant 1–4 were selected around the severing site. To visualize the local intensity change, we calculated the difference between q3 and q2 for every frame in the video. Additionally, as controls we calculate the differential intensity change q1-q2 and q3-q4. Concurrent with the reduciton in the diffusion coefficient, the membrane intensity decreased across the DRP1 oligomer (4.11E). A decrease in membrane intensity suggests that the membrane tether radius was reduced by the constriction of the DRP1 oligomers. From the initiation of constriction to fission, it took about 25 s. Based on the intensity reduction the tether radius was reduced from 40 nm to about 32 nm. The oligomer had a size of 134–268 monomers. Overall I was able to pull 60 membrane tethers, where I observed binding of DRP1. No fission was observed without GTP. Out of these 15 fission events have been recorded resulting in a cutting efficiency of 25 %. From these 15 fission events, the membrane tether was cut at the tether attachment point of the GUV and the membrane tether 4 times. The tether was cut in the middle between the GUV and the microsphere 5 times. It was severed 6 times close to the or at the microsphere. For observed fission events, tether radii were larger than 40 nm while the size of all pulled membrane tethers ranged from 6–225 nm. The smallest oligomere performing fission was between 103–206 DRP1 molecules.

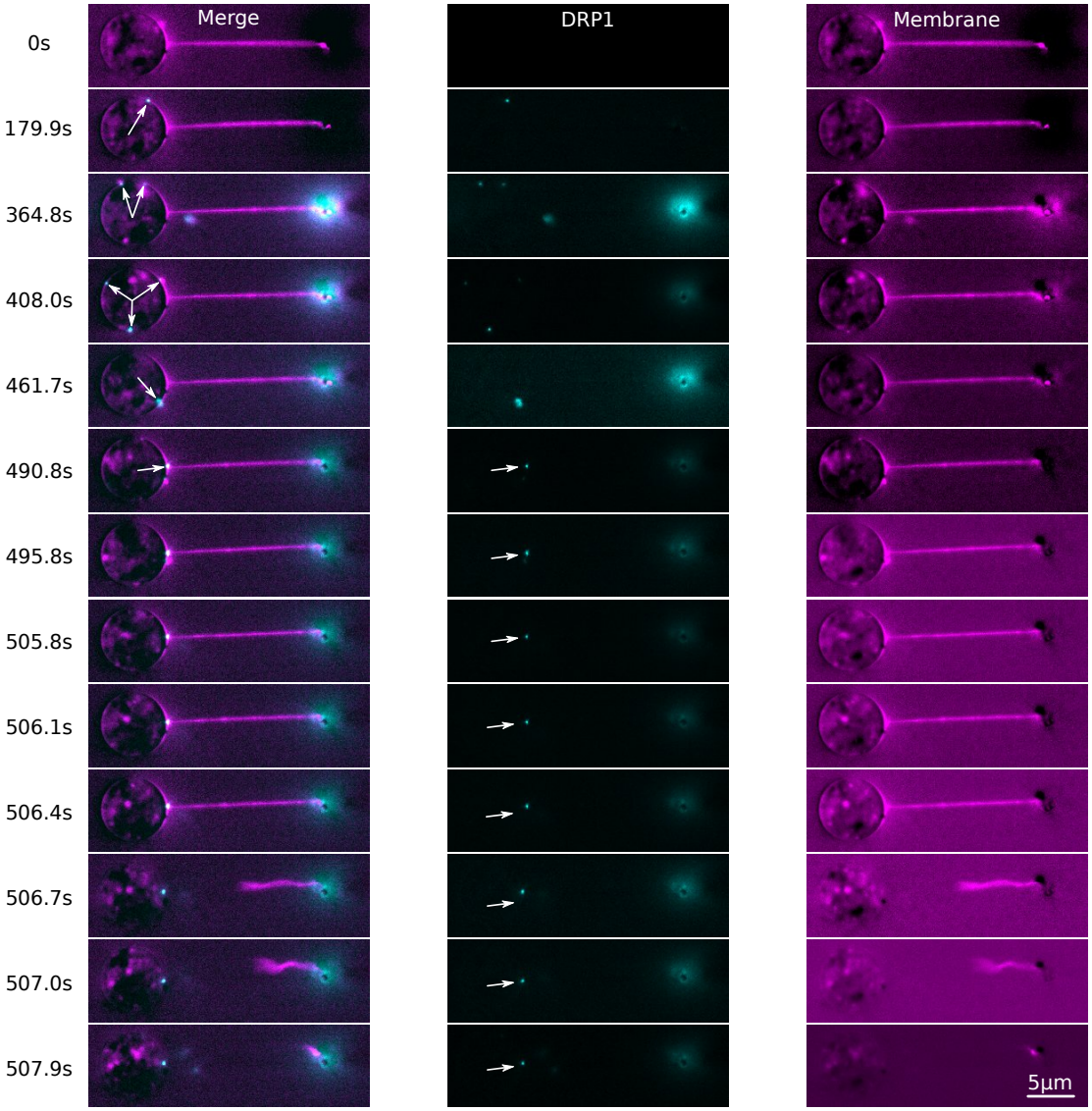

Fig. 4.10 | Time series of tether severing at the GUV. The white arrows mark the moment when a DRP1 oligomer was immobilized on the GUV at the attachment point between GUV and the pulled membrane tether. The oligomere stayed at this location until the membrane tube was cut from the GUV and then continued to diffuse on the GUVs membrane (not shown here). Intensity based size of the oligomere is 1361-2722 DRP1 monomers.

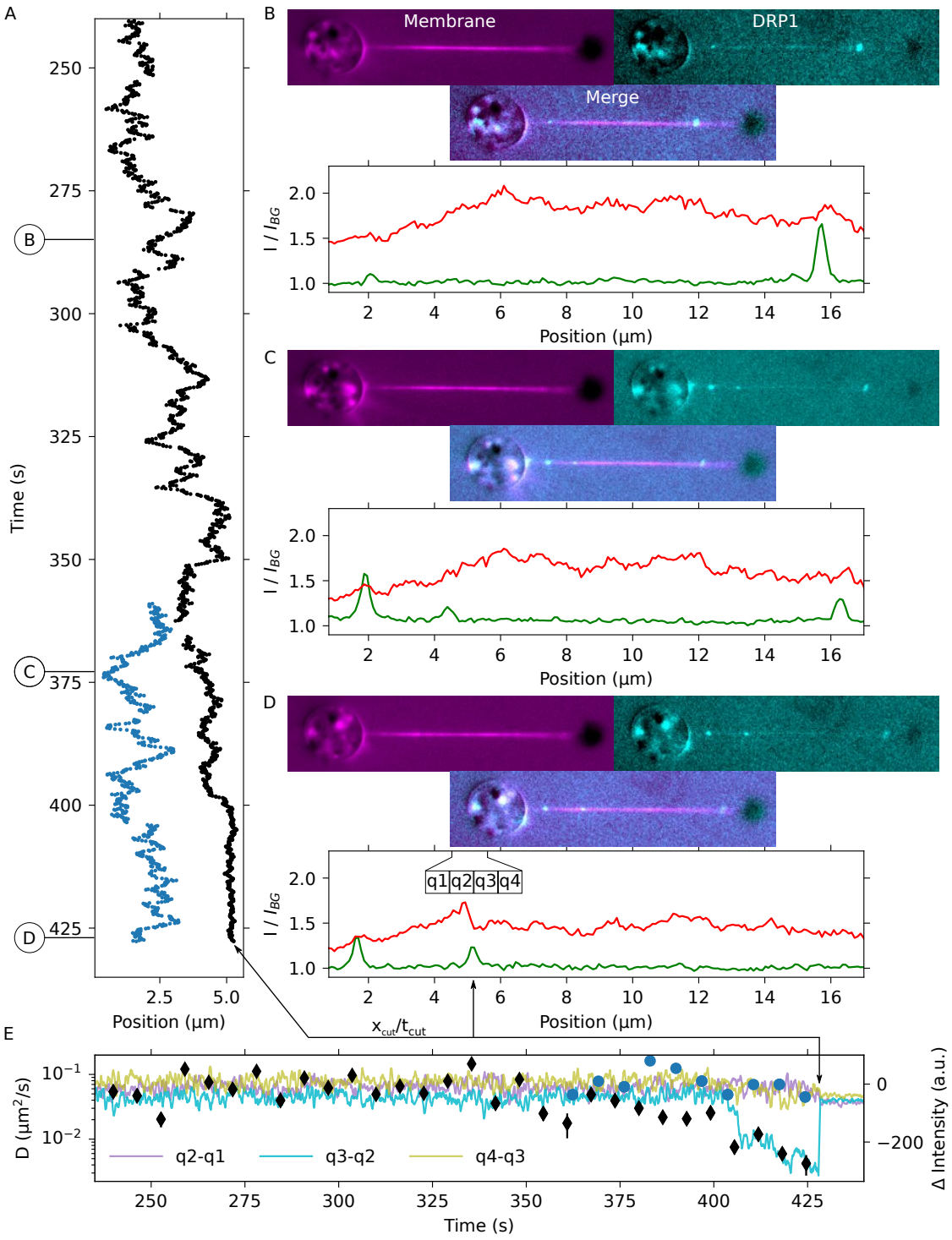

Fig. 4.11 | Diffusion lock. A, Tracked position of DRP1 oligomers. B–D, Fluorescence images and line profiles along the tether at different time points indicated. E, Time-resolved diffusion coefficient and differential intensity change for quadrants q1–q4 along the tether (circles are the blue trace in A, diamonds are the black trace in A, respectively).

4.3. Discussion & conclusion

DRP1 and microtubule co-localization

Microtubules and DRP1 bound to each other in a three microtubule per bundle preference under the conditions tested here. The dimensions of a bundle containing three microtubules is 54 nm in diameter with a single microtubule having a diameter of 25 nm in diameter. This diameter is in the range of previously reported membrane tethers DRP1 was binding to [39, 175]. Microtubule bundles are known to be formed by a variety of microtuble associated proteins e.g. during cell division [201]. The biological function of DRP1 binding remains an open question. One can speculate under the assumption that DRP1 is polymerizing around microtubule bundles that DRP1 provides additional stability that is needed during cell division. Also, microtubule bundles may serve as a reservoir for DRP1 molecules.

Diffusion coefficients of DRP1 on membrane tethers

Using GUVs fixed on a supported lipid bilayer enabled me to study the binding and severing behavior of DRP1 on membrane tethers. To enable long observation times, the experiments were performed at a low laser power 1 mW for 488 nm exciation. At the time, the experiments were performed, the *in vitro* tether fission [182] was not reported yet. Therefore fission times were unkown and I maximized the observation time that was limited by photo bleaching. Therefore only diffusion coefficients of larger DRP1 oligomers were measured. The observed diffusion coefficients are remarkably different from typical diffusion coefficients measured in bulk. To illustrate the order of magnitude, a diffusing sphere with a diffusion coefficient $D \approx 0.01\,\mu m^2/s$ as measured in Chapter 4.4E for DRP1 oligomere would have a radius of

$$r = \frac{k_B T}{6\pi\eta D} = 2.44\,\mu m, \tag{4.3.1}$$

assuming Stokes drag in water at room temperature. Since the tracked oligomers were diffraction limited objects the diffusion was most likely influenced and slowed down by the membranes viscosity. Typical values for diffusion coefficients of single lipids (single cardiolipin is around $\approx 5\,\mu m^2/s$ [190]) or integral membrane proteins like KvAP are 1–4 $\mu m^2/s$, which have been explored on GUVs [188] and pulled tethers [147]. A microdomain has a comparable diffusion coefficient [191, 192]. The order of the magnitude of measured D values seems to indicate that the typical reduction of the diffusion coefficient was not induced by the confined geometry of a membrane tether. In Fig. 4.5, I tried to correlate the existing model for diffusion in tethers, proposed by Daniels and Turner [194], with our data. The data did not indicate any correlation with the model. Further, it is possible that the intensity based stoichiometry was inaccurate due to the labelling ratio of 1–2

fluorophore per DRP1 with an additional uncertainty induced by the bleaching-step-based calibration in Chapter 4.2.2. It could also be possible that not all DRP1 in a diffraction limited focus were interacting with the membrane tether. The sample chamber—even though carefully cleaned from GUV/membrane fragments—could contain small free membrane parts in solution that DRP1 may binding to. Since the experiments were performed at low laser powers, small membrane parts and small DRP1 oligomers could lead to the only partial interaction. The measured diffusion coefficients were an indicator for how many DRP1 molecules interacted with the membrane tether. Based on the known surface packing geometry from Francy et al. [175], I also estimated the covered tether length by DRP1 polymers. With some of these oligomers having a length of almost 1 µm, we should have seen at least an asymmetric intensity distribution or even lines, which was not the case. Thus, this length estimate also suggest that not all DRP1 molecules in an oligomer were directly in contact with the tether. Also, the assumption that the tether radius R_0 is much larger then the protein radius a was not fulfilled for the approximation to the model by Daniels and Turner. The sensitivity of the experimental settings provides a minimum detection of around 35–70 DRP1 monomers (Chapter 4.2.2). If we use the geometry from Francy et al. [175], this number would already mean 2–4 full helical turns around a 30 nm diameter tube with 9 dimers per helical turn. Thus, the smallest oligomers, we detected, were too large to be described by the model.

Bound fraction of DRP1 based on the diffusion coefficient

It has been shown that cardiolipin can induce binding of DRP1 to GUVs [131] possibly by its VD domain. We derived a simple model based on the diffusion coefficient of cardiolipin of how many DRP1 molecules were interacting with how many cardiolipin molecules. The data suggest that each DRP1 molecule bind can 1–5 cardiolipins based on the positive charge distribution of the VD-domain. Indeed many data point corresponded to this ratio as indicated in the grey area of Fig. 4.7. For those that are not within this area, one can assume that less DRP1 molecules were bound to the membrane tether than were contained in the oligomere itself. Since DRP1 forms polymers, I illustrated in Fig. 4.12 situations that may occurred based on the shown data. The overall size of the binding oligomers is a few hundred molecules. Since DRP1 is forming helical structures, binding of a DRP1 oligomer may not immediately lead to a correct arrangement on the membrane tether, but instead lead only to an wrapping of the tether of a few turns with the rest of the oligomer remaining in solution without or with only little contact to the membrane. This conclusion is further supported by the observation that DRP1 oligomers also bound to the GUV surface where no wrapping in form of a helical tether is possible. Still such oligomers can lead to fission of the membrane tether once landed on it (Fig. 4.10). Oligomers that only partially attached to the membrane tether could

have an overhang of a helical DRP1 polymer that may attach over time to the membrane. It is also possible that instead of a rearrangement, the correctly attached part of the oligomer is growing by assembling with new dimers of DRP1 from solution to a matured helix. Such an overhang helix could also prevent oligomers from merging correctly since no correct oligomerization site can get into contact with each other (Fig. 4.12C1, C2). If two oligomers have the correct orientation, they may merge(Fig. 4.12D1 to D2). A matured helix then constricts the membrane tether (Fig. 4.12E) and can lead to fission.

Oligomer merging of DRP1

Oligomer merging did not necessarily lead to diffusion coefficient changes or tether severing. The observed oligomer size unfortunately did not clearly indicate a minimum number of DRP1 molecules necessary to lead to a diffusion lock shown in Fig. 4.8A. This might be another indication that not all tether-bound DRP1 were assembled in a functional helix structure and that the orientation of potential overhangs may also play a role.

Bouncing membrane inclusion

The measured phenomena of the bouncing membrane inclusion is an active process requiring an energy source. The components in this experiments GTP and DRP1 suggest requiring an energy source that the GTPase activity of DRP1 could be the origin of this movement. However to my knowledge, typical polymerization speeds are much slower. For example, microtubule growth speeds of $\approx 0.66 \pm 0.02\,\mu m/min$ [202], actin filament or fillipodia formation are all much slower compared to the average speed measured for the inclusion. Also the reported polymerization speed of DRP1 ($75 \pm 19\,nm\,min^{-1}$, [39]) is far below the here measured velocities. Therefore, we suggest that this effect is caused by the membrane inclusion and force generation of the optical tweezers. The inclusion is introducing an additional bending of the membrane tether disturbing the stable solution of Equation (3.1.2). Unfortunately, I was unable to solve the new geometry with the outcome a of e.g. a second tether radius that might explain the jumping between two semi-stable states.

Tether fission

It was possible independently observe the membrane severing that has first been documented by Kamerkar et al. in 2018 [182]. Under the experimental conditions that are more similar to the once used here, no severing was observed previously by Ugarte-Uribe also in 2018 [39]. Kamerkar et al. performed experiments at 25 °C and 37 °C, Ugarte-Uribe et al. used 20–22°Cwhile I worked at 28.2 °C. The concentration of DRP1 was also different. While both previous studies used micro-molar DRP1

concentrations resulting in completely covered membrane tethers or completely covered GUV surfaces, I performed experiments at 10 nM. My experimental conditions resulted in a sparsely covered membrane surface where distinct foci were visible. These conditions might reflect the *in vivo* situation more accurately since mostly small foci have been observed dividing on mitochondiria. Also note that Kamerkar et al. used DRP1 isoform 3, which is the shortest version of the protein, where the loop in the variable domain is shorter. Also a DRP1-GFP version was used compared to the Alexa-labelled version used here. GFP was fused to the C-terminal end of DRP1, which is quite unusual since all reports up to now used an N-terminal tag or the protein itself without any tag. Whether the chemical labeling here affected the functionality of DRP1 or of a subset of molecules is unknown. In Fig. 4.11 it was possible to correlate the position of a DRP1 oligomer with a reduction of membrane intensity and a reduced diffusion coefficient. This suggests that a DRP1 helix has formed and constricted the membrane. Since the surface coverage of the membrane tether with DRP1 is very low, the overall detected change is minimal. Based on the suggested helix overhangs, DRP1 either reoriented the helix or the helix grow to a functional conformation (where in Fig. 4.12 D1 may have become D2, or D2 has matured from the incorporation of single DRP1 dimers, to E which can perform constriction). I was able to observe 15 tether fission event, where no significant preference for the position seemed to be present. One can speculate on the properties of cardiolipin about a possible preference. As previously stated cardolipin can induce binding of DRP1 to membranes. Cardiolipin prefers negative curved regions on a membrane [203], which would be in this geometry the attachment point tether to GUV or potentially the trapped microsphere if the contract radius is larger then the tether radius.. If an enrichment of cardiolipin occurs at the tether ends, and DPR1 is binding via its VD domain to cardiolipin, we should see a cutting preference there. In deed, 10 out of 15 severing events occurred at the tether ends. If the fission probability would be independent of position then the end probability should be very small because the ends represent only a small percentage of the overall tether length. Thus, it is likely that there is a curvature preference for cutting. This curvature sensitivity may be indirect via cardiolipin over the VD-domain since there is to my knowledge no curvature sensitivity mediated like by the PH-domain in dynamin [179]. The smallest oligomere that performed severing of a tether was between 103–206 DRP1 monomers, in the middle of a tube. This lower limit is comparable to recent *in vivo* values of ≈100 DRP1 molecules forming a functional fission complex [181]. For all experiments, I also recorded the force signal form the optical tweezers. Unfortunately, I could not detect any force increase or decrease that I could correlate to DRP1 binding or binding. Reasons for that could be that the changes were below the detection limit of the system. The low concentration of DRP1 created only individual oligmers binding to the membrane. If only a very small portion of the membrane tether is deformed, the change might be to small to be detected in the background of the Brownian motion of the trapped

microsphere. In contrast, a force change of 60 pN was measured for the collective behavior of the whole membrane tether being coated by ESCRTs and Vps4 [109]. Based on the noise of the force signal, we can estimate that forces associated with binding and constriction of the membrane tether were below ≈0.6 pN, at a typical trapping laser power of 30%. Remnant noise due to the backscattering detection may have masked any force changes.

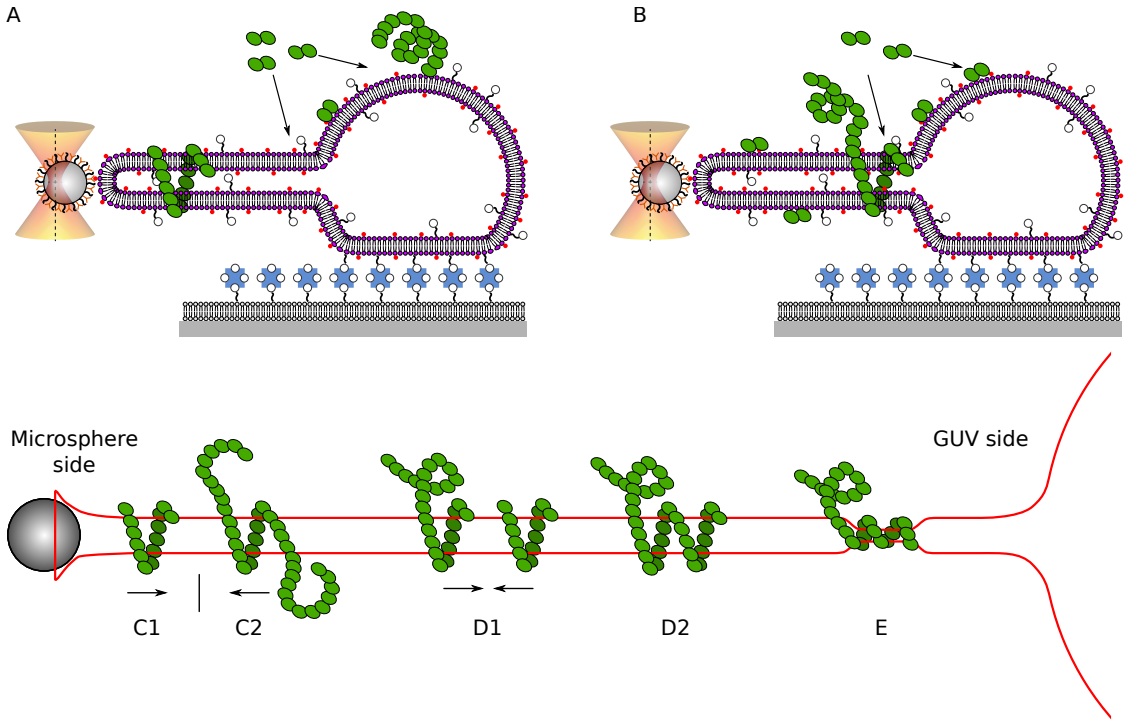

Fig. 4.12 | Model based on the diffusion coefficients and fluorescent oligomer state. A&B, interpretation of the bound DRP1 diffusion coefficients and fluorescent stoichiometry discrepancy. Incomplete binding of DRP1 polymer to the membrane. C1&C2, Oligomers that can not merge because of a overhang that does not provide a binding site. D1, Oligomers with binding sites may fuse to a matured helix (D2), that could also form from growing helix based on DRP1 in solution.

Part IV.

Closure

5. Outlook

Advances in scientific setups and methods are driving the scientific community forward. The novel combination of techniques and features or the enhancement of increasing the resolution/sensitivity is an ongoing procedure to which this thesis contributed.
I developed a vibration isolation system that performs very well in the low frequency range and out compete commercial systems. Our system is very modular and can be adapted to a variety of situations. The rubber-based dampening elements for the surge frequency of the spring should be exchanged with a more durable rubber, because they get porous over time. Possible materials to dampen the surge frequency that have not been tested, yet, are e.g foam made of polyethylen, polystyrene, PET or other polymers. One could also redesign an enclosure for the steel springs to immerse them completely in highly viscous silicone oil. The system overall would of course also benefit from higher ceiling heights since this will further reduce the resonance frequency.
Further, I developed a hybrid optical tweezers, which is combined with a fluorescence, TIRF, interference reflection microscopy and a heating laser. The system has been checked for functionality. During this where I encountered unidentified noise signal that has been successfully filtered out by the CO filter. This so-called noise could be further explored. Ou current hypothesis is that this signal is rotational signal. Since a central obstruction filter is blocking the center of the beam I suggest as an optimization the use of an axicon[204, 205]. This optical element can invert the beam profile, meaning that it rearranges the high intensities of the beam to the outside and the low intensity to the center in a doughnut like shape. Unfortunately, while I was testing the implementation of an axicon in my optical tweezers, I realized that a complete re-design of the optical path would have been necessary for beam profile inversion. The advantage of the axicon would be a reduction of back scattering that reduces the scattering force. This allows to use trap objects deeper in aqueous media with lower NA objectives [204]. In our case it should reduce the amount of backscattered light from static surfaces improving backscattering detection. This inverted beam profile also resembles the use of a CO filter in the incident trapping path as used by Sischka et al. [59] for backscattered detection without blocking the center of the beam and loosing most of its intensity. Another possible change on the microscope that could be beneficial is the motorization of the heating laser. This could in principle be achieved by using a low NA objective on the upper space above the objective. I tested

the transmission rates for the objectives and observed that our 60× TIRf objective has a transmission of $T_{60x} = 20\,\mathrm{mW}/142\,\mathrm{mW} = 0.14$ and a 40× objective can provide $T_{40x} = 121\,\mathrm{mW}/142\,\mathrm{mW} = 0.85$. The higher transmission should enable to heat more or a larger area. The heating laser can also be used to study different effects where local heating may be helpful like phase transition of lipids, temperature–sensitive or temperature–dependent activity of proteins or thermo–diffusion (thermophoresis).
The initial idea of pulling membrane tubes from surface immobilized vesicles in the evanescent field of the TIRF microscope resulted in a variety of problems. The major one was the surface preparation. The initial method was based on silanization[quelle] led to a degradation of surface immobilized vesicles. A significant improvement was made by using the supported lipid bilayers which solved the degradation issue. For pulling a membrane tube it turned out that point defects or small areas within the bilayer caused the tube to get pinned to the surface. This effect has also been observed for a passivation with PEG on the surface [135, 136] where these small imperfections were used to fix membrane tubes to the surface. Here, this effect was unwanted. We wanted a free floating tube without any surface attachments. To measure force simultaneously for the membrane tether that I pulled in the evanescent TIRF field, either they started to stick immediately or got pinned on one point resulting in a uneven position in the excitation field eventually leading to intensity differences along the tether. For future experiments, I suggest a different approach. One could use glass microspheres and stick them on the sample surface. Then one could coat the surface and spheres with a supported lipid bilayer. The diameter of these spheres should be around a few micrometers for pulling a tether well above the surface or roughly 300-400 nm diameter for pulling in the evanescent field. Alternatively large micosphere could be melted on the coverslip crating hemispheres. A smaller microsphere could be used for pulling membrane tubes. The advantage would be a fixed distance between the surface and the pulled membrane tube chosen to be optimal for imaging. The radius of a membrane tube could be calculated by fluorescent intensity measurements similar to those I performed. Because GUVs would not have to be attached to the membrane support, also membrane tethers should not bind to the surface anymore. This approach should allow to pull membrane tethers in the TIRF field. With TIRF, it should be feasible to detect singe DRP1 molecules.
The performed experiments on DRP1 confirmed the tether severing. I was able to observe oligomer DRP1 binding and diffusion on GUVs and on membrane tethers. My experiments have been performed under constant conditions, membrane composition, temperature and DRP1 concentration. Also note that we did not, add any mitochondrial fission factor that can "dramatically improve DPR1s membrane binding" [182]. For future experiments, one could test for different cardiolipin compositions and additional mitochondiral fission factor that potentially enhance binding. The very same experiment could also be repeated with DRP1 having a

controlled labeling ratio of 1:1. To my knowledge, the effect of merging oligomers with a change in the diffusion coefficient have not been reported for DRP1 *in vitro* , yet. To explore this effect further, one could perform concentration dependent experiments. More interesting might be to improve the sensitivity to be able to detect smaller oligomers as discussed above. This would mean higher laser powers, which would reduce the time of observation as a trade-off for the sensitivity. The single-molecule level could be achieved, but might not be favorable here. First, the time scale for fission seems to on the order of a few tens of seconds. Second, a single DRP1 or dimer cannot perform severing.

This novel combination of optical tweezers, fluorescence, IRM, a heating laser and the development of the new assay allowed new insights into membrane protein interactions. I am convinced, as technology is advancing and new combinations of microscopy techniques or experimental assays emerge, there will be always something new to discover.

Contributions

Chapter 1 - Stabilized Environment for Optical Tweezers

Edgar Raid and the wood workshop assembled the wooden frame for concrete block shown in Fig. 1.3 from Chapter 1.3.1. The concrete was kindly provided by the construction side of you building as well as the paint, which is the same one used for the floors the be a S1 area. The results of Chapter 1.3.2 have been published [6]. Erik Schäffer, Gero Lutz Hermsdorf and Sven A. Szilagyi designed the research, Gero Lutz Hermsdorf, Sven A. Szilagyi, and Sebastian Rösch built the system, Gero Lutz Hermsdorf, and Sven A. Szilagyi performed measurements, Gero Lutz Hermsdorf, Sven A. Szilagyi, and E.S. analyzed the data, and Gero Lutz Hermsdorf, and Erik Schäffer wrote the manuscript. Sven A. Szilagyi and Sebastian Rösch have been students/student helper/ or master students at during the project and have been supervised by me.

Chapter 2 - Custom Built Instrument

All optomechanical parts that were not commercial available have been designed my myself and were produced by a company "Kotzur Mechanische Fertigung" or the mechanical workshop of the university(Edgar Raidt and colleages). Mehrbod Soleimani Aligodarzi, contributed to the design of the optical tweezers in Chapter 2.3.3. Mehrbod Soleimani Aligodarzi planned the heating laser electronics that I later assembled and used together with Moritz Burmeister in Chapter 2.3.6. The heating laser profiles and temperature calibrations have been recorded together with Moritz Burmeister during his Bachelor thesis. Sebastian Rösch assisted with the installation of the temperature sensors and related electronics for the temperature feedback as a student helper, Chapter 2.3.10.

Chapter 3 - Tetherpulling with DOPC vesicles

The protocoll for the supported lipid bilayer has been kindly provided by Katia Cosentino. The use of a solid lipid with this protocol has been checked by Tobias Jachowski and Michael Kittelberger, which I used without further modification in Chapter 3.2.3.

The microsphere functionalization protocol in Chapter 3.2.1 has been previously optimized and provided from Tobias Jachowski.

Chapter 4 - DRP1 experiments

The purified protein and labelled DRP1 was kindly provided by Begoña Ugarte Uribe and Andreas Jenner. GTPase assays in section 4.2.1 were planed by Begoña Ugarte Uribe and performed together.

Software

Tobi Jachowski and Steve Simmert developed the Poytic software used here to analyze optical tweezers data. Steve Simmert provided a first version of a scipt to fitting and plotting of the intensity profiles in Chapter 3 & 4. Steve Simmert provided a python script and fitting used in Chapter 2.3.3.3 for the intensity calbiration of the servo, which I extended. Moritz Burmeister wrote the LabView software to control the heatinglaser intensity within his Bachelor thesis Chapter 2.3.6. Mohammed Kazem Abdosamadi developed a overlay tool for fluorescent images that I have used. Erik Schäffer, Mohammad Mahamdeh, Steve Simmert, Tobias Jachowsik and other members of the Schäffer lab that have developed the LabView based control software for the custom built instrument,Chapter 2. I was able to use most of the old programs with slight modifications.
A major fraction of this thesis was created by the use of free and open source software. The following list of software and tools were very useful and their developers shall be acknowledged! Debian Linux, Inkscape, LaTeX, Fiji, SVN, Python, Jupyter, numpy, scipy, matplotlib, lmfit, trackpy, pyotic, trackpy, pandas, scipy.

Publication list

Published

- **High performance passive vibration isolation system for optical tables using six-degree-of-freedom viscous damping combined with steel springs**
  Gero L. Hermsdorf, Sven A. Szilagyi, Sebastian Rösch, Erik Schäffer
  Review of Scientific Instruments 90, 015113 (2019)
  https://doi.org/10.1063/1.5060707

- **LED-based interference-reflection microscopy combined with optical tweezers for quantitative three-dimensional single microtubule imaging**
  Steve Simmert, Mohammad Kazem Abdosamadi, Gero L. Hermsdorf, Erik Schäffer
  Opt. Express 26, 14499-14513 (2018)
  https://doi.org/10.1364/OE.26.014499

In preparation

- **Supported solid lipid bilayers as a platform for single-molecule force measurements**
  Sudhakar, Swathi; Jachowski, Tobias; Kittelberger, Michael; Maqbool, Ammara; Gero L. Hermsdorf; Abdosamadi, Mohammad; Schäffer, Erik
  submitted

- **Reflected scanning light sheet microscopy for high-speed 3D imaging with single moleculesensitivity**
  Moritz Burmeister, Sven A. Szilagyi, Q. Tyrell Davis, Gero L. Hermsdorf, Suman De, Erik Schäffer, and Anita Jannasch
  in preparation

List of Figures

Abbreviations and notations

$\langle\cdot\rangle$	average
$\lfloor\cdot\rfloor$	floor function, *i.e.* round to nearest lower integer
PyOTC	Python Optical Tweezers Calibration package
PyOTIC	Python Optical Tweezers Investigator and Calibration software
vs.	versus
ADEV	Allan deviation
AQP0	aquaporin 0
AVAR	Allan variance
BFP	back focal plane
BFPI	back focal plane interferometry
BSD	backscattered detection
CAD	computer adided design
CO	central obstruction filter
comp.	compare
DIC	differential interference contrast
DM	dichroic mirror
DRP1	dynamin related protein 1
EM	electromagnetic
FFP	front focal plane
GFP	green fluorescent protein

GTP	Guanosintriphosphat
GUV	giant unilamellar vesical
HL	heating laser
HWP	half-wave plate
IRM	interference reflection microscopy
iScat	Interferometric scattering microscopy
JV	jetted vesicles
KvAP	curvature-coupled voltage-gated potassium channel
LED	light emitting diode
LUV	large unilaellar vesicle
MAP	membrane assosiated protein
MSD	mean square displacement
NA	numercial apterture
NI	National Instruments
PBS	polarizing beam splitter
PSD	power spectral density
QPD	Quadrant photo diode
QWP	quarter-wave plate
SDM	standard deviation of the mean
SEM	standard error of the mean
SPT	single particle tracking
STED	stimulated emission depletion
SUV	small unilamellar vesical
TC	temperture control
TIR	total internal reflection

TIRF	total internal reflection fluorescence
var	variance
VI	LabVIEW virtual instrument

Bibliography

1. Heinrich, V & Waugh, R. E. A piconewton force transducer and its application to measurement of the bending stiffness of phospholipid membranes. *Annals of biomedical engineering* **24,** 595–605. ISSN: 0090-6964 (1996).
2. Dasgupta, R. & Dimova, R. Inward and outward membrane tubes pulled from giant vesicles. *Journal of Physics D: Applied Physics* **47.** ISSN: 13616463 (2014).
3. Sorre, B. *et al.* Nature of curvature coupling of amphiphysin with membranes depends on its bound density. *Proceedings of the National Academy of Sciences* **109,** 173–178. ISSN: 0027-8424. http://www.pnas.org/cgi/doi/10.1073/pnas.1103594108 (2012).
4. Prévost, C. *et al.* IRSp53 senses negative membrane curvature and phase separates along membrane tubules. *Nature Communications* **6,** 8529. ISSN: 2041-1723. http://www.nature.com/doifinder/10.1038/ncomms9529 (2015).
5. Hermsdorf, G. *Total internal reflection fluorescence combined with optical tweezers to study membrane mechanics* Diplom (2013), 45.
6. Hermsdorf, G. L., Szilagyi, S. A., Rösch, S. & Schäffer, E. High performance passive vibration isolation system for optical tables using six-degree-of-freedom viscous damping combined with steel springs. *Review of Scientific Instruments* **90.** ISSN: 10897623 (2019).
7. Vér, I. L. & Beranek, L. L. *Noise and vibration control engineering: principles and applications* 966. ISBN: 978-0-471-44942-3 (John Wiley & Sons, University of Michigan, 2006).
8. Harris, C. M. & Piersol, A. G. *Harris' Shock and Vibration Handbook 5th ed* (eds Harris, C. M. & Piersol, A. G.) **9,** 65–66. ISBN: 0071370811 (McGraw-Hill, New York, 2002).
9. Nolting, W. *Theoretical Physics 1* ISBN: 9783642129483 (2016).
10. Landau, L. D. & Lifshitz, E. M. *Mechanics: Course of Theoretical Physics Vol. 1 (3rd ed.)* (Butterworth Heinemann, Oxford, 1976).

11. Accurion. *Compendium, Priciples of Halcyonics Active Vibration Isolation Technology* tech. rep. (Accurion, 2017), 3–4. https://www.accurion.com/active-vibration-isolation/technology/compendium{_}-{_}principles{_}-{_}a{~}.pdf.
12. Platus, D. L. Negative-stiffness-mechanism vibration isolation systems. *Proc. SPIE* **1619,** 44–54 (1991).
13. Workshops, A. F. M. *Vibration Solutions* tech. rep. 888 (1434 East 33rd St., Signal Hill, CA 90755, 2016), 1–3. http://www.afmworkshop.com/images/AFM{_}Vibration{_}Solution{_}Datasheet{_}2016.pdf.
14. Voigtlaender, Peter Coenen, Vasily Cherepanov, Peter Borgens, Thomas Duden, F. T. Low vibration laboratory with a single-stage vibration isolation for microscopy applications. *Rev. Sci. Instrum.* **88,** 23703. ISSN: 0034-6748 (2017).
15. Richman, S. J. *et al.* Multistage active vibration isolation system. *Review of Scientific Instruments* **69,** 2531–2538. ISSN: 0034-6748 (1998).
16. Kim, M. H., Kim, H. & Gweon, D.-G. D. G. Design and optimization of voice coil actuator for six degree of freedom active vibration isolation system using Halbach magnet array. *Rev. Sci. Instrum.* **83,** 105117. ISSN: 00346748 (2012).
17. Stephens, M., Saulson, P. & Kovalik, J. A double pendulum vibration isolation system for a laser interferometric gravitational wave antenna. *Rev. Sci. Instrum.* **62,** 924. ISSN: 00346748 (1991).
18. Martinez, R. V., Glavan, A. C., Keplinger, C., Oyetibo, A. I. & Whitesides, G. M. Soft Actuators and Robots that Are Resistant to Mechanical Damage. *Adv. Funct. Mater.* **24,** 3003–3010. ISSN: 16163028. arXiv: 0706.1062v1 (2014).
19. Rohatgi, A. *WebPlotDigitizer* 2019. https://automeris.io/WebPlotDigitizer.
20. Reitherman, R. K. *Earthquakes and Engineers* ISBN: 9780784410714 (2012).
21. Howells, D., Kusznir, N., O'Neill, D., Skipp, B. & Willmore, P. *Instrumentation for Ground Vibration and Earthquakes* (1978).
22. Mahamdeh, M. HIGH RESOLUTION OPTICAL TWEEZERS OPTIMIZED FOR BIOLOGICAL STUDIES, 324–327 (2011).
23. Jannasch, A. High performance photonic probes and applications of optical tweezers to molecular motors, 116 (2012).
24. Simmert, S. *Optical tweezers combined with interference reflection microscopy for quantitative trapping and 3D imaging* PhD thesis (Tübingen, 2018).

25. Schindelin, J. *et al.* Fiji: An open-source platform for biological-image analysis. *Nature Methods* **9,** 676–682. ISSN: 15487091 (2012).

26. Karioris, F. G. & Mendelson, K. S. A novel coupled oscillation demonstration. *Am. J. Phys.* **60,** 508–513. ISSN: 0002-9505 (1992).

27. Happel, J & Brenner, H. *Low reynolds number hydrodynamics* **3-4,** 273. ISBN: 9789024728770 (1983).

28. Sano, O. Mobility of a Small Sphere in a Viscous Fluid Confined in a Rigid Circular Cylinder of Finite Length. *J. Phys. Soc. Jpn.* **56,** 2713–2720. ISSN: 13474073 (1987).

29. Schäffer, E., Nørrelykke, S. F. & Howard, J. Surface forces and drag coefficients of microspheres near a plane surface measured with optical tweezers. *Langmuir* **23,** 3654–3665. ISSN: 07437463 (2007).

30. Felderhof, B. U. Transient flow of a viscous incompressible fluid in a circular tube after a sudden point impulse. *J. Fluid Mech.* **637,** 285–303. ISSN: 00221120 (2009).

31. Iwaya, K., Shimizu, R., Hashizume, T. & Hitosugi, T. Systematic analyses of vibration noise of a vibration isolation system for high-resolution scanning tunneling microscopes. *Review of Scientific Instruments* **82.** ISSN: 00346748 (2011).

32. Sorre, B. *et al.* Curvature-driven lipid sorting needs proximity to a demixing point and is aided by proteins. *Proceedings of the National Academy of Sciences of the United States of America* **106,** 5622–6. ISSN: 1091-6490. http://www.pubmedcentral.nih.gov/articlerender.fcgi?artid=2667082{\&}tool=pmcentrez{\&}rendertype=abstract (2009).

33. Sorre, B. *et al.* Nature of curvature coupling of amphiphysin with membranes depends on its bound density. *Proceedings of the National Academy of Sciences of the United States of America* **109,** 173–8. ISSN: 1091-6490. http://www.pubmedcentral.nih.gov/articlerender.fcgi?artid=3252917{\&}tool=pmcentrez{\&}rendertype=abstract (2012).

34. Morlot, S. *et al.* Membrane shape at the edge of the dynamin helix sets location and duration of the fission reaction. *Cell* **151,** 619–629. ISSN: 00928674 (2012).

35. Ashkin, A., Dziedzic, J. M., Bjorkholm, J. & Chu, S. Observation of a single - beam gradient force optical trap for dielectric particles. *Optics letters* **43,** 623–629 (1986).

36. Chu, S., Bjorkholm, J. E., Ashkin, A & Cable, A. Experimental Observation of Optically Trapped Atoms. *Physical Review Letters* **57** (1986).

37. Bugiel, M. & Schäffer, E. Three-Dimensional Optical Tweezers Tracking Resolves Random Sideward Steps of the Kinesin-8 Kip3. *Biophysical Journal* **115,** 1993–2002. ISSN: 15420086 (2018).

38. Guilford, W. H., Aust, L. E. & Bernd, K. K. Whole-cell flagellum-based motility studied using back focal plane interferometry in a laser trap transducer. *Conference Record - Asilomar Conference on Signals, Systems and Computers,* 178–182. ISSN: 10586393 (2006).

39. Ugarte-Uribe Begoña, K. K., García-Sáez, A. J., Prévost, C. & Bassereau, P. Drp1 polymerization stabilizes curved tubular membranes similar to those of constricted mitochondria. *Journal of Cell Science,* jcs.208603. ISSN: 0021-9533. http://jcs.biologists.org/content/joces/early/2017/12/18/jcs.208603.full.pdf{\%}0Ahttp://jcs.biologists.org/lookup/doi/10.1242/jcs.208603 (2018).

40. Ashkin, A. Forces of a single-beam gradient laser trap on a dielectric sphere in the ray optics regime. *Biophysical Journal* **61,** 569–582. ISSN: 00063495. http://dx.doi.org/10.1016/S0006-3495(92)81860-X (1992).

41. Neuman, K. C. & Block, S. M. Optical trapping. *The Review of scientific instruments* **75,** 2787–809. ISSN: 0034-6748. http://www.pubmedcentral.nih.gov/articlerender.fcgi?artid=1523313{\&}tool=pmcentrez{\&}rendertype=abstracthttp://www.ncbi.nlm.nih.gov/pubmed/16878180{\%}0Ahttp://www.pubmedcentral.nih.gov/articlerender.fcgi?artid=PMC1523313 (2004).

42. Wriedt, T. The Mie Theory - A Review. **169.** http://link.springer.com/10.1007/978-3-642-28738-1 (2012).

43. Chýlek, P. & Zhan, J. *Absorption and scattering of light by small particles: the interference structure* **28,** 3984 (2004).

44. Nieminen, T. A. *et al.* Optical tweezers computational toolbox. *Journal of Optics A: Pure and Applied Optics* **9.** ISSN: 14644258 (2007).

45. Waterman, P. C. The T-matrix revisited. *Journal of the Optical Society of America A* **24,** 2257. ISSN: 1084-7529 (2007).

46. PRALLE, A., PRUMMER, M., FLORIN, E.-L., STELZER, E. & J.K.H. HOE RBER. Three-dimensional high-resolution particle tracking for optical tweezers by forward scattered light. *Microscopy Research and Technique* **44,** 378–386. ISSN: 1059-910X (1999).

47. Huisstede, J, van der Werf, K, Bennink, M & Subramaniam, V. Force detection in optical tweezers using backscattered light. *Optics express* **13,** 1113–1123. ISSN: 1094-4087 (2005).

48. Friese, M. E. J., Heckenberg, N. R. & Dearden, E. W. Determination of the force constant of a single-beam gradient trap by measurement of backscattered light. *Applied Optics* (1996).

49. Gittes, F. & Schmidt, C. F. Interference model for back-focal-plane displacement detection in optical tweezers. *Optics Letters* **23,** 7. ISSN: 0146-9592 (1998).

50. Moffitt, J. R., Chemla, Y. R., Smith, S. B. & Bustamante, C. Recent Advances in Optical Tweezers. *Annual Review of Biochemistry* **77,** 205–228. ISSN: 0066-4154 (2008).

51. Axelrod, D. Cell-substrate contacts illuminated by total internal reflection fluorescence. *Journal of Cell Biology* **89,** 141–145. ISSN: 0021-9525 (1981).

52. Mashanov, G. I., Tacon, D, Knight, a. E., Peckham, M & Molloy, J. E. Visualizing single molecules inside living cells using total internal reflection fluorescence microscopy. *Methods (San Diego, Calif.)* **29,** 142–152. ISSN: 1046-2023 (2003).

53. Simmert, S., Abdosamadi, M. K., Hermsdorf, G. & Schäffer, E. LED-based interference-reflection microscopy combined with optical tweezers for quantitative three-dimensional microtubule imaging. *Optics Express* **26,** 14499. ISSN: 1094-4087. https://doi.org/10.1364/OE.26.014499 (2018).

54. Ortega-Arroyo, J. & Kukura, P. Interferometric scattering microscopy (iSCAT): New frontiers in ultrafast and ultrasensitive optical microscopy. *Physical Chemistry Chemical Physics* **14,** 15625–15636. ISSN: 14639076 (2012).

55. Keyser, U. F., van der Does, J., Dekker, C. & Dekker, N. H. Optical tweezers for force measurements on DNA in nanopores. *Review of Scientific Instruments* **77,** 105105. ISSN: 00346748. http://scitation.aip.org/content/aip/journal/rsi/77/10/10.1063/1.2358705 (2006).

56. Neves, A. A. R. *et al.* Rotational dynamics of optically trapped nanofibers. *Optics Express* **18,** 822 (2010).

57. Carter, A. R., King, G. M. & Perkins, T. T. Back-scattered detection provides atomic-scale localization precision, stability, and registration in 3D. *Optics Express* **15,** 13434 (2007).

58. Shivashankar, G. V., G. Stolovitzky & A. Libchaber. Backscattering from a tethered bead as a probe of DNA flexibility. *Applied Physics Letters* **73,** 291–293. ISSN: 0003-6951 (1998).

59. Sischka, A. *et al.* Single beam optical tweezers setup with backscattered light detection for three-dimensional measurements on DNA and nanopores. *Review of Scientific Instruments* **79,** 063702. ISSN: 00346748. http://scitation.aip.org/content/aip/journal/rsi/79/6/10.1063/1.2938401 (2008).

60. Shipley, F. B. & Carter, A. R. Back-scattered detection yields viable signals in many conditions. *Optics express* **20,** 9581–90. ISSN: 1094-4087. http://www.ncbi.nlm.nih.gov/pubmed/22535050 (2012).

61. Ramaiya, A., Roy, B., Bugiel, M. & Schäffer, E. Kinesin rotates unidirectionally and generates torque while walking on microtubules. *Proceedings of the National Academy of Sciences* **114,** 10894–10899. ISSN: 0027-8424 (2017).

62. Wohland, T., Rosin, A. & Stelzer, E. Theoretical determination of the influence of the polarization on forces exerted by optical tweezers. *Optik 102,* 181–190 (1996).

63. Gu, M., Morrish, D. & Ke, P. C. Enhancement of transverse trapping efficiency for a metallic particle using an obstructed laser beam. *Applied Physics Letters* **77,** 34–36. ISSN: 00036951 (2000).

64. Ghislain, L. P. & Webb, W. W. Scanning-force microscope based on an optical trap. *Optics Letters* **18,** 1678. ISSN: 0146-9592 (1993).

65. Berg-Sørensen, K. & Flyvbjerg, H. Power spectrum analysis for optical tweezers. *Review of Scientific Instruments* **75,** 594–612. ISSN: 00346748 (2004).

66. Norrelykke, S. F. *et al.* Calibration of optical tweezers with positional detection in the back focal plane. *Review of Scientific Instruments* **77.** ISSN: 00346748. arXiv: 0603037 [physics] (2006).

67. Faxen, H. The resistance against the movement of a rigour sphere in viscous fluids, which is embedded between two parallel layered barriers. *Annalen der Physik* **68,** 89–119 (1922).

68. Schäffer, E., Nørrelykke, S. F. & Howard, J. Surface forces and drag coefficients of microspheres near a plane surface measured with optical tweezers. *Langmuir* **23,** 3654–3665. ISSN: 07437463 (2007).

69. Simmert, S. & Jachowski, T. *pyotic - calibrate optical tweezers by power spectral density analysis and efficiantly analyze time-depended siganls* 2019. https://github.com/cellular-nanoscience/pyotic.

70. Hobbs, P. C. D. *Building Electro-Optical Systems* 0–471. ISBN: 0471246816 (2009).

71. Vanderwerf, D. F. *Applied Prismatic and Reflective Optics* ISBN: 978-0-8194-8332-4 (2010).

72. Fällman, E. & Axner, O. Design for fully steerable dual-trap optical tweezers. *Applied Optics* **36,** 2107. ISSN: 0003-6935 (1997).

73. Goncalves, C. M. B., Coutinho, J. A. P. & Marrucho, I. M. Optical properties of polylactic acid. *Poly(lactic acid): Synthesis, Structures, Properties, Processing, and Applications,* 97–113 (2010).

74. Gibson, G. M., Leach, J., Keen, S., Wright, A. J. & Padgett, M. J. Measuring the accuracy of particle position and force in optical tweezers using high-speed video microscopy. *Optics Express* **16,** 14561 (2008).

75. Czerwinski, F., Richardson, A. C. & Oddershede, L. B. Quantifying Noise in Optical Tweezers by Allan Variance. *Optics Express* **17,** 13255 (2009).

76. Edelstein, A., Amodaj, N., Hoover, K., Vale, R. & Stuurman, N. Computer control of microscopes using manager. *Current Protocols in Molecular Biology.* ISSN: 19343639 (2010).

77. Bormuth, V., Howard, J. & Schäffer, E. LED illumination for video-enhanced DIC imaging of single microtubules. *Journal of Microscopy* **226,** 1–5. ISSN: 00222720 (2007).

78. Zernike, F. How I Discovered Phase Contrast. *Science* **Vol. 121,** pp. 345–349 (1955).

79. Fedosov, I. Particle image velocimetry for visualizing laser-induced motion of nanoparticles. *SPIE Newsroom,* 8–10 (2007).

80. Mahamdeh, M., Simmert, S., Luchniak, A., Schäffer, E. & Howard, J. Label-free high-speed wide-field imaging of single microtubules using interference reflection microscopy. *Journal of Microscopy* **272,** 60–66. ISSN: 13652818 (2018).

81. Duhr, S., Arduini, S. & Braun, D. Thermophoresis of DNA determined by microfluidic fluorescence. *European Physical Journal E* **15,** 277–286. ISSN: 12928941 (2004).

82. Duhr, S. & Braun, D. Thermophoretic depletion follows boltzmann distribution. *Physical Review Letters* **96,** 168301. ISSN: 00319007. http://link.aps.org/doi/10.1103/PhysRevLett.96.168301 (2006).

83. Seidel, S. a. I. *et al.* Label-Free Microscale Thermophoresis Discriminates Sites and Affinity of Protein-Ligand Binding. *Angewandte Chemie International Edition* **51,** 10656–10659. ISSN: 14337851. http://doi.wiley.com/10.1002/anie.201204268 (2012).

84. Reichl, M. R. & Braun, D. Thermophoretic manipulation of molecules inside living cells. *Journal of the American Chemical Society* **136,** 15955–15960. ISSN: 1520-5126. http://dx.doi.org/10.1021/ja506169b (2014).

85. Burmeister, M. Study of a Heating Laser Profile Using Fluorophores as Temperature Sensors Moritz Burmeister (2015).

86. Committee, C. & Board, I.-s. S. *IEEE Standard Definitions of Physical Quantities for Fundamental Frequency and Time Metrology – Random Instabilities* 45. ISBN: 0738117536. http://ieeexplore.ieee.org/servlet/opac?punumber=6545{\%}5Cnhttp://linkinghub.elsevier.com/retrieve/pii/S0920548999922729 (2008).

87. Mahamdeh, M. & Schäffer, E. Optical tweezers with millikelvin precision of temperature-controlled objectives and base-pair resolution. *Optics Express* **17,** 17190 (2009).

88. Ziegler, B. J. G. & Rochester, N. B. N. Optimum Settings for Automatic Controllers (Ziegler and Nichols, 1942) (1942).

89. Tagaya, A. Birefringence of Polymer. *Encyclopedia of Polymeric Nanomaterials,* 1–6 (2013).

90. Paterson, L. *et al.* Controlled rotation of optically trapped microscopic particles. *Science* **292,** 912–914. ISSN: 00368075 (2001).

91. Gollnick, B. *Thesis:Optical and Magnetic Tweezers for Applications in Single-Molecule Biophysics and Nanotechnology* PhD thesis (2014).

92. Gell, C., Berndt, M., Enderlein, J. & Diez, S. TIRF microscopy evanescent field calibration using tilted fluorescent microtubules. *Journal of Microscopy* **234,** 38–46. ISSN: 00222720 (2009).

93. Hochmuth, R. M., Mohandas, N. & Blackshear, P. L. Measurement of the Elastic Modulus for Red Cell Membrane Using a Fluid Mechanical Technique. *Biophysical Journal* **13,** 747–762. ISSN: 00063495. http://dx.doi.org/10.1016/S0006-3495(73)86021-7 (1973).

94. Terasaki, M., Bo Chen, L. & Fujiwara, K. Microtubules and the endoplasmic reticulum are highly interdependent structures. *Journal of Cell Biology* **103,** 1557–1568. ISSN: 0021-9525 (1986).

95. Vale, R. D. & Hotani, H. Formation of membrane networks in vitro by kinesin-driven microtubule movement. *The Journal of Cell Biology* **107,** 2233–2241. ISSN: 0021-9525 (2004).

96. Dabora, S. L. & Sheetz, M. F. The microtubule-dependent formation of a tubulovesicular network with characteristics of the ER from cultured cell extracts. *Cell* **54,** 27–35. ISSN: 00928674 (1988).

97. Roux, A. *et al.* Tubulation-By-Molecular-Motors-Pnas-02, 6. papers2://publication/uuid/F8654B51-46F2-403F-B0FB-CE50B87B466B (2002).

98. Koster, G., VanDuijn, M., Hofs, B. & Dogterom, M. Membrane tube formation from giant vesicles by dynamic association of motor proteins. *Proceedings of the National Academy of Sciences* **100,** 15583–15588. ISSN: 0027-8424. http://www.pnas.org/cgi/doi/10.1073/pnas.2531786100 (2003).

99. Waugh, R. E. Surface viscosity measurements from large bilayer vesicle tether formation. I. Analysis. *Biophysical Journal* **38,** 19–27. ISSN: 00063495. http://dx.doi.org/10.1016/S0006-3495(82)84527-X (1982).

100. Sun, M. *et al.* Multiple membrane tethers probed by atomic force microscopy. *Biophysical Journal* **89,** 4320–4329. ISSN: 00063495 (2005).

101. Afrin, R. & Ikai, A. Force profiles of protein pulling with or without cytoskeletal links studied by AFM. *Biochemical and Biophysical Research Communications* **348,** 238–244. ISSN: 0006291X (2006).

102. Kocun, M. & Janshoff, A. Pulling tethers from pore-spanning bilayers: Towards simultaneous determination of local bending modulus and lateral tension of membranes. *Small* **8,** 847–851. ISSN: 16136810 (2012).

103. Hosu, B. G., Sun, M., Marga, F., Grandbois, M. & Forgacs, G. Eukaryotic membrane tethers revisited using magnetic tweezers. *Physical Biology* **4,** 67–78. ISSN: 14783975 (2007).

104. Stark, D. J., Killian, T. C. & Raphael, R. M. A microfabricated magnetic force transducer-microaspiration system for studying membrane mechanics. *Physical Biology* **8.** ISSN: 14783967 (2011).

105. Campillo, C. *et al.* Unexpected membrane dynamics unveiled by membrane nanotube extrusion. *Biophysical Journal* **104,** 1248–1256. ISSN: 15420086 (2013).

106. Aimon, S. *et al.* Membrane Shape Modulates Transmembrane Protein Distribution. *Developmental Cell* **28,** 212–218. ISSN: 15345807. arXiv: NIHMS150003. http://dx.doi.org/10.1016/j.devcel.2013.12.012 (2014).

107. Saleem, M. *et al.* A balance between membrane elasticity and polymerization energy sets the shape of spherical clathrin coats. *Nature Communications* **6.** ISSN: 20411723 (2015).

108. Simunovic, M. *et al.* Friction Mediates Scission of Tubular Membranes Scaffolded by BAR Proteins. *Cell* **170,** 172–184.e11. ISSN: 10974172 (2017).

109. Schöneberg, J. *et al.* ATP-dependent force generation and membrane scission by ESCRT-III and Vps4. *Science (New York, N.Y.)* **362,** 1423–1428. ISSN: 1095-9203. http://www.ncbi.nlm.nih.gov/pubmed/30573630{\%}0Ahttp://www.pubmedcentral.nih.gov/articlerender.fcgi?artid=PMC6309985 (2018).

110. De Franceschi, N. *et al.* The ESCRT protein CHMP2B acts as a diffusion barrier on reconstituted membrane necks. *Journal of Cell Science* **132.** ISSN: 14779137 (2019).

111. Dai, J. & Sheetz, M. P. Mechanical properties of neuronal growth cone membranes studied by tether formation with laser optical tweezers. *Biophysical Journal* **68,** 988–996. ISSN: 00063495. http://dx.doi.org/10.1016/S0006-3495(95)80274-2 (1995).

112. Dai, J. & Sheetz, M. P. Membrane tether formation from blebbing cells. *Biophysical Journal* **77,** 3363–3370. ISSN: 00063495. http://dx.doi.org/10.1016/S0006-3495(99)77168-7 (1999).

113. Hochmuth, R. M., Shao, J.-Y., Dai, J. & Sheetz, M. P. Deformation and Flow of Membrane into Tethers Extracted from Neuronal Growth Cones. *Biophysical Journal* **70,** 358–369. ISSN: 00063495 (1996).

114. Waugh, R. E. & Bauserman, R. G. Physical measurements of bilayer-skeletal separation forces. *Annals of Biomedical Engineering* **23,** 308–321. ISSN: 00906964 (1995).

115. Sheetz, M. P. Cell control by membrane-cytoskeleton adhesion. *Nature Reviews Molecular Cell Biology* **2,** 392–396. ISSN: 14710072 (2001).

116. Evans, E. & Yeung, A. Hidden dynamics in rapid changes of bilayer shape. *Chemistry and Physics of Lipids* **73,** 39–56. ISSN: 00093084 (1994).

117. Svetina, S., Žekš, B., Waugh, R. E. & Raphael, R. M. Theoretical analysis of the effect of the transbilayer movement of phospholipid molecules on the dynamic behavior of a microtube pulled out of an aspirated vesicle. *European Biophysics Journal* **27,** 197–209. ISSN: 01757571 (1998).

118. Heinrich, V., Božič, B., Svetina, S. & Žekš, B. Vesicle deformation by an axial load: From elongated shapes to tethered vesicles. *Biophysical Journal* **76,** 2056–2071. ISSN: 00063495 (1999).

119. Powers, T. R., Huber, G. & Goldstein, R. E. Fluid-membrane tethers: Minimal surfaces and elastic boundary layers. *Physical Review E - Statistical Physics, Plasmas, Fluids, and Related Interdisciplinary Topics* **65,** 11. ISSN: 1063651X (2002).

120. Derényi, I., Jülicher, F. & Prost, J. Formation and Interaction of Membrane Tubes. *Physical Review Letters* **88,** 238101. ISSN: 0031-9007. arXiv: 0205630 [cond-mat]. http://link.aps.org/doi/10.1103/PhysRevLett.88.238101 (2002).

121. Cuvelier, D., Derényi, I., Bassereau, P. & Nassoy, P. Coalescence of membrane tethers: experiments, theory, and applications. *Biophysical journal* **88,** 2714–26. ISSN: 0006-3495. http://www.pubmedcentral.nih.gov/articlerender.fcgi?artid=1305367{\&}tool=pmcentrez{\&}rendertype=abstract (2005).

122. Helfrich, W. *Elastic Properties of Lipid Bilayers: Theory and PossibleExperiments* 1973.

123. Deuling, H. & Helfrich, W. The curvature elasticity of fluid membranes : A catalogue of vesicle shapes. *Journal de Physique* **37,** 1335–1345. ISSN: 0302-0738. http://www.edpsciences.org/10.1051/jphys:0197600370110133500 (1976).

124. Jan Bukman, D., Hua Yao, J. & Wortis, M. Stability of cylindrical vesicles under axial tension. *Physical Review E* **54,** 5463–5468. ISSN: 1063-651X (1996).

125. Diz-Muñoz, A., Fletcher, D. A. & Weiner, O. D. Use the force: Membrane tension as an organizer of cell shape and motility. *Trends in Cell Biology* **23,** 47–53. ISSN: 09628924. arXiv: NIHMS150003 (2013).

126. Bugiel, M. *et al.* Versatile microsphere attachment of GFP-labeled motors and other tagged proteins with preserved functionality. *Journal of Biological Methods* **2,** 30. ISSN: 2326-9901. http://www.jbmethods.org/jbm/article/view/79 (2015).

127. Ander, M. *Clamping DNA strands : Nano-Mechanics of Homologous Recombination An optical tweezers study of the DNA single-strand annealing mechanism zur Erlangung des akademischen Grades Diplom-Biochemiker* PhD thesis (2011), 119.

128. Angelova, M. I., Soléau, S., Méléard, P., Faucon, F. & Bothorel, P. Preparation of giant vesicles by external AC electric fields. Kinetics and applications. *Trends in Colloid and Interface Science VI* **131,** 127–131. ISSN: 0340255X. http://www.springerlink.com/index/10.1007/BFb0116295 (1992).

129. García-Sáez, A. J., Ries, J., Orzáez, M., Pérez-Payà, E. & Schwille, P. Membrane promotes tBID interaction with BCL XL. *Nature Structural and Molecular Biology* **16,** 1178–1185. ISSN: 15459993. http://dx.doi.org/10.1038/nsmb.1671 (2009).

130. Aitken, C. E., Marshall, R. A. & Puglisi, J. D. An oxygen scavenging system for improvement of dye stability in single-molecule fluorescence experiments. *Biophysical Journal* **94,** 1826–1835. ISSN: 15420086 (2008).

131. Ugarte-Uribe, B., Müller, H. M., Otsuki, M., Nickel, W. & García-Sáez, A. J. Dynamin-related protein 1 (Drp1) promotes structural intermediates of membrane division. *Journal of Biological Chemistry* **289,** 30645–30656. ISSN: 1083351X (2014).

132. Unsay, J. D., Cosentino, K. & García-Sáez, A. J. Atomic Force Microscopy Imaging and Force Spectroscopy of Supported Lipid Bilayers. *Journal of Visualized Experiments,* 1–9 (2015).

133. Hisette, M.-L., Haddad, P., Gisler, T., Marques, C. M. & Schröder, A. P. Spreading of bio-adhesive vesicles on DNA carpets. *Soft Matter* **4,** 828. ISSN: 1744-683X. http://xlink.rsc.org/?DOI=b715530a (2008).

134. Girard, P. *et al.* A new method for the reconstitution of membrane proteins into giant unilamellar vesicles. *Biophysical Journal* **87,** 419–429. ISSN: 00063495 (2004).

135. Dar, S., Kamerkar, S. C. & Pucadyil, T. J. A high-throughput platform for real-time analysis of membrane fission reactions reveals dynamin function. *Nature Cell Biology* **17,** 1588–1596. ISSN: 14764679 (2015).

136. Dar, S., Kamerkar, S. C. & Pucadyil, T. J. Use of the supported membrane tube assay system for real-time analysis of membrane fission reactions. *Nature Protocols* **12,** 390–400. ISSN: 17502799. http://dx.doi.org/10.1038/nprot.2016.173 (2017).

137. Kamal, M. M., Mills, D., Grzybek, M. & Howard, J. Measurement of the membrane curvature preference of phospholipids reveals only weak coupling between lipid shape and leaflet curvature. *Proceedings of the National Academy of Sciences* **106,** 22245–22250. ISSN: 0027-8424 (2009).

138. Dimova, R. Recent developments in the field of bending rigidity measurements on membranes. *Advances in Colloid and Interface Science* **208,** 225–234. ISSN: 00018686. http://dx.doi.org/10.1016/j.cis.2014.03.003 (2014).

139. Niggemann, G., Kummrow, M. & Helfrich, W. The Bending Rigidity of Phosphatidylcholine Bilayers: Dependences on Experimental Method, Sample Cell Sealing and Temperature. *Journal de Physique II* **5,** 413–425. ISSN: 1155-4312 (1995).

140. Pan, J., Tristram-Nagle, S., Kučerka, N. & Nagle, J. F. Temperature dependence of structure, bending rigidity, and bilayer interactions of dioleoylphosphatidylcholine bilayers. *Biophysical Journal* **94,** 117–124. ISSN: 00063495. http://dx.doi.org/10.1529/biophysj.107.115691 (2008).

141. Kubin, R. & Fletcher, A. Fluorescence quantum yields of some rhodamine dyes. *Journal of Luminescence* **27,** 455–462. ISSN: 0022-2313 (1982).

142. Koster, G., Cacciuto, A., Derényi, I., Frenkel, D. & Dogterom, M. Force barriers for membrane tube formation. *Physical Review Letters* **94,** 16–19. ISSN: 00319007 (2005).

143. Rawicz, W., Olbrich, K. C., McIntosh, T., Needham, D. & Evans, E. A. Effect of chain length and unsaturation on elasticity of lipid bilayers. *Biophysical Journal* **79,** 328–339. ISSN: 00063495. http://dx.doi.org/10.1016/S0006-3495(00)76295-3 (2000).

144. Overington, J. P., Al-Lazikani, B. & Hopkins, A. L. How many drug targets are there ? PubMed Commons. *Nature reviews. Drug discovery* **5,** 10. http://www.ncbi.nlm.nih.gov/pubmed/17139284{\%}0Ahttp://dx.doi.org/10.1038/nrd2199 (2006).

145. Jørgensen, I. L., Kemmer, G. C. & Pomorski, T. G. Membrane protein reconstitution into giant unilamellar vesicles: a review on current techniques. *European Biophysics Journal* **46,** 103–119. ISSN: 14321017 (2017).

146. Schmid, E. M., Richmond, D. L. & Fletcher, D. A. *Reconstitution of proteins on electroformed giant unilamellar vesicles* 319–338. ISBN: 9780128024508. http://dx.doi.org/10.1016/bs.mcb.2015.02.004 (Elsevier Ltd, 2015).

147. Quemeneur, F. *et al.* Shape matters in protein mobility within membranes. *Proceedings of the National Academy of Sciences* **111,** 5083–5087. ISSN: 0027-8424. arXiv: arXiv:1408.1149 (2014).

148. Okano, T., Inoue, K., Koseki, K. & Suzuki, H. Deformation Modes of Giant Unilamellar Vesicles Encapsulating Biopolymers. *ACS Synthetic Biology* **7,** 739–747. ISSN: 21615063 (2018).

149. Glazier, R. & Salaita, K. Supported lipid bilayer platforms to probe cell mechanobiology. *Biochimica et Biophysica Acta - Biomembranes* **1859,** 1465–1482. ISSN: 18792642. http://dx.doi.org/10.1016/j.bbamem.2017.05.005 (2017).

150. Chang, C. C., Edwald, E., Veatch, S., Steel, D. G. & Gafni, A. Interactions of amyloid-β peptides on lipid bilayer studied by single molecule imaging and tracking. *Biochimica et Biophysica Acta - Biomembranes* **1860,** 1616–1624. ISSN: 18792642. https://doi.org/10.1016/j.bbamem.2018.03.017 (2018).

151. Saxton, M. J. & Jacobson, K. Single-particle tracking: Applications to membrane dynamics. *Annual Review of Biophysics and Biomolecular Structure* **26,** 373–399. ISSN: 10568700 (1997).

152. Cui, Y. *et al.* Single-Particle Tracking for the Quantification of Membrane Protein Dynamics in Living Plant Cells. *Molecular Plant* **11,** 1315–1327. ISSN: 17529867. https://doi.org/10.1016/j.molp.2018.09.008 (2018).

153. Bridges, A. A. & Gladfelter, A. S. *In vitro reconstitution of septin assemblies on supported lipid bilayers* 57–71. http://dx.doi.org/10.1016/bs.mcb.2016.03.025 (Elsevier Ltd, 2016).

154. Osman, C., Voelker, D. R. & Langer, T. Making heads or tails of phospholipids in mitochondria. *Journal of Cell Biology* **192,** 7–16. ISSN: 00219525 (2011).

155. Glancy, B. & Balaban, R. S. Role of mitochondrial Ca 2+ in the regulation of cellular energetics. *Biochemistry* **51,** 2959–2973. ISSN: 00062960 (2012).

156. Friedman, J. R. & Nunnari, J. Mitochondrial form and function. *Nature* **505,** 335–343. ISSN: 00280836 (2014).

157. Okamoto, K. & Shaw, J. M. Mitochondrial Morphology and Dynamics in Yeast and Multicellular Eukaryotes. *Annual Review of Genetics* **39,** 503–536. ISSN: 0066-4197 (2005).

158. Youle, R. J. *et al.* Mitochondrial Fission, Fusion, and Stress. **337,** 1062–1066 (2012).

159. Chen, H. & Chan, D. C. Mitochondrial dynamics-fusion, fission, movement, and mitophagy-in neurodegenerative diseases. *Human Molecular Genetics* **18,** 169–176. ISSN: 09646906 (2009).

160. Wilson, T. J., Slupe, A. M. & Strack, S. Cell signaling and mitochondrial dynamics: Implications for neuronal function and neurodegenerative disease. *Neurobiology of Disease* **51,** 13–26. ISSN: 09699961. http://dx.doi.org/10.1016/j.nbd.2012.01.009 (2013).

161. Zorzano, A. & Claret, M. Implications of mitochondrial dynamics on neurodegeneration and on hypothalamic dysfunction. *Frontiers in Aging Neuroscience* **7,** 1–17. ISSN: 16634365 (2015).

162. Brandon, E. *et al.* On and Off Membrane Dynamics of the Endoplasmic. *Molecular Biology of the Cell* **17,** 2996 –3008 (2006).

163. Gandre-Babbe, S. & Alexander M., v. d. B. The Novel Tail-anchored Membrane Protein Mff Controls Mitochondrial and Peroxisomal Fission in Mammalian Cells. *Molecular biology of the cell* **19,** 308–317 (2008).

164. Palmer, C. S. *et al.* MiD49 and MiD51, new components of the mitochondrial fission machinery. *EMBO Reports* **12,** 565–573. ISSN: 1469221X. http://dx.doi.org/10.1038/embor.2011.54 (2011).

165. Zhao, J. *et al.* Human MIEF1 recruits Drp1 to mitochondrial outer membranes and promotes mitochondrial fusion rather than fission. *EMBO Journal* **30,** 2762–2778. ISSN: 02614189 (2011).

166. Losó n, O. C., Song, Z., Chen, H. & Chan, D. C. Fis1, Mff, MiD49, and MiD51 mediate Drp1 recruitment in mitochondrial fission. *Molecular Biology of the Cell* **24,** 659–667. ISSN: 10591524 (2013).

167. Kraus, F. & Ryan, M. T. The constriction and scission machineries involved in mitochondrial fission. *Journal of Cell Science* **130,** 2953–2960. ISSN: 14779137 (2017).

168. Bui, H. T. & Shaw, J. M. Dynamin assembly strategies and adaptor proteins in mitochondrial fission. *Current Biology* **23,** R891–R899. ISSN: 09609822. http://dx.doi.org/10.1016/j.cub.2013.08.040 (2013).

169. Macdonald, P. J. *et al.* Distinct splice variants of dynamin-related protein 1 differentially utilize mitochondrial fission factor as an effector of cooperative GTPase activity. *Journal of Biological Chemistry* **291,** 493–507. ISSN: 1083351X (2016).

170. Michalska, B., Duszyński, J. & Szymański, J. Mechanism of mitochondrial fission - structure and function of Drp1 protein. *Postepy biochemii* **62,** 127–137. ISSN: 00325422 (2016).

171. Faelber, K. *et al.* Crystal structure of nucleotide-free dynamin. *Nature* **477,** 556–562. ISSN: 00280836 (2011).

172. Fröhlich, C. *et al.* Structural insights into oligomerization and mitochondrial remodelling of dynamin 1-like protein. *The EMBO journal* **32,** 1280–92. ISSN: 1460-2075. http://www.pubmedcentral.nih.gov/articlerender.fcgi?artid=3642683{\&}tool=pmcentrez{\&}rendertype=abstract (2013).

173. Gao, S. *et al.* Structural basis of oligomerization in the stalk region of dynamin-like MxA. *Nature* **465,** 502–506. ISSN: 00280836. http://dx.doi.org/10.1038/nature08972 (2010).

174. Francy, C. A., Alvarez, F. J. D., Mears, J. A., Ramachandran, R. & Zhou, L. The Mechanoenzymatic Core of Dynamin-related Protein 1 Comprises the Minimal Machinery Required for Membrane Constriction. *Journal of Biological Chemistry* **290,** 11692–11703. ISSN: 0021-9258 (2015).

175. Francy, C. A., Clinton, W. R., Fröhlich, C., Murphy, C. & Mears, J. A. Cryo-EM Studies of Drp1 Reveal Cardiolipin Interactions that Activate the Helical Oligomer. *Scientific Reports* **7.** ISSN: 20452322 (2017).

176. Strack, S., Wilson, T. J. & Cribbs, J. T. Cyclin-dependent kinases regulate splice-specific targeting of dynamin-related protein 1 to microtubules. *Journal of Cell Biology* **201,** 1037–1051. ISSN: 00219525 (2013).

177. Lakämper, S. & Meyhöfer, E. The E-hook of tubulin interacts with kinesin's head to increase processivity and speed. *Biophysical Journal* **89,** 3223–3234. ISSN: 00063495 (2005).

178. Dudek, S. M. *et al.* SPG20 Protein Spartin Is Recruited to Midbodies by ESCRT-III Protein Ist1 and Participates in Cytokinesis. *Molecular biology of the cell* **21,** 4042–4056. ISSN: 1939-4586 (2010).

179. Roux, A. *et al.* Membrane curvature controls dynamin polymerization. *Proceedings of the National Academy of Sciences of the United States of America* **107,** 4141–4146. ISSN: 0027-8424. arXiv: arXiv:1408.1149 (2010).

180. Liu, Y. W. *et al.* Differential curvature sensing and generating activities of dynamin isoforms provide opportunities for tissue-specific regulation. *Proceedings of the National Academy of Sciences of the United States of America* **108.** ISSN: 00278424 (2011).

181. Michalska, B. M. *et al.* Insight into the fission mechanism by quantitative characterization of Drp1 protein distribution in the living cell. *Scientific Reports* **8,** 1–15. ISSN: 20452322 (2018).

182. Kamerkar, S. C., Kraus, F., Sharpe, A. J., Pucadyil, T. J. & Ryan, M. T. Dynamin-related protein 1 has membrane constricting and severing abilities sufficient for mitochondrial and peroxisomal fission. *Nature Communications* **9,** 1–15. ISSN: 20411723. http://dx.doi.org/10.1038/s41467-018-07543-w (2018).

183. Gell, C. *et al. Microtubule dynamics reconstituted in vitro and imaged by single-molecule fluorescence microscopy* First edit. **C,** 221–245. ISBN: 9780123748157. http://dx.doi.org/10.1016/S0091-679X(10)95013-9 (Elsevier, 2010).

184. Tsekouras, K., Custer, T. C., Jashnsaz, H., Walter, N. G. & Pressé, S. A novel method to accurately locate and count large numbers of steps by photobleaching. *Molecular Biology of the Cell* **27,** 3601–3615. ISSN: 19394586 (2016).

185. Xu, J. *et al.* Automated Stoichiometry Analysis of Single-Molecule Fluorescence Imaging Traces via Deep Learning. *Journal of the American Chemical Society* **141,** 6976–6985. ISSN: 15205126 (2019).

186. Jachowski, T. *Stepfinder: find steps in data with low SNR* 2019. https://github.com/tobiasjj/stepfinder.

187. Allan, D., B T., C., N. C., K. & van der We, C. M. *Trackpy v0.4.1* 2018.

188. Domanov, Y. A. *et al.* Mobility in geometrically confined membranes. *Proceedings of the National Academy of Sciences.* ISSN: 0027-8424 (2011).

189. Savin, T. & Doyle, P. S. Static and dynamic errors in particle tracking microrheology. *Biophysical Journal* **88,** 623–638. ISSN: 00063495. http://dx.doi.org/10.1529/biophysj.104.042457 (2005).

190. Wilson, B. A., Ramanathan, A. & Lopez, C. F. Cardiolipin-Dependent Properties of Model Mitochondrial Membranes from Molecular Simulations. *Biophysical Journal* **117,** 429–444. ISSN: 00063495. https://doi.org/10.1016/j.bpj.2019.06.023 (2019).

191. Cicuta, P., Keller, S. L. & Veatch, S. L. Diffusion of liquid domains in lipid bilayer membranes. *Journal of Physical Chemistry B* **111,** 3328–3331. ISSN: 15206106 (2007).

192. Petrov, E. P. & Schwille, P. Translational diffusion in lipid membranes beyond the Saffman-Delbrück approximation. *Biophysical Journal* **94,** 41–43. ISSN: 15420086 (2008).

193. Saffman, P. G. & Delbruck, M. Brownian motion in. *Proc Natl Acad Sci USA* **72,** 3111–3113 (1975).

194. Daniels, D. R. & Turner, M. S. Diffusion on membrane tubes: A highly discriminatory test of the Saffman-Delbruck theory. *Langmuir* **23,** 6667–6670. ISSN: 07437463 (2007).

195. Hachiya, T., Terashima, I. & Noguchi, K. Increase in respiratory cost at high growth temperature is attributed to high protein turnover cost in Petunia x hybrida petals. *Plant, Cell and Environment* **30,** 1269–1283. ISSN: 01407791 (2007).

196. Howard, J. *Mechnnics and Proteins Motor the Cytoskeleton* (Sinauer Associates,Inc., Sunderland, Massachuset, 2001).

197. Sorice, M. *et al.* Cardiolipin-enriched raft-like microdomains are essential activating platforms for apoptotic signals on mitochondria. *FEBS Letters* **583,** 2447–2450. ISSN: 00145793. http://dx.doi.org/10.1016/j.febslet.2009.07.018 (2009).

198. Bustillo-Zabalbeitia, I. *et al.* Specific interaction with cardiolipin triggers functional activation of dynamin-related protein 1. *PLoS ONE* **9.** ISSN: 19326203 (2014).

199. Strack, S. & Cribbs, J. T. Allosteric modulation of Drp1 mechanoenzyme assembly and mitochondrial fission by the variable domain. *Journal of Biological Chemistry* **287,** 10990–11001. ISSN: 00219258 (2012).

200. Ortega Arroyo, J. *et al.* Label-free, all-optical detection, imaging, and tracking of a single protein. *Nano Letters* **14,** 2065–2070. ISSN: 15306992 (2014).

201. Walczak, C. E. & Shaw, S. L. A MAP for bundling microtubules. *Cell* **142,** 364–367. ISSN: 00928674 (2010).

202. Trushko, A., Schäffer, E. & Howard, J. The growth speed of microtubules with XMAP215-coated beads coupled to their ends is increased by tensile force. *Proceedings of the National Academy of Sciences of the United States of America* **110,** 14670–14675. ISSN: 10916490 (2013).

203. Renner, L. D. & Weibel, D. B. Cardiolipin microdomains localize to negatively curved regions of Escherichia coli membranes. *Proceedings of the National Academy of Sciences of the United States of America* **108,** 6264–6269. ISSN: 10916490 (2011).

204. Lei, M. *et al.* Long-Distance Axial Trapping with Focused Annular Laser Beams. *PLoS ONE* **8,** 3–8. ISSN: 19326203 (2013).

205. Akturk, S., Zhou, B., Pasquiou, B., Franco, M. & Mysyrowicz, A. Intensity distribution around the focal regions of real axicons. *Optics Communications* **281,** 4240–4244. ISSN: 00304018 (2008).

Acknowledgments

Thank you Erik for the freedom during the project. I see my self now truly as one of the so called builders or system architects of your group. Having the chance to build one these instrument by myself was terrifying, exciting, a burden, fun, sometimes literally electrifying, challenging, easy and the most complicated thing I have done, so far. Building a instrument and developing a biophysical assay felt sometimes too much for one person to do, but this has been exactly what I wanted. It has been a great opportunity to grow professionally and personally.
Thank you Ana Garcia and Wolfram Antonin for productive meetings and discussion. My work benefited from your input and critical comments. Thank you, Sarah and Dagmar, both put a lot of effort into courses at the MPI, which taught me a lot of scientific soft skills. I would also thank the IMPRS Tübingen, which accepted me for the program and the funding for the very great EMBO conference in Corsica, retreats and the whole framework of the graduate school.
Central Facilities, especially Edgar and Mark for excellent support. I want to thank you a lot, Bego, for long-term collaboration. You showed me everything I know about DRP1 and also provided the protein sample to actually do experiments. Shilpa for the fun side project on staph with smfish and schnitzel. Tassula and Katharina for the very efficient pip/guv/wipi collaboration. Thanks Steve, for chilli, scripts, beer, programs and pizza in the basement. And also teaching me some science things. Thanks Tobi, for all the optimized LabView vi's, python scripts, SLB testing. You thought me what a reasonable level of perfection actually is, and what not. More importantly, now that I am gone through two terrabyte of data, I really can appreciate your efforts in the pyotic investigator. Thank you Avin and Suman, for teaching me how to cook indian food properly. For discussion about Gordon Ramsey and being a awesome fellow thank you Mayank. Thanks to Mehrbod for jokes about Mohammad in Farsi and Mohammad for Farsi jokes about Mehrbod. I had no clue that you know so much about sand, safran, camels and rosewater. Thank you Micha, for the always absolute precise StarTek quotes, wine, politics and proof reading parts of my thesis. Maria thank you for the boxes, very much. I thank colleges on the floor I forgot to mention here that helped me in some way or another. Thank you Moritz, for being the best first student to be supervised by me, awesome drummer and terrible dice game player. And Kevin, for very long and sometimes just entertaining discussions about neuronal networks and annoying old matlab scripts. I am not sure if I remember correctly which students I supervised in some way or another Sven, Baschdi, Aron, Katrin, Carolin,

Rene, Friedrich, Jonas and the lab members Anita, Frau Christine Kiefer, Ben, Victoria, Swathi, all of you made me a better teacher. I thank my family for sometimes useful, sometimes reasonable comments and their full support along the road.

I want to thank Lena and Julius for everything to keep me going.

A. Materials List

A.1. Buffers and Chemicals

This section lists all buffers used to perform the mentioned experiments.

- GTPase buffer/Chemicals
  - 20mM Hepes/KOH pH 7.4, MW = 238.3012 g/mol
  - 150mM Kcl, MW = 74.5513 g/mol
  - 1mM MgCl2, MW = 95.211 g/mol
- PEM - old name BRB80
  - 80 mM PIPES, Sigma, cat P6757, Biochemika Ultra 99.5%, MW = 302.37 g/mol
  - 1 mM MgCl2, Merck / VWR, cat 1.05833.1000, MW = 230.3 g/mol (for Magnesiumchlorid Hexahydrat)
  - 1 mM EGTA, (Ethylene glycol-bis (2-aminoethylether)-N,N,N',N'-Tetra acetic acid), Sigma, cat E4378, MW = 380.35 g/mol
  - 100 mM KOH, Merck / VWR, cat 1.05033.1000, MW = 56.11 g/mol
- PBS
  - 137 mM, NaCl
  - 2.7 mM, KCl
  - 8 mM, KH2PO4
  - 1.5 mM, Na2HPO4
- SLB buffer
  - 10 mM HEPES,
  - 150 mM NaCl,
  - 3mM NaN3
- PolyLink Protein Coupling Kit, Catalog No.24350-1
- NT buffer 10x, pH 7.3 with HCl
  - 100 mM NaCl

  - 200 mM Tris
- NTT
  - 1xNT
  - Tween 10%
- NTT10BSA, for blocking
  - NTT+10mg/ml BSA
- Anti bleaching buffer
  - D-Glucose 10mM
  - Glucose oxidase 112.5 mM
  - Catalase 0.02 mg/ml
- ascorbic acid 20mM, Vitamine C, (+)-Sodium L-ascorbate, crystaline, Lot: SLBT6741
- glucose
- sucrose
- mucasol
- technical ethanol
- chloroform

A.2. Lipids

- **Liver PI**
  L-α-phosphatidylinositol (Liver, Bovine)(sodium salt)
  Physical State: Powder
  Lot: 840042P-10MG-A322
  CAS: 383907-33-3
  Storage: -20°C
  Molecular Weight: 902.133(average based on fatty acids distribution)
  purchased from Avanti Lipids
- **Egg PE**
  L-α-phosphatidylethanolamine(Egg,Chicken)
  Physical State: Powder
  Lot: 840021P-25MG-H259
  CAS: 97281-40-8
  Storage: -20°C
  Molecular Weight: 746.608(average based on fatty acid distribution)
  purchased from Avanti Lipids
- **Heart CA**
  Cardiolipin(Heart, Bovine)(sodium salt)
  Physcical State: Chloroform Solution
  Lot: 840012C-50MG-A-536
  CAS: 383907-10-6
  Storage: -20°C
  Concentration: 25mg/ml
  Molecular Weight: 1494.319(average based on fatty acid distribution)
  purchased from Avanti Lipids
- **Brain PS**
  L-α-phosphatidylserine(Brain, Porcine)(sodium salt)
  Physical State: Chloroform Solution
  Lot: 840032C-25MG-A-822
  CAS: 383907-32-2
  Storage: -20°C
  Concentration: 10mg/mL
  Molecular Weight: 824.966(average based on fatty acid distribution)
  purchased from Avanti Lipids
- **18:1 Biotinyl PE**
  1,2-Distearoyl-sn-Glycero-3-Phosphoethanolamine-N-[Biotinyl(Polyethylene Glycol)2000)]
  Physical State: Powder
  Lot: 870282-01-035
  CAS: 384835-53-4
  Storage: -20°C

Molecular Weight: 992.311(average based on fatty acid distribution)
purchased from Avanti Lipids

- **18:0 DSPC**
  1,2-Distearoyl-sn-glycero-3-phosphocholine
  Physical State: Powder
  Lot: 850365-03-152
  CAS: 816-94-4
  Storage: -20°C
  Molecular Weight: 780.145(average based on fatty acid distribution)
  purchased from Avanti Lipids
- **Egg Liss Rhod PE**
  L-a-Phosphatidylethanolamine-N-(lissamine rhodamine B sulfonyl)(Ammonium Salt)
  Physical State: Powder
  Lot: 810146-01-066
  Storage: -20°C
  Molecular Weight: 3016.781 (average based on fatty acid distribution)
  purchased from Avanti Lipids
- **DIO**
  3,3-Dioctadecyloxacarbocyanine perchlorate
  Molecular Weight: 881.72
  Storage: -20°C
  CAS: 34215-57-1

A.3. Hardware

- Objective, CFI Apochromat TIRF 60x Oil, NA 1.49, 0.13 WD, MRD01691
- 488 nm Luxx 488-100,100mw diode laser, Omicron Laserage Laserprodukte GmbH
- 561 nm 100 mw diode laser Coherent
- 1064 nm SmartLasers systems, Diode Nd:YVO4 Laser 3W cw
- 1450 nm Heating laser, QPhotonics QFBGLD-1450-150,
- Heatinlaser mount LM14S2 from Thorlabs
- Heating laser controller – OEM Laser Diode & Temperature Controllers ITC110 Laser diode mount
- optical table Standa, 1HB06-06-07 HoneyComb Breadboard, 1HT10-12-20 Honeycomb Tabletop
- Piezo Sample coarse rough stage, 3d open loop system, SLC-1720, travel range 12mm, controller MCS-3CC-USB-TAB, MCS controller
- Piezo Sample fine stage, Npoint NPXY100Z50-244 + controller LC403 DSP 3ch, travelrange 100x100x50 µm
- Piezo tip tilt piezo mirror, TT2.5, OptoPhase, Controller USB163 v5 5 mrad.
- linear stage TIRF incident angle, SmarAct, 2x SLC 1730-M-E, 18mm travel range, 100nm res, hard end stop, controller CU-3DM-USB-TAB
- QPD stage, xy positioning MechOnics MX35 Stage
- vibration isolation system, Minus K MIN 500 BM-1
- Fluorescence Camera Hamamatsu Orca Flash 4.0 v2, sCMOS 2048x2048px, 100fps Framegrabber Firebird FBD-1XCLD - 2PE8, PCIe
- GFP bandpass, 520/40ET Bandpass, F47-520
- Rhodamine bandpass, 605/70 ET Bandpass
- Colorsplitter, Beamsplitter H 560 LPXR superflat
- IRM cleanup, 450/30 ET Bandpass
- 488 block in Fluorescence detection, 488 LP Edge Basic long pass
- IR blocking, 1450 nm OD 5, 1064 OD 6 , Multiphoton HC 770/SP
- TIRF Cleanup, Laser Clean-up Filter ZET 488/10
- 2nd level Dichorid, 500DCSPXR
- IR Beamcombinder, T1260DCSP-xxt
- 3rd Level Dichroid, Multiphoton SP T700 SPXR 1500(2/3P)
- IRM Camera, Lt225M CMOS, lumenera, 2048x1088px, 180fps
- IRM Zoom, Sill Optics, 7x Zoom for 1/2 ”ccd
- water cooling, Hailea, HC-150A
- Power supply 1 – Agilent E3648
- Power supply 2 – Agilent E3631A
- Power supply 3 – Agilent E3620A
- Power supply 4 – New focus, Intelligent pico motor driver Model 8753
- Power supply 5 – Gwinstex, GPS-2303

- NI PXI-1033 Chassis, Integrated MXI Express, 5 Peripheral Slots 1 PCIe,3m Cable
- NI PXIe-4472B, used for QPD - xyz, fine piezo stage - xyz, piezo mirror - xy
- NI PXI-6221 2x, used for Temperature sensors, Heating laser monitor signal
- NI PXI-6733, Analog output used for fine stage, tilt mirror, heating laser control

B. Protocols

B.1. Glasslide cleaning – "easy cleaning"

The "easy Cleaning" protocol has been adapted from a lab internal source – Dr. Michael Bugiel, version from 2009.
Materials:

- 2 x glass boxes
- 2 x custom teflon racks for cover slides
- coverslides 18x18 mm^2, 22x22 mm^2)
- Sonicator(VWR USC - THD), tweezers and gloves

Chemicals:

- Distilled Water(dH2O)
- Mucasol diluted 1:20 in dH2O
- Ethanol technical

Procedure:

- Load slips into racks and racks into 1st box
- Fill with Mucasol (slips must be covered), close the cap
- Put into sonicater, sonicate for 15 min, 100%
- Store racks into 2nd box, wash with dH2O for 2min or longer
- Remove Mucasol from 1st box and wash with dH2O, fill in ethanol and racks, close with cap
- Put into sonicater, sonicate for 15 min
- Store racks into 2nd box, wash with dH2O for 2min or longer
- Store Ethanol for later using in a bottle
- Wash 1st box with dH2O, load with racks and repeat procedure 3x, change gloves at least every cycle
- After last washing, store racks into 2nd box, remove dH2O form 1st box, store racks into 1st one again and dry them with N2, close the box with cap
- Cleaning of 2nd box (incl. cap):
- Shake with Mucasol
- Rinse with dH2O
- Shake with Ethanol

- Rinse with dH2O
- Dry with N2
- Store racks into cleaned box, seal with Parafilm

B.2. Flowcell preparation

Materials:

- easy cleaned glass slides
- Parafilm, glass slides, double-sided sticky tape for spacer(Tesa)
- Spacer: Parafilm, Tape, Glass, Tape, Glass, Tape, Glass, Tape, Parafilm thickness $\approx$ 0.8 mm
- Peek tubings, Tub PEEK Nat 1/32 x .015 x 5 ft, WO 1109924, IDEX Health & Science
- Adapter tube for pipette tips
- Two component glue (10 minutes resin)

Procedure:

- Prepare beforehand the spacer
- Assemble the flow cell
- Turn on the heat plate up to 120°C
- Take a 22x22 FDTS cover slide and place the spacer to form a channel
- Cover the channel with a 18x18 mm cover slide
- Use the heat plate to melt the channel to the glass for about 30 seconds
- Place the peek tips inside the channel
- Mix the resin and wait $\approx$ 5 minutes until it is less viscous
- Seal the channel with resin
- Mix new resin and seal the rest of the flow cell edges with liquid resin
- Wait 2h until the resin is dry
- Put more resin at the edges where the tubes stick out, mostly it can leak there
- Seal again with nail polish
- To disassemble the flow cell and reuse the peek tubings
- Remove adapter tubes
- put the whole flow cell in ethanol $\approx$ 1-2 days
- Rinse the tubes with water, ethanol, pressured air directly after the exp
- Add fresh pipette tips

B.3. GUV formation

Materials and solutions:

- PTFE reactionchamber with Pt Wires
- Formation buffer, sugar based
- Function Generator, H-Tronic, FG 250 D or Voltcraft 7202 Sweep / Function Generator
- clamps - Abgreifklemmen BNC SS 7186 :: BNC- male, special lead, 2 A, 25 cm
- hamilton syringe, SYR10 10 µl 701 N, PN:80365/00

Method:

- Put the in EtOH stored reaction chambers and Pt wires in technical EtOH and sonicate them for 20 mins at max. power; afterwards dry them with N2
- Use 2.5 µl of the GUV mixture for each Pt wire and wet the front of the wires carefully; do this for both wires (2x 2.5 µl)
- Vacuum 10 min, in glass petri dish, cover with aluminium foil
- Add 350 µl of buffer solution to the reaction chamber
- Screw the wetted Pt wire piece into the chamber
- Put parafilm around, they can leak
- Put the chamber piece in a PCR reactor or heater and apply a temperature of 45°C
- Apply a voltage of 2 V to the wires formationtime/voltage can be optimized for different lipids:
- 1 h with a frequency of 10 Hz
- 0.5 h with a frequency of 2 Hz
- Stop the voltage and unscrew the chamber from the Pt wire piece
- Use a small amount of the GUV solution to check under the fluorescence microscope
- Let them cool down for 5 min, transphere with cut pipett tip

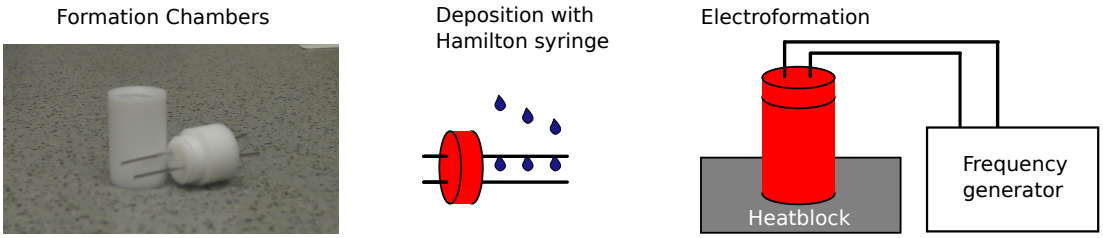

Fig. B.1 | GUV formation protocoll. Important droplets should dry independently. And for reproducibility I performed the formation alwasy at 45 °C due to significant temperatures changes in wet lab over the seasons.

B.4. Supported lipid bilayer

Materials:

- PBS buffer, ph 7.4, pre heat at 65°C
- SLB buffer, ph7.4, pre heat at 65°C , degased buffer - reduces bubble formation
- CaCl2, 0.5 M , pre heat
- Lipids for bilayer
- flowcell
- Heating plate pre heat at 65°C
- Sonicator pre heat at 65°C
- Flowcells pre built

Procedure:

- Mix your Lipids for the bilayer
- According to the ratio you want calculate with the xls file beforehand, for stocks
- Mix them in Chloroform, dry them in the desicator, store them under N2
- Make multilamellar vesicels:
- Take a 0.5mg DSPC aliquote
- Add 60 µl PBS and vortex it
- Sonicate it in the 65°C Heater for 3 minutes
- Make 10µl Aliqotes store them @ -20
- Make SUVs
- Take 10µl aliqote add 140µl of warm SLB buffer
- Optional:
- Add 1µl of DiO dilution (50mM Stock, take 0.78 µl put in 100µl PBS)
- Add 1µl of Biotin-PEG-PE of Stock(10mg/ml)
- Final volume 150µl

- Sonicatte at 100% power at 65°C for 5–10 minutes
- Deposit bilayer on glass support
- Put the flowcell on the 65°C heating block
- Add 250 µl of hot SLB buffer, Final volume 400µl
- Split the Vesicle mix into two 200µl epis, keep them on the hot plate
- Add 1,2 µl of 0.5 M CaCl2 to one of the vesicle mix, final concentration 3mM
- Fill the flowcell with the hot vesicle mix
- Incubate for 10 minutes on the hotplate
- Wash with hot SLB buffer to remove CaCl2 and none fused vesicles

B.5. Bead coupling

The coupling protocol has been adapted from a lab internal source – Tobias Jachowski 2016
buffers and reageants: Coupling Protocoll Tobi Buffers etc.

- coupling buffer (Polylink protein coupling link)
- Tween20 10
- 10x NT buffer
- 1x NT + 0.1% Tween (NTT)
- 1x NTT + 10 mg/ml BSA (NTT10BSA)
- COOH-beads (820 nm, 0.11 mg/ul or 920 nm, 0.11mg/ul) 10ul
- ED(A)C rund 4 mg
- IgG or Neutravidin in non NH2 buffer (MWIgG 150 kDa) 4 or 10 ug
- AminoPEG 2 kDa (MW 2 kDa) 13 mg
- syringe (1 ml) and needle (0.4 mm) 1x
- sonicator (big one in cold room)

2. Activation

- take out ED(A)C from freezer to let it warm up
- vortex bead
- take 10 ul of COOH-beads
- add 400 ul coupling buffer
- Vortex briefly to resuspend beads
- add 2ul Tween20 (10
- wash 75 s, 13,400 rpm (Eppendorf mini spin), resuspend in 2 ul Tween20 (10 %) and 400 ul
- coupling buffer (final Tween concentration to 0.05 % (TechNote 205? Bangslabs))
- Vortex briefly to resuspend beads
- wash 75 s, 13,400 rpm, resuspend in 1 ul Tween20 (10 %) and 200 ul coupling buffer
- Vortex briefly to resuspend beads
- fill a point of a spatula EDC (4 mg) into new tube
- fill a point of a spatula sulfo-NHS (4.5 mg) into new tube
- mix suspended beads with sulfo-NHS
- mix suspended sulfo-NHS beads with EDC
- incubate for 15 min at RT
- wash 3x 75 s, 13,400 rpm, resuspend in 1 ul Tween20 (10%) and 200 ul coupling buffer
- 10mg 2k Peg + 10µl AntiRhodamine (1mg/ml Stock) + 30 µl Coupling buffer

3. Coupling

- pipet beads on top of protein droplet to ensure fast mixing
- incubate 60 min at RT (25 °C) and 1000 rpm on shaker (interval mix, 10 s on, 1:30 min off)
- add 50 ul 10 x NT buffer (stop reaction)
- incubate 5 min
- add 100 ul NTT
- wash 2 min 13,400 rpm, resuspend in 200 ul NTT
- possibility to store beads over night in fridge
- wash 75 s, 13,400 rpm, resuspend in 200 ul NTT
- if protein: sonicate for some seconds, to get rid of clusters and more than monolayer of protein.
- Check on microscope (1:40 beads:H2O)! Sonicate no longer than necessary.
- wash 75 s, 13,400 rpm, resuspend in 200 ul NTT
- wash 75 s, 13,400 rpm, resuspend in 100 ul NTT
- check on microscope (1:40 beads:H2O), if beads not single, sonicate no longer than necessary.
- Add 900 ul NTT10BSA and store.

B.6. Tetherpulling assay DOPC

Procedure GUVs:

1. Produce

- sonicate GUV formation chambers 5min ethanol, dry with pressured air
- prepare lipid mixture
- prepare formation buffer succrose based
- prepare GUVs according to protocol B.3
- Transfer into epi + 300 µl sucrose

2. Prepare supported lipid bilayers

- prepare a sample as described in protocol B.2
- DSPC + biotin-PE in the wanted concentration
- incubate 30min with NeutrAvidin 1mg/ml 5µl, diluted to 100 µl per Flow cell
- Exchange buffer to glucose

3. GUV immobilization

- add 20 µl GUV for 30min. Slowly filling the flow cell, two centimeters height difference between tube ends, check orientation of sample!
- Cleaning, turn the flow cell upside down, with at least rinse 2x 1000 µl
- Blocking biotin 1mg/ml 10µl, diluted to 100 µl per flow cell 10 min
- Buffer exchange higher glucose, to get a floppy dome for vesicles.
- Change buffer to glucose + Anti bleaching buffer
- Incubate with NeutrAvidin Beads in Anti bleaching buffer
- add 1:1000 microsphere dilution

4. Tether pulling

- Calibrate bead AC 32 Hz, 1.4 µm pp
- Triangle function on stage to attach bead to GUV, record a few pulling events

Statement of authorship

Statement of Authorship

I hereby certify that

- I have composed this thesis by myself,
- all references and verbatim extracts have been quoted, and all sources of information have been specifically acknowledged,
- this thesis has not been accepted in any previous application for a degree, neither in total nor in substantial parts.

Eidesstattlicher Versicherung

Ich versichere hiermit, dass ich

- die vorliegende Arbeit selbstständig verfasst habe,
- keine anderen als die angegebenen Quellen benutzt und alle wörtlich oder singemäß aus anderen Werken übernommenen Aussagen als solche gekennzeichnet habe
- description und die eingereichte Arbeit weder vollständig noch in wesentlichen Teilen Gegenstand eines anderen Prüfungsverfahrens gewesen ist.

.....	.....
Ort, Datum	Unterschrift/Signature
Place, Date	Gero L. Hermsdorf

Es ist mir in den Wissenschaften gegangen wie einem, der früh aufsteht, in der Dämmerung die Morgenröte, sodann aber die Sonne ungeduldig erwartet und doch, wie sie hervortritt, geblendet wird.

— Johann Wolfgang von Goethe
Maximen und Reflexionen 372